Enhancing the potential of optical coherence tomography in human myopia research

DISSERTATION

der Mathematisch-Naturwissenschaftlichen Fakultät

der Eberhard Karls Universität Tübingen

zur Erlangung des Grades eines

Doktors der Naturwissenschaften

(Dr. rer. nat.)

vorgelegt von

KATHARINA BREHER

aus Kempten (Allgäu)

Tübingen

2021

Contents

Acronyms list

AEL	Axial eye length
CDF	Cumulative distribution function
ChT	Choroidal thickness
CI	Confidence interval
CR	Coefficient of repeatability
CV	Coefficient of variation
CVI	Choroidal vascularity index
ETDRS	Early treatment of diabetic retinopathy study
H	Horizontal (meridian)
ICC	Intraclass correlation coefficient
IQR	Interquartile range
LoA	Limits of agreement
MRI	Magnetic resonance imaging
OCT	Optical coherence tomography
ONH	Optic nerve head
PRX	Peripheral refraction
ROI	Region of interest
RPE	Retinal pigment epithelium
RRC	Retinal radius of curvature
V	Vertical (meridian)

1 Introduction

1.1 Motivation

Myopia is a refractive error usually caused by an overshoot of ocular growth compared to the focal length of the eye. This leads to blurred distance vision despite relaxed accommodation and the need for optical correction [Chen et al., 2009]. More importantly, myopia is also associated with an increased risk for sight-threatening pathologies, such as myopic macular degeneration, retinal detachment and glaucoma [Saw et al., 2005; Spaide et al., 2014]. This situation generates a public health concern as the prevalence of myopia has been increasing over the last decades and will continue to do so in the future. In 2050, 50% and 10% of the worldwide population are suggested to be myopic (-0.50 D to -5.00 D) and highly myopic (more than -5.00 D [Diez et al., 2019a]), respectively [Holden et al., 2016]. Along this line, myopia-related vision loss is predicted to rise by a factor of seven within the next 30 years. Thus, myopia is evolving to one of the main origins of blindness [Holden et al., 2016].

Research puts great effort into understanding the aetiology of myopia and attenuating this development. It was found that genetic and environmental factors play a role in the risk of myopia onset and progression [Pan et al., 2012]. For myopia onset, parental myopia as a genetic factor increases the risk for their children to become myopic [Pacella et al., 1999; Mutti et al., 2002]. As the most important environmental factor, time spent outdoors can significantly delay the onset of myopia. The mechanism is assumed to work by the increased depth of focus, dopamine release through light intensity and extended light spectrum, as well as the different spatial frequency content compared to indoor environments [Xiong et al., 2017; Lingham et al., 2020; Flitcroft et al., 2020]. In contrast, the role of intensive near work as an accelerator, e.g. through a reduced efficacy of the accommodative system, is of debate with inconclusive study results [Lin et al., 2014; Huang et al., 2015].

Additionally, it is known that the rate of myopia progression is dependent on the age of myopia onset: the younger myopia occurs in a child, the faster its progression will be and the higher the risk to suffer from especially high myopia [Pärssinen and Lyyra, 1993; Saw et al., 2000; Chua et al., 2016; Diez et al., 2019b; Verkicharla et al., 2020]. Again, no clear relation between near work and faster myopia progression could be found [Berntsen et al., 2011]. Furthermore, central and peripheral retinal defocus is suggested to be a significant neurally-optically regulating factor of eye growth in animal models [Schaeffel et al., 1988; Wallman et al., 1995; Wallman and Winawer, 2004].

Hyperopic defocus stimulates eye growth and promotes myopia, as the retina is striving to rematch to the image plane. Vice versa, myopic defocus is regarded as an inhibitor of eye growth.

Therefore, a major portion of myopia control strategies is based on the modulation of said retinal defocus. These interventions include various spectacle lens approaches, such as under-correction, bifocal lenses, progressive addition lenses, radial refractive gradient lenses and defocus incorporated multiple segments lenses. Moreover, different contact lens designs are in use, for example bifocal, multifocal, multizone bifocal and orthokeratology lenses. Other options consist of pharmacological interventions, surgical procedures or contrast-modulating spectacle lenses. Overall, pharmacological interventions showed the highest efficacy in inhibiting axial length growth, followed by contact lenses and spectacle lenses [Huang et al., 2016]. However, there is a high intersubject variability of control outcomes within the same type of intervention [Huang et al., 2016; Wildsoet et al., 2019]. Besides the efficacy, other factors have to be considered, such as the side effects of pharmacological interventions, including a temporary loss of accommodation and pupil mydriasis with increased light sensitivity [North and Kelly, 1987].

So far, the rate of myopia progression and the efficacy evaluation of myopia control strategies have been mostly limited to a longitudinal analysis of axial length and/or spherical refractive error compared to placebo groups. However, as the change of both these parameters is relatively slow, this longitudinal research approach commonly requires year-long studies with follow-up visits (see reviews by Huang et al. [2016] and Wolffsohn et al. [2019]). This situation is disadvantageous, as it takes a long time until the first results from initial hypotheses are derived. This duration becomes ethically even more critical, especially in clinical studies with children, when either the tested treatment option does not lead to the desired efficacy or a placebo control group is involved, where no beneficial effect is expected.

Therefore, myopia research strives to establish a set of parameters that are able to indicate early and reliably the long-term change of axial length and/or refractive error. In scientific use, this type of parameter is defined as a "biomarker". Biomarkers represent quantitative indicators for ongoing biological processes in a diagnostic or predictive manner. Here, retinal imaging, especially optical coherence tomography (OCT), allows the evaluation of current and novel optical biomarkers for myopia research. However, the technology still needs to be investigated regarding its potential in human myopia studies. Ultimately, the identification and usage of OCT-based biomarkers could not only result in an improved research process but could also lead to a future implementation in clinical settings.

1.2 The human visual system

This chapter covers the fundamental aspects of the human visual system, especially the posterior segment, as these structures are most related to the topic of this dissertation.

1.2.1 Anatomy and physiology of the posterior eye

The following information on ocular anatomy and physiology was extracted and summarized from Lens et al. [2008] and Remington and Goodwin [2011]. The human eye can be organized into an anterior and posterior segment, as depicted in Figure 1a. The anterior segment consists of the visual system's main optical components, such as the cornea and the crystalline lens. The iris and pupil are located between these structures and regulate aperture-like the incidence of light. The anterior and posterior chamber represent the aqueous-humor-filled spaces between the cornea and iris and the iris and lens, respectively.

The posterior segment contains the vitreous chamber and the retina with the optic nerve head. The retina is composed of ten separate layers (see Figure 1b) with their main functions listed and numbered from inner to outer retina: (1) The inner limiting membrane as barrier basement membrane. (2) The nerve fiber layer with the ganglion cells' axons, leading to and eventually forming the optic nerve. (3) Ganglion cell layer with the nuclei of the ganglion cells for complex information processing collected from bipolar and amacrine cells. For this, ganglion cells contain receptive fields that are selectively responsive to various temporal and spatial light patterns in an ON and OFF fashion. Moreover, intrinsic photosensitive retinal ganglion cells are regulators of the circadian rhythm via melanopsin. (4) The inner plexiform layer with synapses between bipolar cells, ganglion and amacrine cells. (5) The inner nuclear layer with the nuclei of the amacrine, bipolar and horizontal cells as signal processors. (6) The outer plexiform layer with synapses between photoreceptors with bipolar and horizontal cells. (7) The outer nuclear layer with the nuclei of the photoreceptors. (8) The external limiting membrane as a separation barrier between photoreceptor cell bodies and inner/outer segments. (9) The photoreceptor layer with the inner and outer segments of the rods and cones. Rods are responsive to single photons and sensitive in mesopic and scotopic light conditions. Cones are categorized into long-, middle- and short-wavelength cones and represent the basis for photopic and trichromatic color vision. (10) The retinal pigment epithelium as a supportive, nutritional and barrier epithelial layer for the outer retina. Moreover, the melanin-containing pigment cells reduce light scatter within the eye.
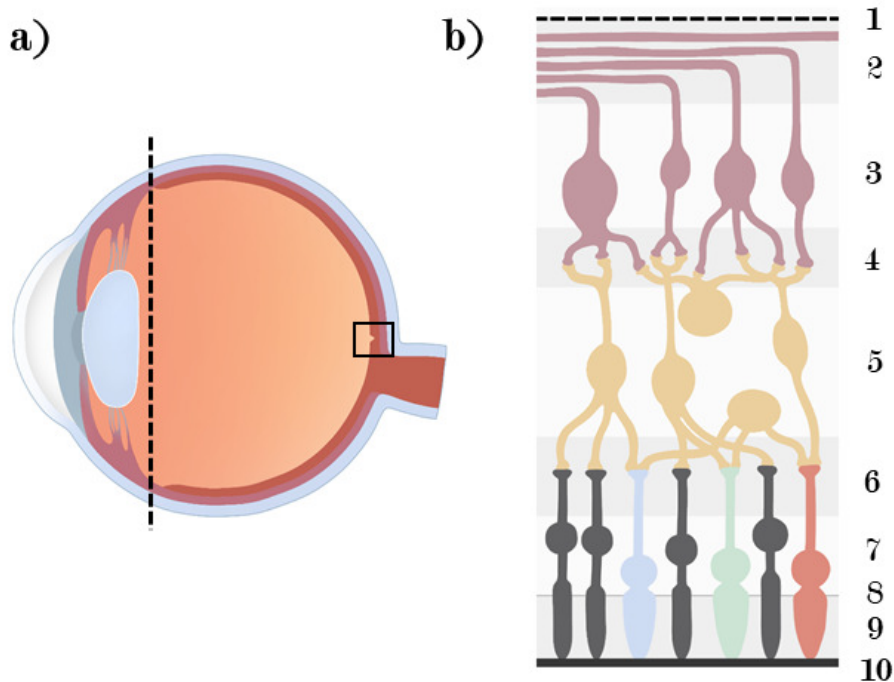
Figure 1: a) Sagittal scheme of the eye with the main anatomical components and the separation into anterior and posterior segment (adapted from Kolb [2012]); b) Magnified drawing of the previously described and numbered ten retinal layers (adapted from Koeppen and Stanton [2009]).

The choroid and the sclera enclose the outer retina to ensure blood supply and stability/protection. While the inner retina is resourced by the aqueous humor and the retinal and uveal vascular system, the outer retina and the anterior optic nerve draw the nutrients and oxygen from the choroid. The choroid is structured in five distinct layers: Bruch's membrane (collagen and elastin), choriocapillaris (small capillaries), Sattler's layer (medium vessels), Haller's layer (large vessels) and the suprachoroid (collagen, fibroblasts, melanocytes). The choroidal stroma presents the choroid's extravascular connective tissue and consists of melanocytes, elastin, fibroblasts, mast cells, macrophages, lymphocytes, and smooth-muscle cells. The autonomic nervous system innervates the choroidal vessel walls. On the one hand, parasympathetic innervation triggers vasodilation via the neurotransmitter nitric oxide and vasoactive intestinal polypeptide. On the other hand, sympathetic innervation and associated vasoconstriction are achieved via the neurotransmitter noradrenaline. While blood supply is the primary function of the choroid, it is also involved in the regulation of intraocular pressure, thermic and ocular growth [Nickla and Wallman, 2010].

1.2.2 Central and peripheral optics

According to the Gullstrand No. 1 eye model, the total optical power of the eye with relaxed accommodation is 59 D and has a normative ocular axial length of 24.39 mm [Artal, 2017]. Ideally, in a relaxed state of accommodation, the focal length and axial length of the eye are coordinated with each other, called emmetropia (see Figure 2a). However, refractive errors occur in case of a mismatch between both parameters. Supposing the axial length is too long or the total optical power too strong, the focus point is located in front of the retina (Figure 2b), resulting in myopia. Vice versa for hyperopia as depicted in Figure 2c. Astigmatism with two focal lines instead of one focal point occurs if the lens or cornea exhibit a cylindrical shape with two optically different meridians instead of a homogeneous spherical shape. Spherical defocus and astigmatism are considered as lower-order aberrations [Artal, 2017]. More complex higher-order aberrations commonly arise from off-axis optics and larger pupils. The aberrations of the highest clinical importance (as being the most visually affecting) are spherical aberration, coma and trefoil [Philip et al., 2014].
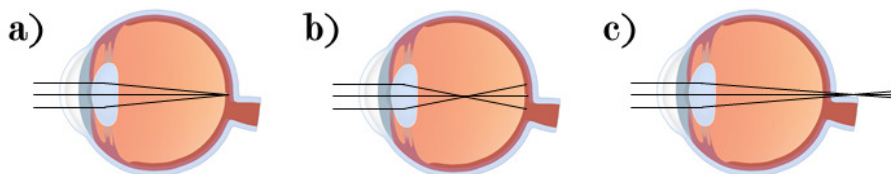
Figure 2: The three spherical refractive errors: a) emmetropia; b) myopia; c) hyperopia.

The aforementioned refractive errors can be measured not only in the central but also peripheral retina [Fedtke et al., 2009]. Due to off-axis optics, the peripheral refraction changes with the angle of eccentricity. If the relative peripheral refraction is of interest, the profile is normalized, such that the central refractive error is set to zero. An example of a relative peripheral refractive profile acquired with eccentric photorefraction [Tabernero and Schaeffel, 2009a] across a $\pm 50°$ horizontal retinal angle is given in Figure 3. Here, relative peripheral hyperopia is visible, more pronounced on the temporal than the nasal retina. Moreover, the optic nerve head's reflective properties usually cause a myopic dip on the nasal side.

Five fundamental patterns of peripheral refraction were determined along the horizontal visual field in the healthy population [Ferree et al., 1931; Rempt et al., 1971; Atchison, 2012] when only lower-order aberrations are considered:
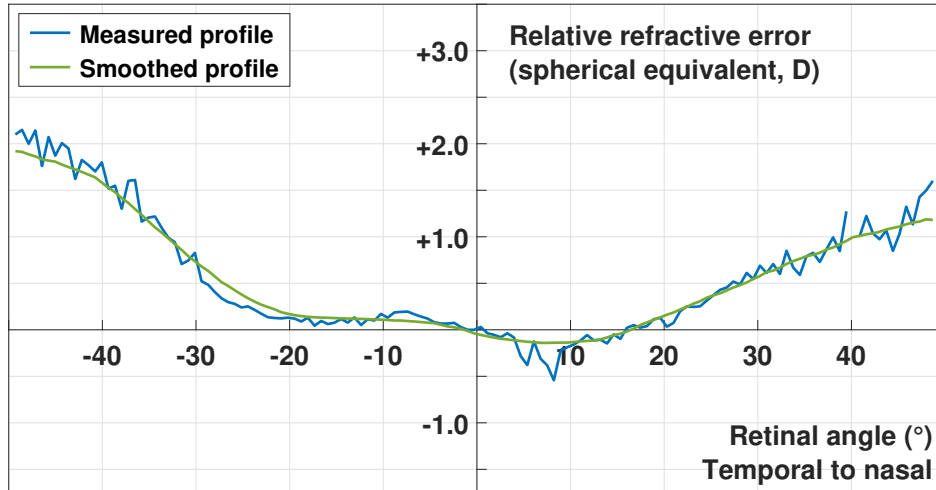
Figure 3: Exemplary normalized (blue) and normalized plus smoothed (green) two-dimensional peripheral refraction profile. Refractive error is plotted on the y-axis, retinal angle on the x-axis.

(1) Type I with relative hyperopia in the horizontal and vertical meridian; (2) Type II with relative hyperopia in the vertical meridian and nearly relative emmetropia in the horizontal meridian; (3) Type III with a naso-temporal asymmetry of refractive profiles; (4) Type IV with relative hyperopia in the vertical and relative myopia in the horizontal meridian; (5) Type V with nearly relative emmetropia in the vertical and relative myopia in the horizontal meridian.

As will be explained later, the peripheral refractive error is somewhat related to the central refractive error, as it has implications on eye growth regulation. Myopes tend to exhibit more often relative peripheral hyperopia (Type I and II), whereas patterns for emmetropes and hyperopes shift into the myopic directions, represented as Type IV and V [Verkicharla et al., 2012]. However, a more recent study using the more advanced technique of two-dimensional wavefront aberrometry did not find any relation between central and peripheral refractive error [Lan et al., 2019].

1.3 Regulatory processes of eye growth

1.3.1 Fundamental concepts of emmetropization

"Emmetropization" is defined as the physiological process of ocular growth regulation to a set-point of refractive state - which is usually emmetropia. In most species, this process is more prominent and plastic in younger than older age [Siegwart Jr and Norton, 2010]. Unlike other organs, the eye relies on external visual input to guide this process via various mechanisms [Wallman and Winawer, 2004].

This fact becomes evident in animal studies, where the eye receives only manipulated visual information. On the one hand, the eye develops form-deprivation myopia when visual input is significantly degraded/restricted (e.g. via diffusers), suggesting an underlying open-loop feedback mechanism of eye growth [Norton et al., 1977; Wallman et al., 1978; Morgan et al., 2013]. Here, the importance of spatial frequency content on emmetropization were demonstrated [Schmid and Wildsoe, 1997; Tran et al., 2008; Flitcroft et al., 2020]. On the other hand, the eye can compensate for an imposed refractive error (e.g. via negative or positive lenses) in a sign- and magnitude-matching fashion, suggesting a closed-loop feedback mechanism for lens-induced myopia [Schaeffel et al., 1988; Wallman et al., 1995; Morgan et al., 2013].

However, the interpretation of defocus signals on a retinal level, such as the magnitude and directionality, still needs to be fully clarified. So far, longitudinal chromatic aberration, on- and off-axis astigmatic error composition and contrast perception/adaptation have been proposed as visual cues to serve this purpose [Wildsoet et al., 1993; Woods et al., 1996; Seidemann and Schaeffel, 2002; Wallman and Winawer, 2004; Ohlendorf and Schaeffel, 2009; Rucker and Wallman, 2012; Rucker, 2013; Flitcroft et al., 2020]. Moreover, different underlying processing of blur signals between refractive groups were found [Radhakrishnan et al., 2004; Swiatczak and Schaeffel, 2021].

Furthermore, the eye can integrate visual input on a non-linear temporal level, as seen in the processing of alternating periods of defocus conditions, recovery phases or experiments related to light conditions and the circadian rhythm [Wallman and Winawer, 2004; Zhu, 2013]. Moreover, previous studies could show that the regulation mainly occurs on a retinal level, as it also could be elicited in the absence of further optic pathway processing [Raviola and Wiesel, 1985; Wildsoet and Wallman, 1995]. Along this line, local changes in eye growth occur in the specifically stimulated retinal areas [Wallman et al., 1987; Diether and Schaeffel, 1997]. However, in the case of defocus across larger peripheral retinal regions, the eye spatially integrates the visual input, which eventually affects central refractive error [Smith et al., 2007].

This relationship is of interest when studying the impact of resulting peripheral refraction profiles in combination with human environments or optical treatments [Flitcroft, 2012; García García et al., 2019; García et al., 2019].

Due to the local regulation of eye growth, the retina, choroid and sclera were proposed as primarily involved tissues. In a simple model, the retina receives the visual input, leading to a biochemical signal cascade to the choroid and sclera. This signal cascade most probably includes retinal dopamine, retinoic acid, nitric oxide, melanopsin and glucagon [Wallman and Winawer, 2004; Troilo et al., 2019]. Here, the choroid acts as a molecular secretory site and as a rapid accommodative tissue by adjusting its thickness in response to visual input, such as defocus [Nickla and Wallman, 2010]. This results in changes in the sclera's biochemical characteristics and matrix and eventually modified scleral growth on a long-term basis [Metlapally and Wildsoet, 2015]. However, further research is required to fully understand the involved signal-and-response pathways and their connection to ocular growth regulation.

1.3.2 Structural manifestations of eye growth regulation

Re-modeling processes of the retina, choroid and sclera can nowadays be investigated via OCT. These processes are proposed to be expressed as changes in choroidal thickness, vascularity and retinal or ocular shape, as described in the following sections.

Choroidal thickness and choroidal vascularity

Based on its location between the retina and sclera, the choroid (see Figure 4a) was proposed as a potential regulator of ocular growth already in research at the beginning of the 20th century [Kajikawa, 1923; Walls, 1944]. In subsequent studies on chicks, it was indeed found that the long-term adjustment of axial length to lens-induced defocus between $\pm 15\,\mathrm{D}$ is accompanied by a preceding change in choroidal thickness of approximately $300\,\mu\mathrm{m}$ [Wallman et al., 1995; Wildsoet and Wallman, 1995]. As a result, the induction of full-field negative (hyperopic) defocus leads to choroidal thinning with simultaneous axial length growth and further myopization. In contrast, the opposite reaction can be observed for full-field positive (myopic) defocus. The choroidal response was shown to happen rapidly "in a matter of minutes" [Zhu et al., 2005]. It is suggested that the change in choroidal thickness occurs to quickly re-match the optical retinal and image plane. Moreover, the choroid is able to spatially and temporally integrate defocus patterns: On the one hand, local induction of defocus leads to corresponding local choroidal changes [Diether and Schaeffel, 1997]. On the other hand, temporally induced bi-directional changes can be reversed during recovery phases without defocus [Wildsoet and Wallman, 1995].

Beside optical defocus, other means of visual restriction can elicit choroidal thinning in animals, such as form deprivation or rearing in darkness [Wallman et al., 1995]. These alterations in choroidal thickness were also observed across a range of species, such as monkeys [Hung et al., 2000], tree shrews [Siegwart Jr and Norton, 1998] and guinea pigs [Howlett and McFadden, 2009].

Studies in humans revealed similar choroidal effects in response to defocus, albeit with significantly smaller amplitudes of less than $20\,\mu$m thickness change [Read et al., 2010; Wang et al., 2016; Chiang et al., 2015; Hoseini-Yazdi et al., 2019a, 2020]. However, these short-term results in humans are relatively subtle and inconclusive, as some studies could not detect statistically significant alterations in choroidal thickness throughout all study conditions [Breher et al., 2018; Wang et al., 2016; Chiang et al., 2015; Hoseini-Yazdi et al., 2020, 2019a]. On a long-term basis, choroidal thickening was also found with a variety of strategies applied in myopia control, such as orthokeratology lenses [Chen et al., 2016; Li et al., 2017, 2019], atropine [Zhang et al., 2016; Ye et al., 2020] or the combination of both [Zhao et al., 2020].

However, the choroid does not only respond to externally induced defocus signals for ocular growth regulation but is suggested to play a role in an intrinsic regulation process as well. The majority of cross-sectional reports in adults showed negative correlations between choroidal thickness and axial length [Wei et al., 2013; Tan and Cheong, 2014; Gupta et al., 2015], which cannot be solely caused by mechanical tissue stretching during eye growth [Read et al., 2013]. Therefore, the choroid seems to be involved in a cause-and-consequence relationship in myopia. Previous animal models strengthen this hypothesis since they found a connection between thicker choroids at baseline and reduced future myopia development [Nickla and Totonelly, 2015]. In humans, longitudinal studies show similar results: a physiological thickening of the choroid during childhood only occurs for emmetropic children but is replaced by thinning in children who were already myopic or became myopic in the future [Read et al., 2015; Fontaine et al., 2017]. Here, a spatial asymmetry was observed, where the choroid thinned inhomogeneously across the retina, with more pronounced thinning in the foveal than extra-foveal regions [Lee et al., 2015; Hoseini-Yazdi et al., 2019c].

Another important factor to consider is the choroidal diurnal rhythm, guided by the light-dark cycle of the day [Nickla and Wallman, 2010]. As a result, choroidal thickness decreases during the day and increases during the night in anti-phase to axial length. The oscillations exhibit a magnitude of change of approximately $30\,\mu$m in humans [Chakraborty et al., 2011; Tan et al., 2012; Seidel et al., 2015]. The diurnal rhythm can be modulated in humans via defocus [Chakraborty et al., 2012, 2013] or light exposure [Read et al., 2018], thus, being proposed to play another important role in ocular growth [Chakraborty et al., 2018].
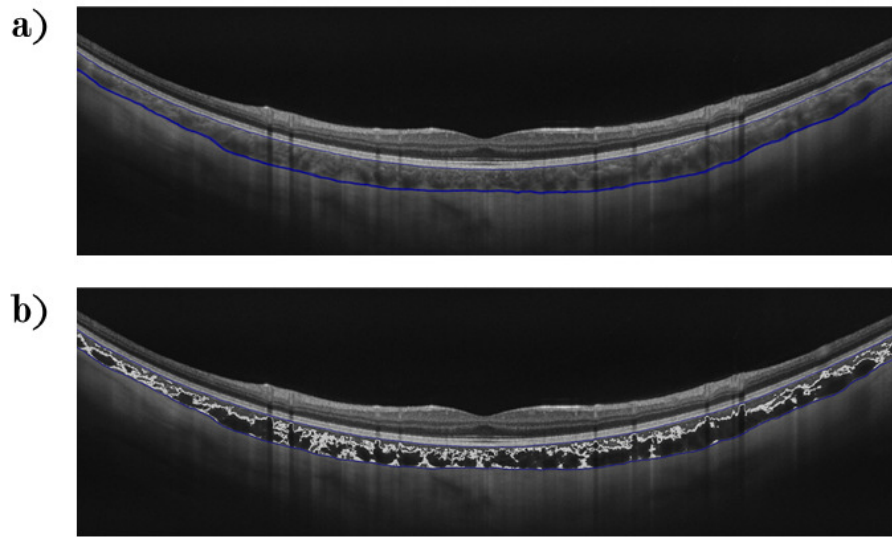
Figure 4: OCT scan of the posterior segment of the human eye with: a) segmented choroid between retinal pigment epithelium and choroidal-scleral interface (blue lines); b) choroidal vascular areas (dark) vs. stromal areas (light) in the binarized segment.

The underlying mechanisms of the short- and long-term alterations in choroidal thickness still require further research. However, it is assumed that they originate from fluid changes based on the lymphatic lanunae for non-mammals [Nickla and Wallman, 2010]. However, lacunae are absent in mammals and primates; thus, alterations in blood flow and vessel diameter are proposed as responsible factors for rapid changes in choroidal thickness in these species [Zhang and Wildsoet, 2015].

Previous studies in humans revealed a myopia-associated reduction in not only the stromal but in all vascular layers of the choroid, especially in high myopia [Grossniklaus and Green, 1992; Moriyama et al., 2007; Alshareef et al., 2017b]. Myopes exhibit diminished blood circulation in correlation with the magnitude of myopia [Akyol et al., 1996; Shih, 1998; Wakabayashi and Ikuno, 2010; Yang and Koh, 2015]. Nowadays, these numbers are extracted from binarized OCT images (see Figure 4b) with the vascular-to-total-choroidal-tissue ratio being commonly expressed as "choroidal vascularity index" (CVI) [Agrawal et al., 2020]. However, CVI results in myopia are inconsistent, also showing an increased CVI in myopia [Gupta et al., 2017]. As shown in animal models, diminished choroidal vascular function leads to a subsequent decline in the supply of oxygen and nutrients, potentially affecting the retina and sclera's growth in a myopigenic manner [Wu et al., 2018; Zhang et al., 2019]. Regarding choroidal vascularity, the choroid's altered anatomy and physiology are suggested to present a link to the observed choroidal thinning in myopia, however, with unclear cause-effect relation between them [Liu et al., 2021].

Ocular and retinal shape

Ocular growth is assumed to have implications on the retinal and ocular shape in a variety of existing eye growth models in myopia. Measurements of ocular shape showed that the eye myopic eye commonly expands more in length than in height and width, resulting in global or mainly axial growth in most examined myopes [Atchison et al., 2004]. However, it is essential to distinguish between ocular and retinal shape as two different parameters [Verkicharla et al., 2012]. On the one hand, the term "ocular shape" refers to the globe's absolute measurements, as described before. On the other hand, "retinal shape" describes the geometrical surface properties of the retina itself rather than the overall globe [Verkicharla et al., 2012]. These measurements can be conducted via magnetic resonance imaging (MRI), OCT, eccentric refraction and eccentric biometry [Dunne, 1995; Schmid, 2003; Atchison et al., 2005; Steidle and Straub, 2018]. Previous research exploiting the aforementioned methodological range revealed inconsistent results [Verkicharla et al., 2012]. Using MRI, oblate profiles were detected in both myopes and non-myopes, however, with a lesser degree in myopia and high inter-subject variability [Atchison et al., 2005; Kuo et al., 2016]. Two previous OCT studies found contradictory low correlations between retinal shape and myopia, with either less oblate shapes or larger retinal radii [Kuo et al., 2016; Minami et al., 2020]. With peripheral refraction and eccentric biometry, the findings tended to steeper and more prolate retinas in myopia vs. emmetropia [Schmid, 2003; Verkicharla et al., 2016]. In addition to the inspected correlations between retinal shape and myopia, a study found that the baseline shape of the temporal retina seemed to predict myopia progression in children [Schmid, 2011].

It is noteworthy that MRI and OCT present direct and image-based measurement tools in contrast to peripheral biometry and refraction as indirect procedures. In the case of MRI and OCT, the retinal shape can be extracted directly from scan images after correction of scan geometry (in OCT only) [Atchison et al., 2005; Kuo et al., 2016; Steidle and Straub, 2018]. While the analysis of direct measurement modalities seems to be relatively straight forward, their clinical availability is often reduced, for example due to financial reasons. In contrast, indirect methods such as peripheral refraction and biometry procedures are more widespread and in use. However, these were initially developed and optimized for central measurements. For off-axis measurements, they require additional optical assumptions of scan paths and induce unknown inaccuracies. Consequently, they should be interpreted with caution for the analysis of retinal contour [Atchison and Charman, 2011; Verkicharla et al., 2012; Koumbo et al., 2019].

Pending questions concerning structural biomarkers of myopia

In addition to the previous research findings, the aforementioned myopia-associated changes of the posterior segment deserve further critical discussion. Firstly, the in-vivo analysis of the human choroid underlies metrological-technical variations caused by measurement noise. The location of the choroidal-scleral interface is not always precisely determinable as its visibility depends on the used OCT technology, the retinal pigmentation and the absolute choroidal thickness [Kong et al., 2016, 2018; Copete et al., 2014]. The visibility is reduced with lower scan depths, higher pigmentation and thicker choroids. Another metrological parameter is the method of choroidal segmentation, which can be performed manually, semi-automated or fully automated with or without artificial intelligence being involved [Alonso-Caneiro et al., 2013; Chen et al., 2015; Gupta et al., 2015; Twa et al., 2016; Kugelman et al., 2019]. In the case of manual segmentation, results are subjective as they rely on a human examiner. In contrast, semi- or fully-automated software are more objective but show varying robustness dependent on the OCT device, scan pattern, scan area and choroidal health status [Mazzaferri et al., 2017; Breher et al., 2019b]. The same relation applies to the evaluation of choroidal vascularity, which is directly dependent on the reliability of the determination of the choroidal borders [Breher et al., 2020b; Sonoda et al., 2014]. This leads to uncertainty about whether small choroidal changes can be considered measurement noise or a truly present effect.

The ideal analysis and interpretation of choroidal changes are still not clarified along the line of effect sizes. Choroidal changes can be either measured on a paired pre-vs-post-treatment paradigm or longitudinally, such as via diurnal changes [Read et al., 2019a; Liu et al., 2021]. Diurnal experiments set the analysis on a more complex level where modulations of the diurnal rhythm in amplitude and phase are considered additional parameters. Furthermore, the measured choroidal effects cannot yet be directly transferred to their final impact on eye growth. This transfer becomes of high importance when the long-term efficacy of myopia control strategies needs to be extrapolated from relatively short-term study results.

Moreover, the assessment of retinal shape as another potential biomarker for myopia deserves further clarification. Previous studies found varying results using different methodologies. Therefore, the methodology "OCT" needs to be further evaluated in the context of other measurement tools to assess and compare different study methodologies with each other. Moreover, it is of high importance to evaluate retinal shape not as an isolated parameter but rather in an interplay with other myopia-related aspects, as proposed by Flitcroft [2012]. Here, retinal shape does not only affect the static peripheral refraction but also the dynamic defocus patterns from the environment across the entire visual field.

1.4 Technical aspects of optical coherence tomography

OCT is a biomedical in-vivo, real-time and non-contact imaging modality for biological tissue structures. Concerning the human eye, it produces high-resolution and cross-sectional images of the anterior or posterior segment. It was first introduced in 1991 [Huang et al., 1991] and since then has been most commonly used as a tool for the clinical diagnosis, progression monitoring and treatment management of retinal pathologies [Fujimoto and Swanson, 2016]. At this moment, OCT can visualize anomalies in the retinal structure in the form of e.g. cell degeneration, fluid and blood accumulation or retinal layer disassembly. The following information on the development of OCT technology was extracted and summarized from Drexler and Fujimoto [2008], Chen et al. [2019] and Bille [2019].

Time-domain OCT

Time-domain OCT was the first milestone of OCT technology development and similar to a Michelson interferometer, as displayed in Figure 5a. Here, a low-coherent broadband light source in the near-infrared region is split into a sample beam and a reference beam via a fiber-based beam splitter. The sample beam is directed towards the sample tissue (e.g. the retina), whereas the reference beam travels to a fast-moving mirror with a known position. Both beams are reflected from the tissue or the mirror and are collected at a common photodetector. This set-up leads to a difference in the traveled optical path length of the two beams, which depends on the relative position of the tissue structures to the mirror's time-encoded position. Interference only occurs if the differences between both optical path lengths lie within the short coherence length of the light source (Figure 5b). Therefore, information about the intensity versus axial depth position of the sample structures can be extracted by demodulation of the envelope of the interference pattern. Here, the envelope amplitude encodes the intensity, whereas the position over time of the reference mirror encodes the depth position in the axial direction z of the sample, as seen in Figure 5c. The resulting relation between intensity versus axial position is also called A-scan. A cross-sectional B-scan (line scan) can be acquired if the scan procedure is repeated laterally across the sample. A stack of acquired B-scans subsequently creates a three-dimensional volumetric scan pattern, referred to as C-scan or volume scan. The axial resolution of a time-domain system usually is about $10\,\mu m$ with a scan depth of $2\,mm$. However, the mirror's mechanical movement in time-domain OCT limits the scan rate (number of A-scans taken per time frame) and scan quality.
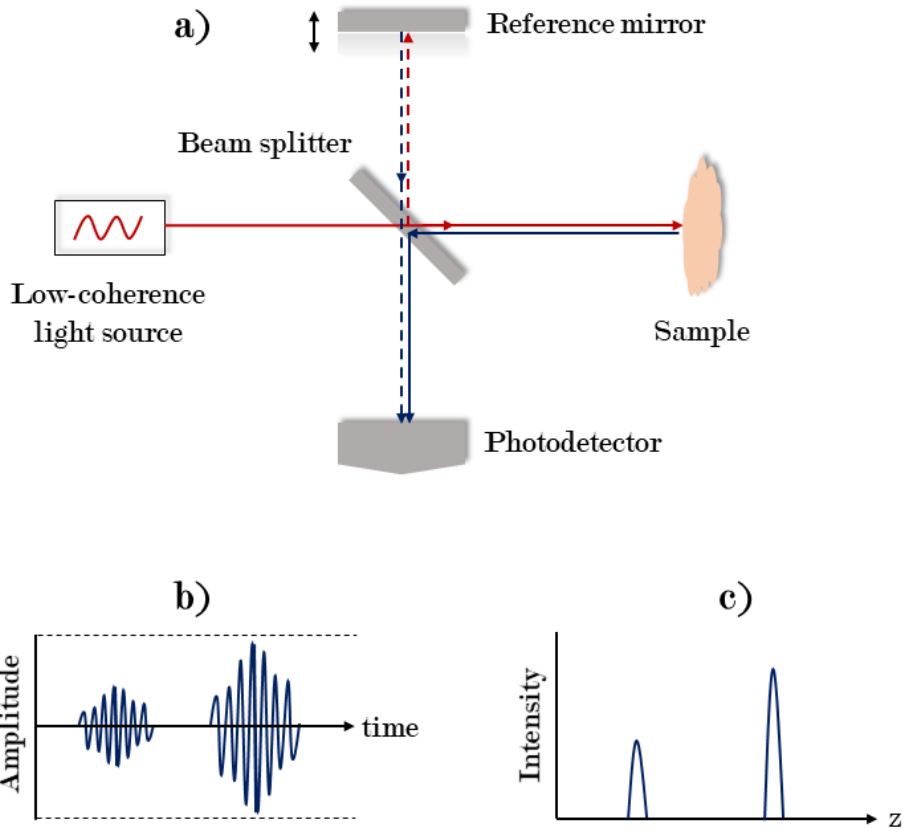
Figure 5: a) Michelson interferometer set-up of a time-domain OCT system; b) resulting interference signal of two layers of a sample; c) A-scan pattern of two sample layers. Adapted from Bille [2019].

Fourier-domain OCT

Fourier-domain OCT development abolished this constraint: allowing higher scan speeds, improved signal-to-noise ratios, and reduced motion artefacts. Fourier-domain OCT can be separated into spectral-domain and swept-source systems. The set-up of a spectral-domain system resembles time-domain systems, however, a spectrometer is used to process the incoming scan signal, and the mirror is fixed (Figure 6a). The near-infrared, broad-band source spectrum gets decomposed into the wavelength-specific interferograms, containing the complete depth information at once without the need for a moving reference mirror. However, the scan depth in spectral-domain OCT is usually limited to $2\,\text{mm}$ in the eye, as the depth resolution decreases with more considerable optical path differences, thus, deeper located tissue structures. Swept-source OCT uses time-encoded sweeping through a broad-band light source as a baseline (Figure 6b). The tunable light source eliminates the spectrometer and its associated disadvantages regarding scan time and scan depth. Therefore, an even higher scan rate of $> 100\,\text{kHz}$ can be achieved with these systems, while increasing ocular scan depth up to 3 to $6\,\text{mm}$ with a central wavelength λ_0 near $1060\,\text{nm}$.
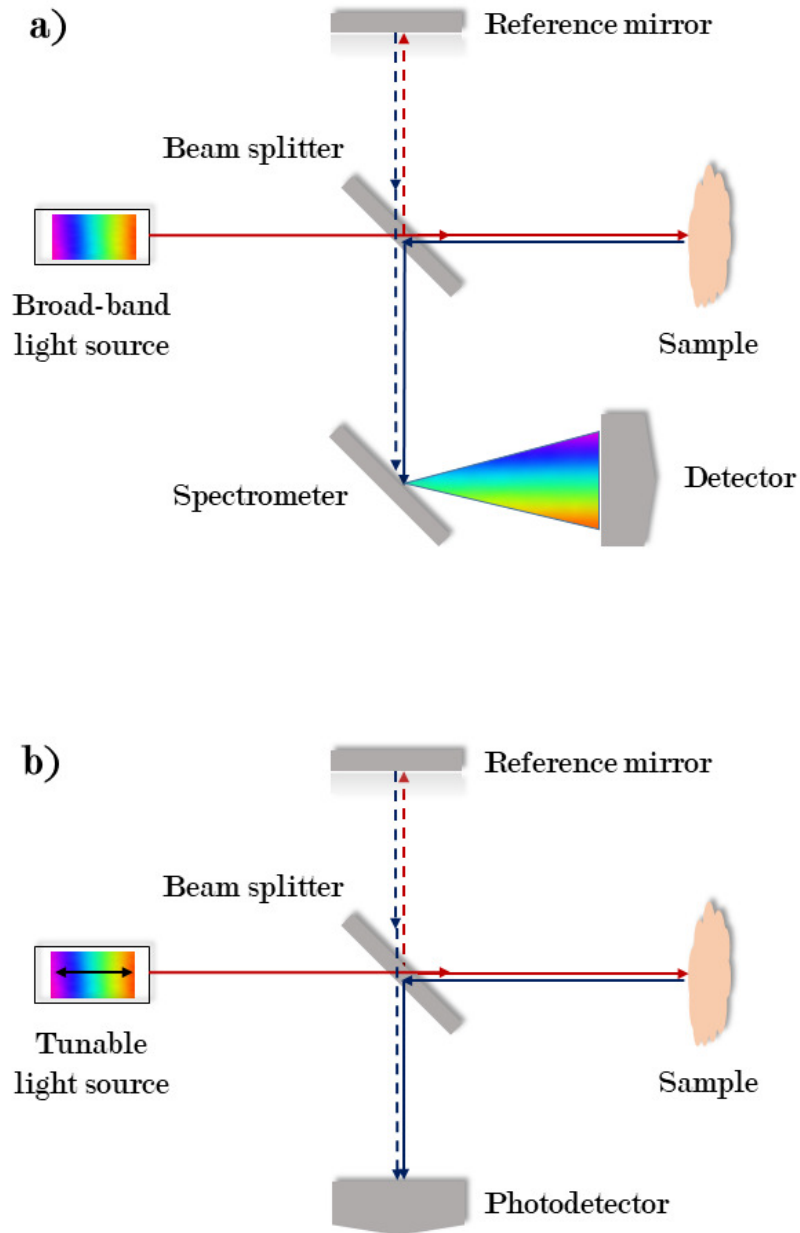
Figure 6: Set-up of Fourier-domain OCT systems: a) spectral-domain OCT; b) swept-source OCT. Adapted from Bille [2019].

The interference signal in Fourier-domain systems encodes the A-scan profile in a wavelength-specific manner. The intensity I is proportionally linked to the modulation amplitude (MA) of the interference signal, which in turn is associated with the reflectivity of the sample (R_s) and reference mirror (R_r) as seen in Equation 1.

$$MA = \sqrt{R_s \cdot R_r} \tag{1}$$

The depth position z is related to the wavelength-dependent modulation frequency MF of the interferogram. The higher the modulation frequency, the larger is the difference in optical path length between reference and sample beam according to Equation 2.

$$MF = \frac{\pi}{z} \tag{2}$$

Fast Fourier transformation of the interference signal achieves the conversion from the obtained interferogram into an A-scan pattern. This means that the wavelength-dependent intensity profiles $I(\lambda)$ for all sample layers z are transformed into a position-encoded intensity profile $I(z)$.

Determinants of scan quality

There are essential parameters defining image quality and clinical usability of OCT scan images. Higher scan rates (dependent on the used technology and system components) mainly reduce scan acquisition time and, therefore, motion artefacts resulting from eye movements. The central wavelength and subsequent light absorption, light scattering, and signal roll-off while passing through ocular media and signal detection and processing determines the scan depth.

Besides scan depth and scan rate, an OCT system's resolution is another crucial aspect to be considered. The axial resolution in air, δ_z, is dependent on the coherence length of the light source (Equation 3), where λ_0 is the central wavelength and $\Delta\lambda$ the bandwidth of the light source. Larger central wavelengths require broader bandwidths in order to maintain the desired axial resolution.

$$\delta_z = \frac{2 \cdot ln(2)}{\pi} \cdot \frac{\lambda_0^2}{\Delta\lambda} \approx 0.44 \cdot \frac{\lambda_0^2}{\Delta\lambda} \tag{3}$$

In contrast, the lateral resolution is associated with the focused spot size of the sample beam. Therefore, this parameter depends on the numerical aperture of the optical system, given by the focal length f and the size of the incident beam d (see Equation 4).

$$\delta_x = \frac{4\lambda_0}{\pi} \cdot \frac{f}{d} \tag{4}$$

Other OCT technologies have been developed and implemented for ocular imaging in addition to the developmental steps above. These include but are not limited to OCT angiography, polarization-sensitive OCT, OCT in combination with adaptive optics and high-speed OCT. In summary, OCT technology is undergoing constant improvement, which opens up new opportunities for applications, such as in myopia research.

2 Objectives

Before OCT, studies on tissue changes in myopia were limited to animal models with laborious ex-vivo analyses. Later, biometry and time-domain OCT offered the opportunity to expand the studies also to humans and investigate the posterior segment in an in-vivo and real-time manner. However, these technologies were not well-suited for exact measurements of the deeper retinal structures and the choroid due to high measurement noise. The development of spectral-domain and especially swept-source OCT provided improvements in scan depth and scan resolution and were subsequently brought more into focus for myopia-related investigations of retinal and choroidal processes. Some of these processes are proposed as promising biomarkers for long-term indications of ocular growth behavior. Due to the relative novelty of OCT in this field, it is meaningful to evaluate available technologies concerning their suitability of these measurements and to further analyze potential biomarkers with it.

Therefore, the first study investigated the repeatability and agreement of automated choroidal thickness segmentation with two spectral-domain OCT devices in different retinal areas. With the obtained results, it was possible to identify metrologically preferred regions for choroidal thickness measurements. Moreover, previous study findings regarding choroidal thickness changes could be assessed in the context of the measurement noise of spectral-domain technology.

The second project was performed using swept-source OCT with more advanced imaging possibilities and a wider scan field than spectral-domain OCT. Choroidal thickness and choroidal vascularity index were extracted automatically for various retinal regions and correlated to axial length. With these results, normative topographical distributions of the parameters mentioned above and their relation to myopic eye growth could be established.

In the third study, retinal and foveal shape properties were extracted from horizontal and vertical wide-field OCT scans after correction for the scan geometry distortions. The project aimed to identify myopia-specific growth patterns of the posterior segment. These findings could be relevant for future longitudinal studies to investigate ocular growth with a clinically feasible OCT measurement procedure.

The last experiment compared the direct OCT-based measurement of retinal shape to eccentric photorefraction as an exemplary used procedure to indirectly assess retinal shape. The findings helped to understand whether peripheral refraction and retinal shape could be inferred from each other or whether they should be considered as two separate parameters in future research.

3 Repeatability and agreement of automated choroidal thickness segmentation of volumetric spectral-domain OCT scans

3.1 Abstract

In myopia research, changes of choroidal thickness in response to optically induced signals serve as predictor for changes in axial length that might be correlated with myopia progression. Optical coherence tomography (OCT) provides a tool for imaging the choroid, however, with certain difficulties because of a limited visibility of the scleral-choroidal interface. Considering the previously reported effect sizes of thickness change in human myopia research, this study investigated the repeatability of automated 3D choroidal segmentation across the macular area of $6x6\,mm^2$. Fifteen subjects underwent nine volume scans in two OCT devices with analysis of the 95% interval of repeatability, inter-subject and intra-subject variations, as well as interdevice agreement. Repeatability generally improved with increasing eccentricity from the fovea. The nasal perifoveal region exhibited the best repeatability with ±19 and $\pm21\,\mu m$ in both OCT devices, whereas the subfovea showed a repeatability of ±57 and $\pm44\,\mu m$, respectively. High inter- and intra-subject variations were observed, together with a negative bias in the device agreement. Although there is still limited data on thickness changes of the nasal choroid, future studies could focus more on measuring the effect size in the nasal perifoveal area to account for metrological issues in choroidal segmentation.

3.2 Introduction

Optical coherence tomography (OCT) allows in-vivo imaging of retinal structures. Especially imaging the choroid has become of great interest in the field of myopia research [Read et al., 2019a]. Previous studies in animals [Wallman et al., 1995; Hung et al., 2000; Zhu et al., 2005] and humans [Read et al., 2010; Chiang et al., 2015; Wang et al., 2016; Chiang et al., 2018] have shown that the choroid might be capable to change its thickness in a bi-directional fashion in response and in relation to the sign of defocus already after a short period of time and in anti-phase to the axial length.

Moreover, physiological [Brown et al., 2009; Chakraborty et al., 2011; Tan et al., 2012; Usui et al., 2012; Lee et al., 2014; Chakraborty et al., 2018] and defocus-manipulated circadian thickness changes [Chakraborty et al., 2012, 2013] of the choroid gained more interest together with differences in the absolute thickness and distribution patterns of choroidal thickness between myopes and emmetropes [Deng et al., 2018; Jin et al., 2019; Hoseini-Yazdi et al., 2019c]. The aforementioned choroidal reaction, rhythm and global distribution therefore might serve as a predictive biomarker for future axial length development.

However, measuring choroidal thickness changes from OCT images can cause difficulties due to a limited visibility of the choroidal-scleral interface, which is dependent on the absolute choroidal thickness and the pigmentation of the retinal pigment epithelium in healthy eyes [Kong et al., 2016, 2018]. Measurements of choroidal thickness can be performed manually, with semi-automated as well as fully automated segmentation algorithms. Previous studies have investigated the repeatability, correlation and agreement of manual measurements of choroidal thickness by one or more examiners or with different spectral-domain OCT devices [Rahman et al., 2011; Branchini et al., 2012; Yamashita et al., 2012; Shao et al., 2013; Li et al., 2016; Kong et al., 2018]. In addition, various algorithms for (semi-)automated choroidal segmentation have been developed, validated and compared to the manual thickness evaluations, which served as gold standard [Alonso-Caneiro et al., 2013; Chen et al., 2015; Gupta et al., 2015; Twa et al., 2016]. These studies report good correlations of choroidal measurements of approximately $20\,\mu m$. However, they were mainly focused on the subfoveal choroid, with only few of them reporting results from single measurement points outside of the subfoveal region, which were obtained from line scans. Furthermore, the eventual interpretation of the overall reliability of choroidal thickness segmentation and analysis is dependent on the usage of these results with the associated effect sizes. For example, the aforementioned studies in the field of human myopia research have reported choroidal thickness changes of $10\,\mu m$ or even less, whereas clinical applications for choroidal pathologies generally present with considerably higher changes of more than $100\,\mu m$ [Maruko et al., 2010, 2011; Chung et al., 2011], and are therefore less sensitive to metrological influences by the OCT devices and analysis methods.

Thus, the aim of the current study is to evaluate the repeatability and agreement of a published open-source automated segmentation algorithm for OCT volume scans [Mazzaferri et al., 2017] in two different OCT devices (ZEISS CIRRUS HD-OCT 5000, Carl Zeiss Meditec Inc., Dublin, CA, USA and HRA + OCT SPECTRALIS, Heidelberg Engineering, Germany) across the macular area using volume scans instead of multiple line scans.

The overall purpose is to critically define the reliability of OCT measurements in regards to the effect size of choroidal thickness changes/differences with a maximum of 20-30 μm as they have been reported in human myopia research [Read et al., 2010; Chiang et al., 2015; Wang et al., 2016; Chen et al., 2016; Chiang et al., 2018; Breher et al., 2018; Brown et al., 2009; Chakraborty et al., 2011; Tan et al., 2012; Usui et al., 2012; Lee et al., 2014; Chakraborty et al., 2018; Deng et al., 2018; Jin et al., 2019; Hoseini-Yazdi et al., 2019c]. Another aim of the study is to particularly investigate regional differences in the repeatability of choroidal segmentation, in order to give meaningful recommendations for future measurement locations, such that the repeatability of the measurement location itself does not doubt the found effect sizes.

3.3 Results

3.3.1 Subjects

Spherical equivalent refractive errors from objective refraction of the right eye ranged from -0.50 D to -6.25 D with a mean of -3.18 D $\pm$ 2.01 D. Mean choroidal thicknesses in the different Early Treatment of Diabetic Retinopathy Study (ETDRS) [Group et al., 1985] areas are displayed in Figure 7. Generally, the choroidal thickness decreases towards the periphery of the macula. It moreover varies among the ETDRS regions with the nasal area exhibiting the thinnest choroids between 159 ± 46 μm and 232 ± 32 μm, followed by, in increasing order, the inferior regions, the central, temporal and superior areas, that show an almost 100 μm thicker choroid with up to 248 ± 49 μm.
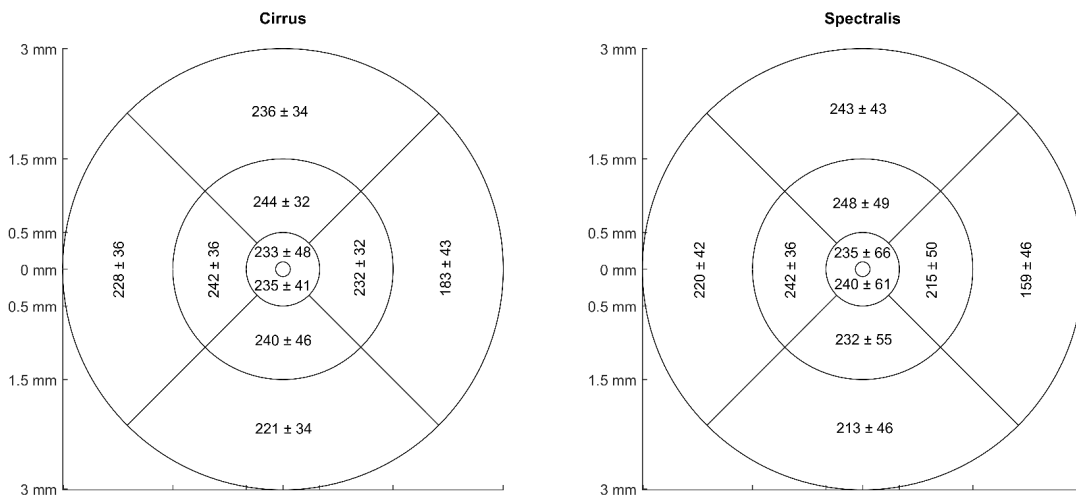
Figure 7: Choroidal thickness (in microns) across the different ETDRS areas averaged over all subjects for the ZEISS Cirrus OCT and the Spectralis HRA + OCT.

3.3.2 Repeatability in the macular area

The repeatability of the analysis of choroidal thickness varies among the different ET-DRS areas of the macula in both devices as seen in Table 1. Generally, the repeatability improves with increasing distance (eccentricity) from the fovea for all ETDRS areas measured with the ZEISS Cirrus, and for all ETDRS except the nasal section when measured with the Heidelberg Spectralis OCT. The repeatability of measurements in the subfoveal region is among the highest values for both devices with 57 μm and 44 μm, whereas the nasal region, especially at the diameter of 6 mm exhibits the best repeatability with 19 μm and 22 μm for both OCT devices. Figure 8 shows the repeatability values from Table 1 in a colour-coded map across the macular area.

	ZEISS Cirrus			Heidelberg Spectralis		
	Repeatability	2.5%	97.5%	Repeatability	2.5%	97.5%
Subfoveal	± 57	-59	55	± 44	-43	45
Central 1 mm	± 43	-42	44	± 34	-34	34
Inferior 3 mm	± 35	-36	34	± 28	-29	27
Superior 3 mm	± 42	-43	42	± 34	-36	33
Nasal 3 mm	± 27	-26	27	± 22	-22	23
Temporal 3 mm	± 31	-33	29	± 24	-23	25
Inferior 6 mm	± 27	-28	27	± 50	-77	22
Superior 6 mm	± 34	-32	35	± 50	-64	35
Nasal 6 mm	± 19	-19	18	± 21	-22	20
Temporal 6 mm	± 23	-23	24	± 23	-23	23

Table 1: Repeatability values with 2.5% and 97.5% limits of the reference intervals of the different ETDRS sections. Repeatability is defined as half the length of the reference interval.
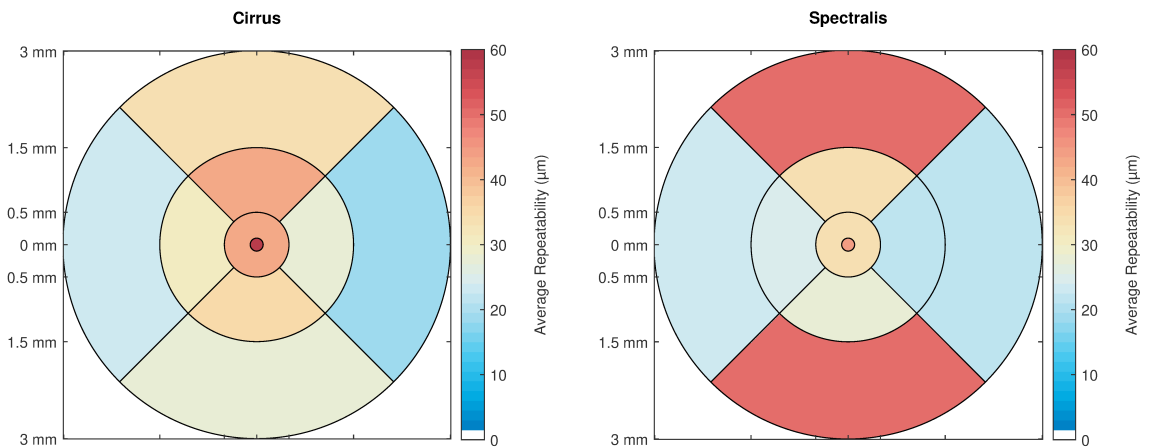
Figure 8: Colour-coded repeatability in the different ETDRS areas of the right eye as measured with both OCT devices.

3.3.3 Inter-subject and intra-subject variability

The repeatability varied greatly between the individual subjects as can be seen on Figure 9 in the top two plots A and B. The average difference to the mean - not to be confused with the 95% reference interval derived from the cumulative distribution function (CDF) as described in the methods section and reported in Table 1 - for all subjects in the subfoveal region was $17 \pm 11\,\mu m$ and $13 \pm 9\,\mu m$ for both OCT devices, respectively. However, the individual differences ranged from $4\,\mu m$ to $39\,\mu m$ (ZEISS Cirrus) and from $3\,\mu m$ to $38\,\mu m$ (Heidelberg Spectralis). In contrast, the perifoveal nasal ETDRS section showed generally lower averaged differences to the mean with $6 \pm 3\,\mu m$ with a range of $2\,\mu m$ to $13\,\mu m$ for both OCT devices.

However, analysis of choroidal thickness did not only vary between subjects but also within the single subjects. If the intra-subject standard deviation was high, this indicated that the choroidal thickness analysis in this subject led to very different results. Figure 9 gives an overview about the standard deviation of the differences to be mean across the study population in the bottom row plots C and D. Exemplarly, the subfoveal region showed the highest range of intra-subject variability from $5\,\mu m$ and $4\,\mu m$ up to $51\,\mu m$ and $44\,\mu m$, for each of the OCT devices. In contrast, the outermost nasal section exhibited the least standard deviations for single subjects with on average $7 \pm 4\,\mu m$ measured by ZEISS Cirrus, and $8 \pm 4\,\mu m$ by Heidelberg Spectralis OCT.

3.3.4 Agreement between both devices with automated choroidal segmentation

Bland–Altman analysis [Bland and Altman, 1999] and Intraclass correlation (ICC) [McAlinden et al., 2011] coefficients were used for statistical analysis of the agreement of choroidal thickness measurements between both devices. Results are shown in Table 2 (limits of agreement), Table 3 (ICC) and Figure 10 (Bland-Altman plots). It is noteworthy that the choroidal thickness analysis yielded constantly higher thickness values for the ZEISS Cirrus than for the Heidelberg Spectralis, which is indicated by the negative bias of the mean differences in Table 2. The superior regions showed here the least bias but widely spread limits of agreement in contrast to the nasal areas with the highest mean difference but smallest limits of agreement. However, for all other ETDRS areas, the limits of agreement and their associated 95% confidence intervals become smaller with increasing retinal eccentricity. This relationship is confirmed by the ICC coefficients in Table 3.
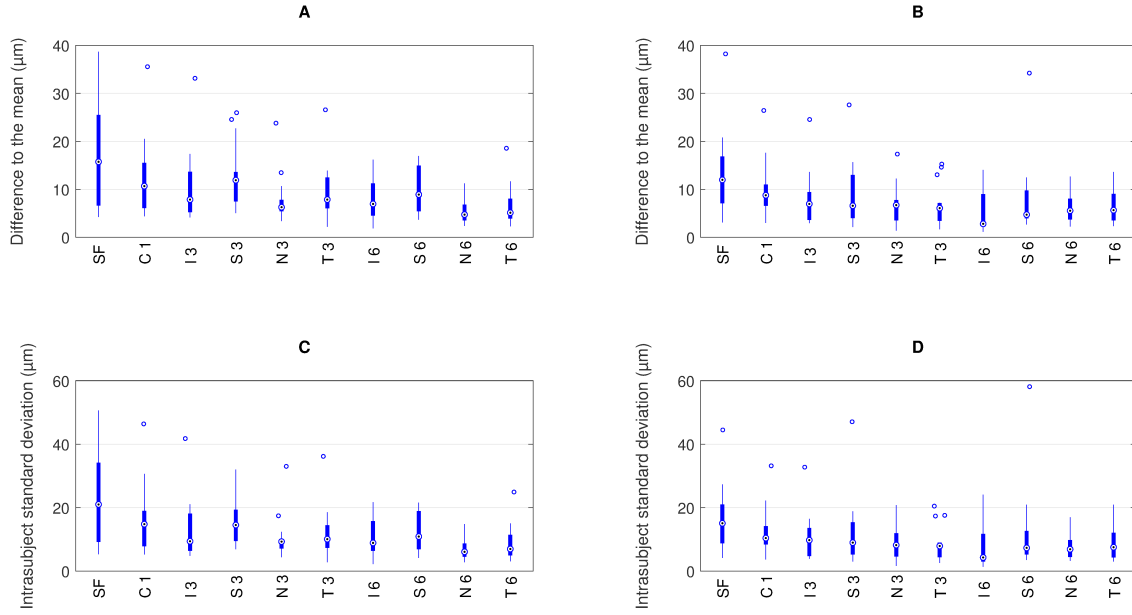
Figure 9: Difference to the mean from all subjects across the different ETDRS regions to describe the variability between subjects for ZEISS Cirrus (A) and Heidelberg Spectralis (B). Standard deviation of the raw choroidal thickness measurements from all subjects across the ETDRS regions to describe the variability within one subject for ZEISS Cirrus (C) and Heidelberg Spectralis (D). Note that the abbreviations of the ETDRS areas on the x-axis are composed of the specific region and its diameter in mm.

	MD (µm)	95% LoA (µm)	95% CI upper limit (µm)	95% CI lower limit (µm)
Heidelberg Spectralis vs. ZEISS Cirrus				
Subfoveal	-14	± 73	20 to 98	-125 to -48
Central 1 mm	-10	± 63	20 to 87	-107 to -39
Inferior 3 mm	-25	± 47	-3 to 46	-96 to -47
Superior 3 mm	-5	± 60	28 to 103	-113 to -38
Nasal 3 mm	-28	± 25	-16 to 10	-66 to -39
Temporal 3 mm	-13	± 55	12 to 71	-98 to -39
Inferior 6 mm	-17	± 45	4 to 52	-86 to -38
Superior 6 mm	-1	± 64	29 to 97	-100 to -31
Nasal 6 mm	-24	± 31	-9 to 23	-71 to -39
Temporal 6 mm	-19	± 35	-2 to 36	-73 to -35

Table 2: Mean differences, limits of agreement (LoA) and their 95% confidence intervals (CI) for each retinal area. Negative mean differences mean that the choroidal thickness measurements obtained by the ZEISS Cirrus OCT were thicker than these obtained by the Heidelberg Spectralis OCT.

	ICC	95% CI	
		Lower	Upper
Subfoveal	0.773	0.29	0.93
Central 1 mm	0.804	0.39	0.94
Inferior 3 mm	0.902	0.69	0.97
Superior 3 mm	0.633	-0.14	0.88
Nasal 3 mm	0.965	0.89	0.99
Temporal 3 mm	0.842	0.51	0.95
Inferior 6 mm	0.884	0.64	0.96
Superior 6 mm	0.682	0.01	0.90
Nasal 6 mm	0.968	0.90	0.99
Temporal 6 mm	0.916	0.74	0.97

Table 3: ICC coefficients with 95% confidence intervals for the retinal areas. The nasal areas show excellent correlations compared to the subfoveal and superior sections with the lowest coefficients but still good overall correlation.
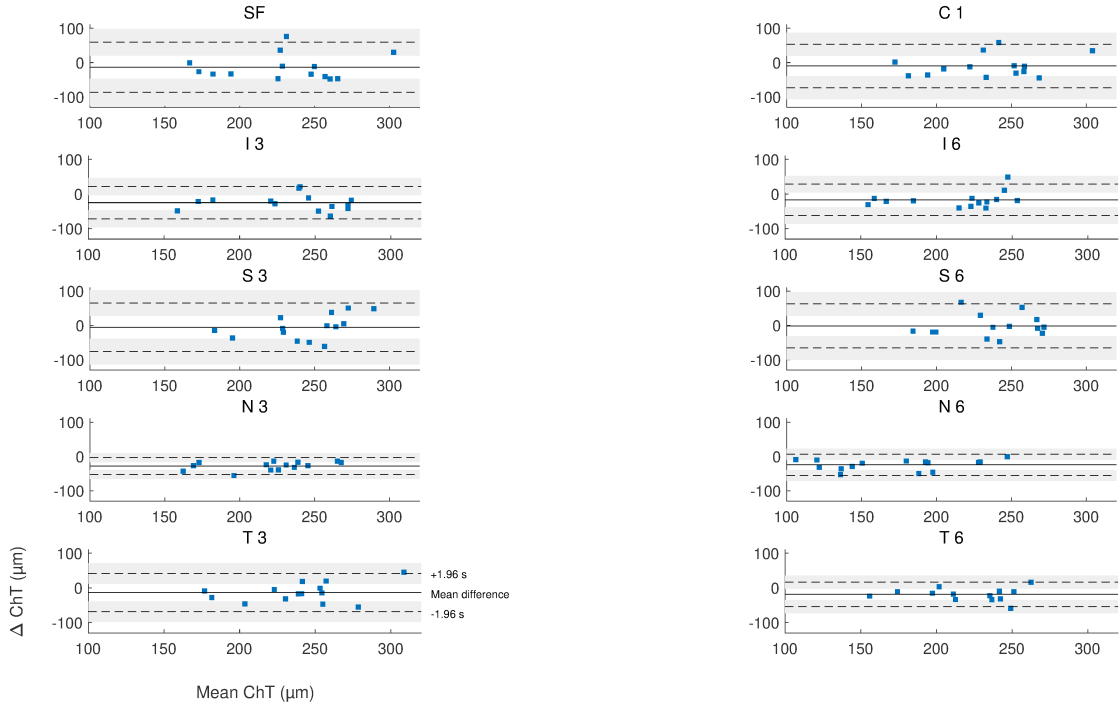
Figure 10: Bland-Altman plots for comparison of choroidal thickness analysis between both OCT devices for the single ETDRS areas. The x-axes of the plots show the mean of ChT measurements in both devices, the y-axes the difference between them. The subfoveal and superior regions show the most spreaded intervals of agreement in contrast to the nasal areas.

3.4 Discussion

The current study evaluated the overall repeatability, inter-subject and intra-subject repeatability, as well as agreement of choroidal thickness measurements in two OCTs across the macula. To our best knowledge, this is the first study that analyzed choroidal thickness with automated segmentation [Mazzaferri et al., 2017] and further split into the different ETDRS regions for separate analysis. The results showed consistently better repeatability in the nasal section compared to the other measured areas, especially in the case of the central and subfoveal divisions. One obvious reason for the better repeatability nasally could present the thinner choroidal thickness in that area, which allows better scan depth into the tissue, thus clearer imaging of the choroidal-scleral interface and therefore more reliable segmentation. However, this reasoning stands in contradiction to the worse repeatability of the inferior compared to the relatively thicker temporal choroid. Bland-Altman analysis also showed that the nasal quadrants indeed show the highest mean difference, however, they also show the smallest limits of agreement and the highest ICC coefficients. Together with the good repeatability value in those area indicates that the choroidal thickness might differ significantly between both OCTs in absolute numbers but still are reliable from a relative point of view. However, this absolute bias becomes less important in human myopia studies examining changes in response to e.g. optical defocus, where usually only the relative difference before and after exposure to defocus are measured with the same OCT device.

Moreover, previous studies using automated choroidal thickness analyses showed varying results in regards of repeatability. Twa et al. [2016] automatically analyzed line scans taken one hour apart from each other with resulting limits of agreement of $14\,\mu$m. However, they did not distinguish between retinal locations for their analysis. Gupta and colleagues [Gupta et al., 2015] applied a 7-line macular volume scan protocol with $10\,$min breaks between the single scans. With their segmentation algorithm they measured choroidal thickness at the subfoveal region, nasally and temporally at $1.5\,$mm and $3\,$mm locations. These points represent the borders of the ETDRS sections in horizontal direction. They observed an excellent intra-session correlation with less pronounced differences between the evaluated locations. Moreover, the results indicated the highest repeatability subfoveally and nasally which worsened towards the temporal regions. These observed discrepancies might derive from different methodological approaches, as the present study averaged all the choroidal thickness measurement points within each ETDRS area in contrast to single points being assessed.

Mansouri et al. [2014] measured the same-sized macular area and found an excellent correlation between consecutive measurements. However, they averaged the choroidal thickness across the entire scanning area, while also using a swept-source OCT compared to the spectral-domain devices that were used in the current study. Most recently, the wide-field repeatability of a semi-automated algorithm was tested with multiple B-scans across a field of 45x55° using a wide-field lens [Hoseini-Yazdi et al., 2019b]. This resulted in a repeatability even lower than the axial resolution of the spectral-domain OCT, down to 2-3 μm if whole quadrants (nasal, temporal inferior, superior) across the retinal areas are averaged. By evaluating the repeatability as a term of eccentricity, they found the foveal repeatability to be 27 μm and improving towards the periphery down to 16 μm. These results are in line with the results of the current study from a relative perspective, while the absolute numbers are not comparable due to differently sized measurement areas.

For a more direct numerical comparison between automated and manual segmentation, only the previous studies with reported coefficients of repeatability are discussed. These studies also found coefficients between 17 μm and 49 μm for the subfoveal region [Rahman et al., 2011; Cho et al., 2014], and between 27 μm and 63 μm if averaged across the macular region [Chen et al., 2012; Vuong et al., 2016]. As this experiment was focused on comparisons of automated choroidal segmentation between different macular areas, rather than the comparison between manual and automated segmentation per se, the discussion part will not further cover the comparison between manual and automated segmentation for different OCT devices, techniques and parameters, which can be found elsewhere [Alonso-Caneiro et al., 2013; Chen et al., 2015; Zheng et al., 2016; Twa et al., 2016].

It should be noted that the aforementioned studies using automated segmentation reported the repeatability in form of ICC coefficients and/or limits of agreement, while the current study described the reference interval as non-parametric alternative to the within-subject standard deviation derived from Analysis of Variance (ANOVA), which can be considered as a measure of repeatability with the according units of measurement (here μm) for two or more repeated measurements [Bland and Altman, 1999; McAlinden et al., 2011]. This approach in units of measurement allows the direct metrological comparison to actually reported changes of choroidal thickness in human myopia research. Previous studies found effect sizes up to 20 μm, on average around 10 μm or even less in the subfoveal choroid in response to optically induced signals, while these reported effect sizes were accompanied by high standard deviations [Read et al., 2010; Chiang et al., 2015; Wang et al., 2016; Chen et al., 2016; Chiang et al., 2018; Breher et al., 2018].

The same accounts for circadian rhythms and absolute thickness differences in the range of approximately $30\,\mu m$ [Brown et al., 2009; Chakraborty et al., 2011; Tan et al., 2012; Usui et al., 2012; Lee et al., 2014; Chakraborty et al., 2018, 2012, 2013; Deng et al., 2018; Jin et al., 2019; Hoseini-Yazdi et al., 2019c]. Thus, the currently described measurement repeatability of subfoveal choroidal thickness highly exceeds the previously found effect sizes, which doubts the observed results from a metrological perspective. As a consequence, it would be more appropriate to analyze changes of choroidal thickness more preferably in the nasal para- and perifoveal regions, since it shows the best repeatability. However, only limited data is available on the choroidal reactions in these areas, especially from optical interventions. Choroidal thickness in respsonse to three weeks of Orthokeratology lens wear revealed the least amount of thickness change in the nasal area [Chen et al., 2016] compared to temporally and subfoveally, whereas short-term multifocal contact lens wear showed the highest respsone in the nasal region regions [Breher et al., 2018]. Further research needs to be conducted to evaluate the possible advantages of analyzing the nasal or temporal retinal areas in the appropriate eccentricities from the fovea in order to detect choroidal thickness changes more reliably in regards to the repeatability of measurements.

Moreover, general statistical pitfalls by analyzing the inter-subject variations in repeatability were worked out in the analysis process. Despite the advantages of using a single and concrete statistical value to express repeatability, such as coefficients of repeatability, reference intervals, ICC coefficients or limits of agreement, these approaches lack a differentiation between subjects. As already observed during the scan acquisition but also later during the analysis of the results, there is a high inter-subject variation in repeatability. This means that an effect size, e.g. the change of choroidal thickness in response to myopic defocus, of $10\,\mu m$ can be already significant for one subject with a very good repeatability, but not for the other subject with a worse repeatability.

The current study also faces some limitations by itself. First of all, it included a relatively low number of participants for a repeatability analysis. However, the current study primarily aimed to evaluate the repeatability and especially its regional differences in volume scans across the central $6x6\,mm^2$ retina. Although the absolute repeatability value might change in one or the other direction with an increased number of participants, the relative differences between the retinal areas most probably will persist, mainly because of choroidal thickness differences and thus associated visibility of the choroidal-scleral interface [Kong et al., 2016, 2018]. The current study also waived to consider magnification effects, which lead to increasing scan fields sizes with increasing myopic refractive error of the study participants and therefore potentially differently sized ETDRS areas.

Resulting magnification effect from refractive errors between -0.5 D and -6.25 D translate to a maximum scan field difference of ± 0.35 mm, which again translates to maximum ± 30 pixels that might be inaccurately distributed. However, the current study did not evaluate single retinal point locations – which surely would be more affected by these magnification effects – but instead the median value of each of the ETDRS regions was calculated to increase the robustness against magnification effects of the following analysis. Moreover, the parameters for scan acquisition were set equally in both OCT devices except for the number of B-scans in the volume scan. Even though the algorithm interpolates missing image information in both cases, this inequality could have created the differences of repeatability between both devices. Moreover, to ensure equality of the image quality itself for the choroidal segmentation, only one frame per B-scan was averaged. Image averaging, also termed "automated real time averaging" (ART) for the Heidelberg Spectralis OCT, is capable to reduce the speckle noise and lower signal-to-noise ratio of the scan images [Alonso-Caneiro et al., 2011]. Further studies are required to evaluate whether averaging more frames per B-scan would improve the overall repeatability across the macula with automated choroidal segmentation. Additionally, the current study was conducted with only one segmentation algorithm, which was originally developed for the Heidelberg Spectralis and its resulting scan image properties in regards to further image processing. Other algorithms might deliver different results than reported here. However, the current study also showed the successful implementation and usage of the algorithm for the ZEISS Cirrus OCT scans.

One definite advantage of automated algorithms is the fast evaluation without influences from human examiners. It also enables the analysis across a broader retinal area with multiple B-scan images in a volume scan, which would be too time intensive if segmented manually. However, this study showed that there is potential for improvement in the future. For example, the algorithms can be refined to notice even smaller amplitudes of changes on exact pixel level and therefore OCT resolution level during image processing and analysis of the scans for a better detection of the scleral-choroidal border. The OCT technology itself also undergoes a constant improvement: from time-domain to spectral-domain devices, later with EDI technology, to the newly introduced swept-source devices. This development is accompanied by constantly improving scan resolution and scan depth, for example with swept-source OCTs that provide an approximately three times higher scan depth and therefore a more complete visualization of the choroid. This progress will facilitate the choroidal analysis in human myopia research in the future, as it will likely allow more accurate measurements of changes in choroidal thickness compared to the repeatability from the metrological perspective [Mansouri et al., 2014; Jin et al., 2016].

In conclusion, the present study found variations of repeatability of automated choroidal thickness analysis across the macular area, across subjects and even within the same subject for both OCT devices. As observed, the repeatability improved with increasing eccentricity from the fovea and was found to be better in the nasal regions of the retina. Therefore, upcoming studies with automated choroidal segmentation should focus on the analysis of choroidal thickness changes in the nasal para- and perifoveal retina additionally to the subfovea. Ongoing development in OCT technique, such as swept-source OCT, will allow more precise measurements of choroidal thickness and associated changes in human myopia research in the future.

3.5 Methods

3.5.1 Subjects

The prospective study adhered to the tenets of the Declaration of Helsinki and was approved by the ethics committee of the Faculty of Medicine of the University Tuebingen. Written informed consent was obtained from all participants. Fifteen subjects aged between 24 years and 37 years with no reported ocular pathologies were enrolled in the study. One subject was excluded as outlier for the agreement comparison as the averaged thickness measurements differed more than $100\,\mu m$ between both devices.

3.5.2 OCT devices and scan protocol

Study measurements were performed with two different OCT devices based on spectral-domain technology: ZEISS Cirrus (ZEISS CIRRUS HD-OCT 5000, Carl Zeiss Meditec Inc., Dublin, CA, USA) and Spectralis (HRA + OCT SPECTRALIS, Heidelberg Engineering, Germany). Both devices are able to perform volume scans that consist of multiple B-Scans in a defined retinal area. They are also equipped with an eye-tracking software to minimize motion artifacts during scan acquisition. Moreover, the enhanced depth imaging (EDI) or zero delay method, respectively, was used for a better visualization of the choroid. Other scan settings were also set to match each other as closely as possible. The scan area in both devices covered 6x6 mm^2 for the ZEISS Cirrus and 20x20° for the Heidelberg Spectralis, respectively. Furthermore, one B-Scan consisted of 512 A-Scans in both devices, with a frame averaging number of 1 B-Scan. The volume scan for the ZEISS Cirrus consisted of 128 B-Scans, for the Heidelberg Spectralis of 193 B-Scans in total. Participants underwent nine OCT 3D volume scans with each of the devices on their undilated right eyes. The scans were always obtained by the same examiner. The order of the OCT devices was randomized for each participant. The subjects were instructed to move their head out of and back onto the chin and head rest between the individual scans.

3.5.3 Choroidal segmentation

Automated choroidal segmentation and thickness analysis was performed with an open-source MATLAB (MATLAB 2017b, The MathWorks, Inc. Natick, MA, USA) software (available online: https://www.mathworks.com/matlabcentral/fileexchange/61275-choroidsegmentation) [Mazzaferri et al., 2017]. Each B-scan of the volume scan was segmented with an resulting matrix as 2D choroidal thickness map. It displays the choroidal thickness of the corresponding retinal location of the scan points with the fovea being assumed in the centre of the scan. Despite the eye tracking software in both OCT devices, the thickness values around the foveola were averaged in the size of a regular microsaccade [Martinez-Conde et al., 2009], in order to obtain the subfoveal choroidal thickness. The rest of the thickness map was divided into the nine ETDRS sections with diameters of 1 mm, 3 mm and 6 mm [Group et al., 1985] and the median was calculated for each of the regions.

3.5.4 Statistical data analysis

MATLAB and Excel (Microsoft Excel 2016, Microsoft Corporation, Redmond, WA, USA) software was used for the statistical analysis of the data. ANOVA analysis with within-subject standard deviation as conventional repeatability measure was not applicable since the data within the different ETDRS regions did not follow a normal distribution, as tested by the Kolmogorov-Smirnov Test. Nevertheless, to obtain a single value for the repeatability in every ETDRS section, the mean of the nine measurements per subject was subtracted from each of the the nine measurements. The resulting differences to the mean from all subjects per retinal area were then evaluated in a CDF. The 2.5% and 97.5% limits of the cumulative distribution function were identified, multiplied by a correction factor of $\sqrt{3/2}$ for centered data and considered as the limits of the 95% reference interval. Half of the length of the reference interval was then defined as the repeatability value for the analyzed ETDRS region [ISO / IEC Guide 100:2008, 2008].

To analyze the variability and ranges of inter-subject repeatability, the absolute differences to the mean for each subject per ETDRS area were averaged. The standard deviation of the raw choroidal thickness values per subject describe the intra-subject variability of repeatability. These statistical approaches were chosen over the previous methodology using the 95% reference interval, due to the limited statistical and informative value of a CDF with only nine values for each separately analyzed subject. Given that, the values for the inter-subject and intra-subject variability of repeatability are lower than the general repeatability value reported for all subjects.

To compare the agreement of choroidal thickness analysis for both OCTs, the limits of agreement from the nine averaged choroidal thickness measurements in the different ETDRS sections were calculated via Bland-Altman analysis [Bland and Altman, 1999] and ICC coefficients with ICC(2,k) [Shrout and Fleiss, 1979].

Data availability

The datasets generated during and/or analyzed during the current study are available from the corresponding author on reasonable request.

Author contributions statement

KB conducted the measurements and analyzed the data. AO and SW conceived and supervised the study. All authors were involved in the writing process of the manuscript.

Competing interests

This work was done in an industry-on-campus-cooperation between the University of Tuebingen and Carl Zeiss Vision International GmbH. Author KB declares no potential conflict of interest. AO and SW are employed by Carl Zeiss Vision International GmbH and are scientists at the University Tuebingen.

4 Metrological and topographical aspects of choroidal thickness and vascularity measurements using swept-source OCT

4.1 Abstract

Purpose: Choroidal thickness (ChT) and choroidal vascularity index (CVI) represent two important metrics in health-, disease-, and myopia-related studies. Wide-field swept-source optical coherence tomography (OCT) provides improved and extended imaging and extraction of choroidal variables. This study characterizes the topography and repeatability of these parameters in healthy eyes.

Methods: Swept-source OCT volume scans were obtained on 14 young adult patients on three separate days. ChT and CVI were automatically corrected for image magnification and extracted for different enface regions within an extended ETDRS grid of 10mm diameter. Topographical distribution, correlation to ocular length, and inter-session repeatability of both choroidal parameters were assessed.

Results: CVI showed little fluctuation between subfields, unlike ChT, which demonstrated thinning towards the peripheral choroid (coefficients of variation 5.92 vs 0.89). ChT showed a consistent negative correlation with axial length ($\rho = $-0.05 to -0.61), although this was only statistically significant in the inner superior subfield (P = 0.02). There was no consistent or significant relationship between CVI and axial length or between CVI and ChT. The repeatability of CVI measurements (3.90% – 5.51%) was more consistent between scan regions than ChT measurements (10.37 – 20.33 μm).

Conclusions: CVI values were consistent across the central 10mm of the retina, while ChT reduced with eccentricity. The repeatability of both parameters is similar to the effect size reported in many studies using the choroid as a biomarker, which should be considered in the interpretation of findings.

Translational Relevance: This study provided normative as well as metrological information for the clinical interpretation of ChT and CVI in health and disease.

4.2 Introduction

The choroid is located between the retina and the sclera and consists of five layers - Bruch's membrane, choriocapillaris, Haller's layer, Sattler's layer, and the suprachoroid - with its main task to provide blood supply to the outer retina [Hogan, 1971; Nickla and Wallman, 2010].

The choroid is suggested to play an essential role in various fields of human eye research. Changes to the choroidal structure have been suggested as biomarkers for a variety of ocular pathologies; altered choroidal thickness (ChT) was previously observed in central serous chorioretinopathy [Maruko et al., 2010], Vogt-Koyanagi-Harada disease [Maruko et al., 2011], and polypoidal choroidal vasculopathy and exudative age-related macular degeneration [Chung et al., 2011]. Moreover, bidirectional changes of ChT influence the regulation of eye growth due to its location in the signaling pathway from retina to sclera [Wallman et al., 1995; Nickla and Wallman, 2010]. However, the exact physiologic mechanisms behind the observed ChT changes still require further clarification. It is assumed that the fast alterations are based on adjustments of the vascular rather than stromal components [Nickla and Wallman, 2010; Wang et al., 2016; Fitzgerald et al., 2002; Zhang et al., 2019; Li et al., 2017]. Therefore, choroidal vascularity developed as a further subject of interest in human eye research. The term "choroidal vascularity index" (CVI) was introduced as the ratio of luminal area to total choroidal area. The higher the CVI, the more vascular tissue compared with stromal tissue is present in the choroid [Agrawal et al., 2020]. CVI was previously investigated in a healthy study population [Agrawal et al., 2016b], as well as in ocular pathologies, such as diabetic retinopathy [Tan et al., 2016], central serous chorioretinopathy [Agrawal et al., 2016a], age-related macula degeneration [Wei et al., 2017], panuveitis, [Agrawal et al., 2016c] and retinitis pigmentosa [Tan et al., 2018]. While there are only a few studies existent, they report only vague and somewhat inconsistent association between choroidal vascularity and myopia [Li et al., 2020; Alshareef et al., 2017a,b; Gupta et al., 2017].

ChT and CVI can be obtained from optical coherence tomography (OCT) images. After segmentation of the choroidal area, the hyporeflective blood vessel lumina are distinguished from the hyperreflective stromal tissue. The reliability of the results from graphical analysis strongly depends on the OCT technology (scan depth, scan resolution and image contrast) [Agrawal et al., 2020; Iovino et al., 2020] but also on subject factors (absolute choroidal thickness and the pigmentation of the retinal pigment epithelium [Kong et al., 2016, 2018]). Therefore, these parameters influence the repeatability of ChT and CVI measurements.

The repeatability metric helps to differentiate between measurement noise and true measured effect, which is pertinent for interpreting study findings. This becomes essential when effect sizes are small, in combination with high inter-subject variability, as is typical of studies of the choroid.

Therefore, the purpose of this study is to evaluate the repeatability of ChT and CVI measurements metrologically and to put them into the context of commonly found effect sizes in choroidal research. Moreover, the topographic distribution across an extended scan area, as well as the relationship between choroidal parameters and axial length, is assessed. To our knowledge, this is the first study for this purpose using automated analysis of wide-field volume scans from swept-source OCT.

4.3 Materials & Methods

4.3.1 Study participants

The prospective and cross-sectional study adhered to the Declaration of Helsinki and was approved by the ethics committee of the Faculty of Medicine of the University Tuebingen. Written informed consent was obtained from all participants prior to data collection. Fifteen patients without known ocular pathologies were enrolled in the study. One patient was excluded from analysis due to erroneous choroidal segmentation resulting from small pupil size and thus reduced image quality. The study participants included in the analysis had a mean age of 27 ± 3 years (range, 24 - 37 years) and an average axial eye length (AEL) of 24.83 ± 0.91 mm (range, 23.12 - 26.52 mm).

4.3.2 OCT scanning protocol

Participants underwent nine OCT volume scans on their undilated right eye, using swept-source OCT (ZEISS PlexElite 9000, Carl Zeiss Meditec Inc., Dublin, CA, USA). The OCT device uses a central wavelength between 1040 and 1060 nm and a sweep range from 980 to 1120 nm, resulting in an increased scan depth of 3 mm. The axial and lateral resolutions in tissue are 6.3 μm and 20 μm, respectively. Three consecutive scans were performed, at the same time of day on three separate days, to control for diurnal variations in choroidal structure [Lee et al., 2014; Tan et al., 2012]. Moreover, participants were advised to avert caffeine [Dervişoğulları et al., 2016; Zengin et al., 2015] and nicotine [Zengin et al., 2014] at least 1 hour prior to the measurement to avoid short-term changes of ChT. In order to wash out near work-induced accommodative choroidal thinning [Woodman et al., 2012; Woodman-Pieterse et al., 2015] and to stabilize blood pressure [Tan et al., 2012], participants completed a 10-minute resting phase with distance viewing.

For the current study, a 12 x 12 mm isometric volume scan centered on the fovea was chosen. This scan pattern consisted of 1024 B-scans with 1024 A-scans per B-scan. Eye tracking, enhanced-depth imaging, and follow-up mode were enabled to reduce motion artifacts, to enhance the visibility of the choroid, and to ensure a constant scanning area throughout all scans. The same experienced examiner obtained all scans. Furthermore, participants moved their head off of and back onto the chinrest and headrest between each scan.

4.3.3 Extraction of choroidal thickness

Choroidal segmentation was performed automatically by image processing of each volume scan via the Advanced Retinal Imaging Network (ARI Network, Carl Zeiss Meditec Inc., Dublin, CA, USA). The ARI Network represents a research portal provided by Carl Zeiss Meditec Inc., which offers various algorithms for researchers using the PlexElite 9000 OCT device. The choroidal segmentation algorithm uses a graph-based approach with a combination of intensity, axial gradient, gradient magnitude, and positional information to segment the RPE and the choroidal-scleral interface. To save time and increase segmentation reliability in volume scans with multiple adjacent B-scans, a subset of B-scans is segmented first. The remaining B-scans are segmented considering the results from the first subset. Exemplary central and peripheral B-scans of the scan were checked for segmentation errors by the examiner [Bagherinia et al., 2019].

The choroidal thickness map for the entire scan area was extracted as a two-dimensional matrix in pixels and was further processed in MATLAB (MATLAB 2020a, The MathWorks, Inc. Natick, MA, USA). An axial conversion factor of 1.9531 from pixel to microns was applied, which is based upon the ratio of true scan depth $(3000\,\mu m)$ to digital image scan depth (1536 pixels). Subsequently, a modified extended Early Treatment of Diabetic Retinopathy Study (ETDRS) grid [Early Treatment Diabetic Retinopathy Study Research Group, 1985] was overlaid on the segmented choroidal thickness map (Figure 11). It consisted of four rings with baseline radii of 0.5 mm (central), 1.5 mm (inner), 3.0 mm (outer), and 5.0 mm (extended). The three outer rings were further divided into nasal, temporal, superior, and inferior sectors. The ETDRS grid size was adjusted for the AEL (Equation 6) of the participant (ZEISS IOLMaster 700, Carl Zeiss Meditec AG, Jena, Germany) to compensate for the individual ocular magnification. Data from the optic nerve head (ONH) was selected and subsequently excluded via a semi-automated approach due to inherent segmentation errors in this region.

The ONH was excluded by presenting the examiner with an en-face stack image and prompting the user to select with their cursor two points that define the diameter of a circle. This circle was later used to define an exclusion zone for calculations of CVI. These steps are described in more detail in the following section.

4.3.4 Extraction of choroidal vascularity index

The novel CVI calculation algorithm is written in MATLAB (MATLAB 2019b, The MathWorks, Inc. Natick, MA, USA) and makes use of the Parallel Computing Toolbox for parallelized "for" loops with slices of the volume sent to each worker node in turn for processing. The user interface for this code is in the form of Windows dialogues and figure plots, which request cursor click positions for various tasks. The code also relies on the preparation of a data file, listing the filenames of the volume scans, along with the AEL of each scan. The scan itself is stored as an 8-bit unsigned grayscale image. The procedure for calculating CVI for an image once it is loaded into MATLAB is adapted from the protocol of Sonoda et al. [Sonoda et al., 2014, 2015] and is outlined below.

The volume scan is extracted from the input file and stored in a three-dimensional matrix. The RPE segmentation and choroidal thickness map are stored in a matrix, and the segmentation for the choroidal-scleral boundary is calculated by summing the RPE segmentation matrix and the choroidal thickness matrix. The AEL is also extracted from the input files. To give the algorithm a baseline to quantify the grayscale value of a typical fluid, the average voxel value is taken in the two non-en-face planes of the scan, at 50% of the width of the slice, and 75% of the height of the slice (assumed to be within the vitreous). This value is referred to as the "liquid norm". A mask is then created that specifies the region of interest (ROI) for analysis. From the RPE and choroidal segmentation data, a three-dimensional binary mask matrix is generated, holding a value of 1 within the ROI and 0 outside the ROI. For normalization of the image, the liquid norm is used as a lower threshold on the volume scan (i.e. all values below the threshold were set to zero), and voxel values were re-scaled between 0 and 255.

To reduce speckle and assist with thresholding, a median blur was applied to each slice in the scan using a 3 x 3 window. The volume scan was binarized using Niblack auto local thresholding [Niblack, 2003] over each slice of the scan, whereby a moving circular window of radius 20 pixels specified the binarization threshold. The threshold, T, was calculated from the local mean, m, and local standard deviation, σ, of the pixels in the window, along with a parameter k, which was set to 0.2.

$$T = m + k \times \sigma \tag{5}$$
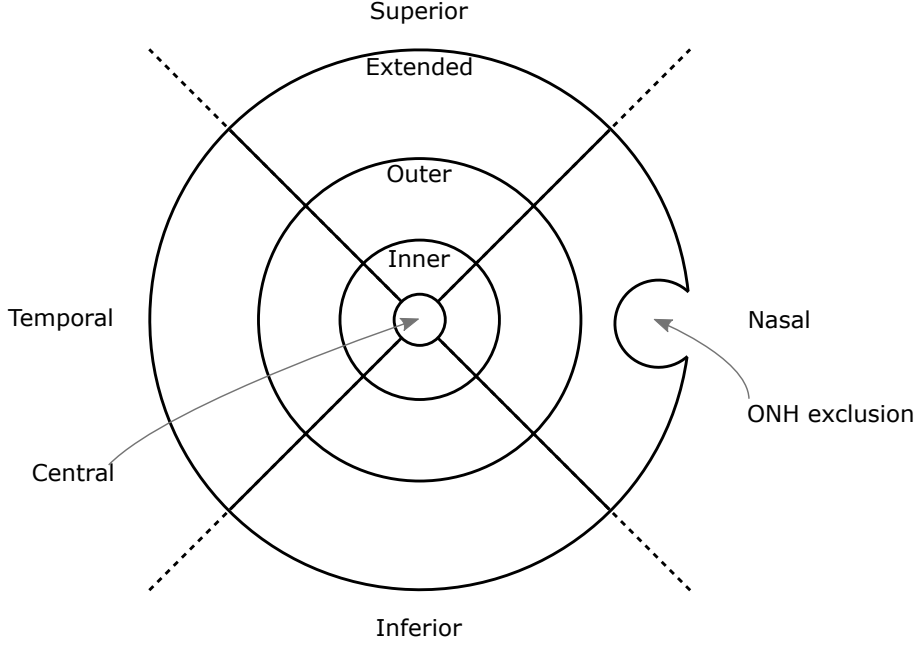
Figure 11: Extended ETDRS grid, showing the optic nerve head exclusion zone for a right eye. The ring diameters are 1mm, 3mm, 6mm, and 10mm.

Any value above the threshold was set to 1, and values below were set to 0, thus producing a binarized image.

This study made use of an extended ETDRS grid, centered on the fovea, with an extended diameter of 10 mm and exclusion of the optic nerve head region (Figure 11). Careful lateral scaling was performed for each image, to account for the effects of ocular biometry on OCT magnification [Terry et al., 2016]. In the lateral dimension, the length each pixel, represented in mm p_{mm}, was given by:

$$p_{mm} = \frac{(l_a - \Delta_{cp}) \, \theta_{air}}{d_p n_B} \tag{6}$$

where l_a is the AEL, Δ_{cp} is the distance between the cornea and principal plane and is given as 1.82mm [Bennett et al., 1994], θ_{air} is the scan angle (in radians) of the OCT in air and is 40° for this study, d_p is the dimension of the en-face scan in pixels, and n_B is the bulk refractive index of the ocular humors which is taken as 1.336.

The 13 ETDRS grid regions were stored as two-dimensional Boolean mask matrices. Each matrix was also masked against the optic nerve head exclusion circle; typically this intersected with the extended nasal grid cell.

The CVI was calculated from each voxel column of an en-face view to create a map of CVI for the scan. Within the ROI of each column, the number of voxels representing vessel lumen was counted, n_v, and the total number of voxels in the ROI column was counted, n_{ROI}. The CVI for each column was calculated as:

$$CVI_{col} = \frac{n_v}{n_{ROI}} \times 100 \tag{7}$$

This CVI map was stored and presented as an image with an ETDRS grid overlay. Finally, the CVI for each of the ETDRS regions was calculated by summing the total number of voxels representing the vessel lumen in the grid region within the ROI, N_v, and the total number of voxels in the ROI within each region, N_{ROI}. The CVI for each region was calculated as:

$$CVI_{reg} = \frac{N_v}{N_{ROI}} \times 100 \tag{8}$$

4.3.5 Statistical data analysis

MATLAB (MATLAB 2020a, The MathWorks, Inc., Natick, MA, USA) was used for statistical analysis. Normality of the data was tested with the Lilliefors test. For the analysis of topographical distribution, measurements from all nine scans were averaged per patient and are presented as a median and interquartile range (IQR). The quartile-based coefficient of variation [Zwillinger and Kokoska, 1999] (CV) was calculated (Equation 9), where Q_{25} and Q_{75} denote the 25th and 75th quantile of the distribution.

$$CV = (\frac{Q_{75} - Q_{25}}{Q_{75} + Q_{25}}) \times 100 \tag{9}$$

Correlations of the choroidal parameters with AEL were performed using Spearman's rank correlation [Myers and Sirois, 2004]. The coefficient of repeatability (CR) from nonnormal data was derived for each ETDRS region as explained elsewhere [ISO / IEC Guide 100:2008, 2008; Breher et al., 2019b]. In short, the median of each of the three measurements per day and its difference to the overall mean across the 3 days were calculated. Subsequently, the resulting deltas were evaluated in a cumulative distribution function. The 95% limits of the cumulative distribution function were determined and multiplied by $\sqrt{3/2}$ as a correction factor for centered data. The CR was considered as half the length of the 95% interval. It is noteworthy that only inter-session but not intra-session repeatability was considered in the analysis, to reflect most studies that investigate choroidal metrics in an inter-session rather than intra-session (consecutive) manner.

4.4   Results

4.4.1   Wide-field topography of ChT and CVI

Presented ChT and CVI were sorted by retinal location and eccentricity, as presented in Table 4. In general, the ChT decreased with increasing eccentricity and was typically highest superiorly, followed by the temporal, inferior, and nasal areas. In contrast, CVI showed a relatively uniform pattern with almost no eccentricity- or region-dependent fluctuations. Quartile-based CV across the scanned retina were 5.92 for ChT and 0.89 for CVI. There were no significant correlations found between ChT and CVI in any ETDRS sector (all $P > 0.05$). However, there appears to be a general transition from negative to increasingly positive correlations between the parameters with increasing eccentricity.

Figure 12 shows an example of the CVI algorithm output with typical topographic variations for ChT and CVI. As depicted in Figure 12b and Figure 12c, the structures of larger choroidal vessels are highly visible with a subsequently higher CVI. This relationship is not surprising, since these pixel columns will comprise predominantly vessel lumina, yielding a high CVI in these localized areas.
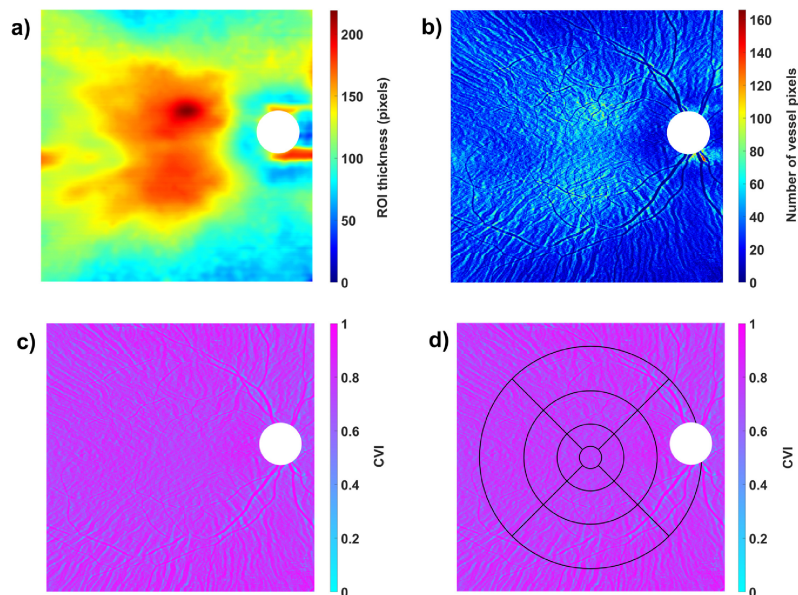
Figure 12: Output of the CVI algorithm for an example participant: (a) ChT segmentation as ROI; (b) Calculated number of vessel pixels; (c) CVI map without ETDRS grid and (d) CVI map with overlaying ETDRS grid, adjusted for image magnification. The white area of the ONH was excluded from analysis.

| | ChT (µm) | | CVI (%) | | Correlation ChT × CVI | |
	Median	IQR	Median	IQR	ρ	P-value
Central field						
Central	323.24	29.30	72.89	4.51	-0.39	0.17
Inner fields						
Superior	333.98	54.69	74.20	4.12	-0.06	0.84
Inferior	299.80	64.45	74.12	4.58	-0.38	0.18
Temporal	315.43	48.83	75.11	3.75	-0.14	0.64
Nasal	298.82	54.69	73.78	4.61	-0.24	0.41
Outer fields						
Superior	329.10	64.45	73.80	4.49	+0.30	0.30
Inferior	303.71	111.33	74.15	4.14	-0.17	0.57
Temporal	297.85	50.78	76.05	5.65	+0.12	0.69
Nasal	246.09	78.12	76.08	5.35	-0.07	0.82
Extended fields						
Superior	344.72	70.31	73.35	3.72	+0.25	0.38
Inferior	285.15	64.45	73.49	3.95	+0.28	0.33
Temporal	287.11	46.87	75.34	6.01	+0.46	0.10
Nasal	200.19	60.55	74.72	5.44	+0.38	0.19

Table 4: Topographical distribution of ChT and CVI across the scan area and their correlation with each other.

4.4.2 Relationship between axial length and choroidal metrics

The relationship of both choroidal parameters with AEL was investigated to explore the potential effects of eye size on ChT and CVI. While ChT decreased with increasing AEL in all scan fields, CVI showed a more variable relationship with AEL (Table 5). The central and inner fields correlated positively with AEL, whereas negative correlations were found in the most peripheral regions. Despite the consistency in the pattern of ChT, the relationship with AEL was statistically significant only in the inner superior field (P = 0.02), and there were no significant correlations between CVI and AEL.

4.4.3 Inter-session repeatability

The CR between the three measurement sessions for choroidal metrics is reported in Table 6. There were small regional fluctuations for ChT, ranging from 10.37 µm (inner temporal and extended inferior fields) to 20.33 µm (extended nasal field). CVI repeatability ranged between 3.90% in the outer inferior field and 5.51% in the temporal extended field. The quartile-based CV for the repeatability across the total scan area were 11.11 and 9.66 for ChT and CVI respectively.

	ChT × AEL		CVI × AEL	
	ρ	P-value	ρ	P-value
Central field				
Central	-0.49	0.08	+0.45	0.10
Inner fields				
Superior	*-0.61*	*0.02*	+0.16	0.57
Inferior	-0.25	0.38	+0.34	0.24
Temporal	-0.48	0.08	+0.21	0.47
Nasal	-0.45	0.11	+0.46	0.10
Outer fields				
Superior	-0.37	0.19	-0.24	0.42
Inferior	-0.21	0.47	+0.24	0.42
Temporal	-0.40	0.15	-0.05	0.86
Nasal	-0.47	0.09	+0.22	0.44
Extended fields				
Superior	-0.13	0.65	-0.34	0.24
Inferior	-0.05	0.87	-0.06	0.83
Temporal	-0.32	0.26	-0.27	0.35
Nasal	-0.50	0.07	-0.14	0.63

Table 5: Spearman correlation coefficient (ρ) and associated P-value of choroidal metrics with axial eye length. Significant correlations are highlighted in *italics*.

The last two columns of Table 6 represent the relative proportion between the repeatability coefficient and the absolute median values from Table 4. With exception of the nasal extended subfield, ChT exhibits a relatively better repeatability than CVI.

4.5   Discussion

The study undertaken investigated the wide-field distribution of ChT and CVI, their inter-session repeatability and their relationship to axial eye length. Moreover, novel and advantageous methodology was applied as follows:

(1) Swept-source OCT with an increased wide-field scan area of 12 x 12 mm was used. A smaller region of interest with a diameter of 10 mm was evaluated due to potential information loss resulting from magnification correction using AEL. To our knowledge, this is the largest evaluated retinal area for CVI distribution, ChT and CVI repeatability, and axial length scaling correlation to date.

	CR		CR / Median	
	ChT (µm)	CVI (%)	ChT (%)	CVI (%)
Central field				
Central	11.96	4.00	3.70	5.49
Inner fields				
Superior	16.35	4.20	4.89	5.65
Inferior	13.95	4.21	4.65	5.67
Temporal	10.37	4.54	3.29	6.05
Nasal	10.76	4.15	3.60	5.62
Outer fields				
Superior	13.95	3.93	4.24	5.33
Inferior	12.76	3.90	4.20	5.26
Temporal	11.36	5.41	3.81	7.11
Nasal	11.56	4.88	4.70	6.41
Extended fields				
Superior	11.16	5.00	3.24	6.81
Inferior	10.37	4.39	3.64	5.97
Temporal	11.16	5.51	3.89	7.32
Nasal	20.33	4.02	10.16	5.38

Table 6: CR for ChT and CVI across the ETDRS sectors. The last two columns denote the proportion in percentage between the CoR to the median value reported in Table 4.

(2) The analysis of three-dimensional volume scans was possible thanks to enhanced scan depth and thus improved image quality compared to spectral-domain OCT. Previously, most CVI and ChT metrics were obtained from line scans or as single measurement points only.

(3) All algorithms used were optimized to run entirely automated (with the exception of the semi-automated exclusion of the optic nerve head) on all 1024 B-scans per volume. This includes image-processing steps for choroidal thickness and choroidal vascularity analysis, as well as the subsequent scaling of the ETDRS grid to account for image magnification. This approach reduces analysis time, examiner bias, and inter-observer variation.

(4) The size of the ETDRS sectors was compensated for image magnification for each participant, from their AEL measurement. Moreover, the study measurements were controlled for choroidal diurnal rhythm by performing the measurements always at the same time of day for each participant. Eye movement artifacts during and between scans were minimized by using the inbuilt eye-tracking and follow-up mode of the device.

4.5.1 CVI reveals less topographical variations than ChT

ChT showed a higher variability of topographical distribution across the retina compared to CVI. ChT generally decreased toward the periphery (particularly in the nasal sector), as reported previously [Mohler et al., 2015; Hoseini-Yazdi et al., 2019c; Breher et al., 2018; Rasheed et al., 2018]. CVI distribution patterns were more uniform with no obvious influence of retinal location and thus lower variability metrics. Regional consistency is also reflected in the low quartile-based CV of 0.89 for CVI, compared to 5.92 for ChT. This is consistent with earlier studies [Agrawal et al., 2016b; Goud et al., 2019], although these found generally lower absolute CVI values of around 45% to 65% [Agrawal et al., 2016b; Goud et al., 2019; Li et al., 2020; Singh et al., 2018]. These differences likely arise from the use of different OCT devices, scan patterns, image-processing algorithms, and participant age and ethnicity distributions. However, it has been stated that central CVI (measured in two dimensions) is not significantly influenced by the choice of scan pattern [Agrawal et al., 2017] or OCT device [Agrawal et al., 2019]. Moreover, ChT and CVI showed a tendency of eccentricity-dependent association with each other, with a shift from negative to positive correlations toward the peripheral retinal. This suggests that the thicker central and inner choroid result from a higher stromal rather than vascular component. This is in contrast to previously reported positive correlations of ChT and CVI in the central retina up to 1.5mm diameter [Agrawal et al., 2016b], which is comparable to the central and inner fields defined in the current study.

4.5.2 Eccentricity-dependent correlations of AEL with CVI

When establishing and adjusting normative databases, the interactions of choroidal metrics with AEL are an important factor to be considered. Like this, it is possible to differentiate physiologic from truly pathologic deviations. ChT is known to thin with increasing AEL [Agrawal et al., 2016b; Hirata et al., 2011; Sanchez-Cano et al., 2014; Jin et al., 2016]. The lack of statistical significance in the current study, except in the inner superior field, most likely arises from the relatively small sample size. CVI again exhibits mixed associations with AEL; centrally, longer ocular length leads to an increased vascular component and/or reduced stromal component. In contrast, higher AEL comes along with lower CVI in the peripheral retina. Interestingly, this eccentricity-dependent correlation pattern is the inverse of the ChT and CVI correlation described above.

Previous correlation findings appear somewhat inconclusive; low negative correlations of CVI with AEL have been reported [Agrawal et al., 2016b; Li et al., 2020; Goud et al., 2019], while slightly increased vascular components with myopia have also been observed [Gupta et al., 2017; Alshareef et al., 2017a]. However, these findings are all limited to the central or maximally the outer scan fields and do not all reach statistical significance.

4.5.3 Repeatability of choroidal metrics is similar to reported effect sizes

The analysis of inter-session repeatability was included for two reasons: first, to evaluate whether there are more metrologically preferred retinal areas for measurements in future studies. These are areas that exhibit lower CR values. Second, the repeatability of these choroidal metrics is put into context of commonly found effect sizes. To address the first question, the nasal extended area manifests the highest CR with $20.33\,\mu m$ compared to the other ETDRS sectors (10.37 - $16.35\,\mu m$). One earlier publication reported an averaged CR of $30\,\mu m$ for ChT with automated segmentation in swept-source volume scans but without differentiating between ETDRS areas [Mansouri et al., 2014]. Moreover, another methodologically similar study found the opposite for spectral-domain OCT scans, with the best repeatability in the nasal sectors due to thinner choroids and thus advantageous imaging properties [Breher et al., 2019b]. However, comparisons to other past literature are limited, since the range of methodologies used and analyzes reported are broad. In contrast to ChT, repeatability of CVI measurements did not show any regional variations, surprisingly even in the extended nasal subfield. Therefore, CVI can be measured irrespective of the retinal region from a metrologic perspective. There are few published reports on the repeatability of CVI measurements and all limited to spectral-domain and line scan analysis, making comparisons to the present study difficult. Moreover, these commonly evaluate the repeatability of luminal and stromal areas separately, which causes difficulties when translating it to repeatability results of final and summarized CVI measurements. However, the somewhat most comparable study found 95% limits of agreements ranging from approximately -4% to +3% [Agrawal et al., 2017]. From a relative perspective, however, ChT exhibits a better repeatability compared to the absolute thickness than CVI (Table 6). This finding is in line with another study in healthy participants [Agrawal et al., 2016b]. There has not been a definite theory for this relation yet. However, one hypothesis suggests that the repeatability of CVI is dependent on the repeatability of ChT, as a first and inherent processing step. Therefore, this finding can be expected.

The second step was to compare reported effect sizes with measurement variability. Only if the CR does not exceed the effect size can measurement noise be neglected as a source of error. Typical reported differences between healthy and disease conditions are around 2% to 6% for CVI (review: Agrawal et al. (2020) [Agrawal et al., 2020]). For ChT, the effect size is highly dependent on the condition studied. In retinal disease, ChT alterations of around $100\,\mu$m are commonly found [Maruko et al., 2010, 2011; Chung et al., 2011]. However, in myopia research, the measurement reliability is similar to or even exceeds published effect sizes of maximally $20\,\mu$m (review: Read et al. (2019) [Read et al., 2019b]), even when using swept-source OCT technology with improved choroidal imaging. In summary, measurement repeatability should be carefully considered when interpreting "true" change or difference in both choroidal parameters and distinguishing from measurement variation.

4.5.4 Limitations

A relatively small sample size of $n = 14$ was used for this study. Although axial length was normally distributed and covered the range of usual emmetropic and myopic ocular sizes in the normal population, the small sample size could affect the homogeneity of the sample. It is therefore prudent to view the correlation results as indicative rather than definitive, and these relationships warrant further investigation with a larger sample with a wider range of axial lengths and stronger homogeneity. All included participants were young adults without ocular pathology and from Caucasian descent (except for one Indian participant). Therefore, the findings should be applied cautiously to other age groups and ethnicities, as well as in pathology. Moreover, participants could not be fully controlled for all factors shown to affect the choroid, such as smoking and caffeine. By enrollment into the study, participants were advised to avoid caffeine and nicotine intake at least for 1 hour before the measurements but this could not be verified by the examiner. Blood pressure as another confounding factor was not measured specifically, as it was assumed to be stable within one individual because of the 10-minute resting and distance viewing period prior to the measurements. Despite imaging advances with swept-source and long-wavelength OCT, there were still B-scans in the evaluated subset with limited visibility of either the choroidal-scleral interface or vessels. The limited contrast of choroidal structures occurred due to OCT signal roll-off with increasing scan depth and therefore measurement noise. Retinal vessel shadows (areas of hyporeflectivity in the choroid from overlying structures) represent another measurement artifact and could lead to a misjudgement of CVI. However, these artifacts are limited to the extended nasal, inferior, and superior analysis regions. While this factor might have a small influence on CVI in those regions, it should not affect the repeatability results, as the retinal vessels are not transient.

Therefore, these artifacts were acknowledged in these three out of 13 analysis regions but were not removed from the images due to their expected limited effect on the outcomes. The results of the extended nasal sector might have been additionally influenced by the semi-automated exclusion of the optic nerve head, leading to a reduced number of analyzed pixels in that region, which varied between participants based on the size of that feature. Despite the image size compensation for magnification, caused by axial length differences of the participants, they were not corrected for ocular curvature. Subsequently, this might lead to small biases in measurements of absolute ChT, especially in the periphery of the scan and with increasing curvature. However, the magnitude of error usually tends to be relatively small with up to 6.0 μm at a scan eccentricity of almost 7 mm [Kuo et al., 2013]. Moreover, no highly myopic eyes were included into the study and only affects the absolute measures of ChT but not the repeatability measurements, as these were analyzed in a relative manner to each other. Therefore, the total error in the current study is existent but most probably has only very limited effect on the final outcomes and conclusion.

4.6 Conclusions

This study provides evidence that choroidal vascularity does not follow a clear and distinct topographical pattern across the central retina, unlike ChT. Moreover, mixed correlations between ChT and CVI, as well as CVI and axial length, were found, whereas choroidal thinning with increasing axial length was confirmed. It was further observed that the repeatability of CVI measurements does not vary across scan areas, in contrast to ChT measurements. However, the repeatability of both metrics is similar to or even exceeds previously reported effect sizes in many studies using choroidal parameters. Measurement repeatability should be considered in the interpretation of results from studies involving the choroid as a biomarker.

5 Wide-field retinal and foveal shape in myopia and emmetropia

5.1 Abstract

Myopic axial eye growth has mechanical implications on ocular structures, such as the retinal and foveal shape integrity or choroidal thickness. The current study investigated myopia-related changes of retinal radius of curvature, foveal width, depth, slope and choroidal thickness. Wide-field swept-source OCT line and volume scans were performed on 40 young adult participants in horizontal and vertical directions. OCT scans were corrected for their scan display distortions before automated extraction of retinal and foveal shape parameters. All findings were correlated to refractive error and axial length. The horizontal retinal radius of curvature and the directional ratio between horizontal and vertical retinal shape correlated significantly with axial length ($\rho = +0.53$, $p < 0.001$ and $\rho = +0.35$, $p < 0.05$). Vertical retinal shape and foveal pit parameters neither showed any significant correlations with axial length nor refractive error (all $p > 0.05$). Choroidal thickness correlated significantly with refractive error in all analyzed regions (ρ +0.39 to +0.52), but less with axial length (ρ -0.18 to -0.37). Horizontal retinal shape and choroidal thickness, but not foveal pit morphology, were altered by myopic eye growth. Asymmetries in horizontal vs. vertical retinal shape with increasing myopia were detected. These parameters could act as promising biomarkers for myopia and its associated complications.

5.2 Introduction

Myopia is a worldwide problem with rising prevalence, affecting half of the population in 2050 [Holden et al., 2016]. Myopia is caused by a mismatch between the ocular focal length and axial length due to excessive eye growth [Meng et al., 2011]. An increased myopic refractive error thus reflects a longer axial length, which leads to growth-induced retinal changes due to mechanical stretching of the tissue. Therefore, it appears logical that myopia also increases the risk especially for retinal pathologies, such as myopic maculopathy and retinal detachment [Saw et al., 2005; Flitcroft, 2012].

There is a dose-response relationship, which indicates a proportional relationship between amplitude of the refractive error and the risk to be affect by a particular complication. Myopes with a refractive error of -3D, -6D and -9D have a threefold, nine-fold and 22-fold higher odds ratio to suffer from retinal detachment, respectively [Flitcroft, 2012; Ogawa and Tanaka, 1988]. Furthermore, macular degeneration occurs up to 350 times more often in myopes [Flitcroft, 2012; Vongphanit et al., 2002]. As these diseases commonly lead to a potentially irreversible loss of sight, but also will affect an increasing part of the worldwide population, one aim in myopia research is to identify biomarkers for myopia. Ideally, these biomarkers should describe myopic eye growth and associated risks, while being obtained by clinically feasible measurement procedures. Since the retina is one of the most affected tissues during eye growth, the investigation of retinal shape and layer thickness has become a subject of interest in myopia research.

Retinal shape can be measured either directly using magnetic resonance imaging (MRI) [Atchison et al., 2005], but also indirectly via peripheral biometry [Schmid, 2003, 2011; Verkicharla et al., 2015, 2016] or peripheral refraction [Atchison, 2012; Tabernero and Schaeffel, 2009b; Tabernero et al., 2011]. The retinal shape can then be inferred from the differences between eccentric and central refraction or axial length. However, indirect conclusions from eccentric eye length or peripheral refraction should only be made cautiously. Optical aberrations occur in off-axis measurement angles, which are caused by eye, instrument or head rotations, and which cannot be predicted and thus considered in the individual subjects [Verkicharla et al., 2012; Koumbo et al., 2019; Atchison and Charman, 2011]. Therefore, indirect measurement techniques suffer from a certain inaccuracy, while recent direct procedures, such as MRI, are of reduced clinical feasibility and too cost-intensive. Due to these limitations, optical coherence tomography (OCT) as established tool for in-vivo retinal imaging was taken into account for the analysis of retinal shape. However, original OCT scan images appear flattened due to displaying reasons. These displaying distortions can be corrected through optical re-modelling [Steidle and Straub, 2018; Kuo et al., 2013, 2016; Minami et al., 2020]. Consequently, the retinal shape can be extracted from these distortion-corrected OCT scan images.

Additionally, foveal pit morphology - such as width, depth and slope - can be analyzed via OCT imaging either with original [Nolan et al., 2008; Dubis et al., 2009; Wagner-Schuman et al., 2011; Ding et al., 2014; Liu et al., 2016; Scheibe et al., 2016; Tick et al., 2011] or corrected scans [Breher et al., 2019a].

Choroidal thickness presents another potentially important biomarker for myopia. Multiple studies investigated the choroid in relation to refractive error and axial length. They used a broad variety of methodological tools regarding OCT technology (spectral-domain vs. swept-source OCT), segmentation method (manual vs. automated) and evaluated locations (single point locations vs. broader areas). The majority finds decreasing choroidal thickness with increasing myopia [Ikuno et al., 2010; Agawa et al., 2011; Li et al., 2011; Hirata et al., 2011; Sanchez-Cano et al., 2014; Jin et al., 2016].

In summary, it is of high interest to determine if and which ocular parameters - additionally to axial length and refractive error - could be used to describe and evaluate myopic eye growth. So far, retinal shape has been measured mostly via eccentric biometry, refraction or MRI with the known limitations. Additionally, retinal shape was investigated using corrected spectral-domain OCT scans but with a relatively small scan field. The relation of foveal pit shape to refractive error has not been investigated yet with distortion-corrected scans. In contrast, the purpose of previous studies was choroidal thickness and correlations to axial length or refractive error. However, these groups used spectral-domain OCT with associated reduced visibility of the choroid, manual and potentially biased segmentation methods or smaller scan fields.

The current study was thus focused to identify whether distortion-corrected retinal shape, foveal pit morphology, as well as choroidal thickness exhibit correlations with axial length or refractive error. If this is the case, these parameters could figure as appropriate biomarkers for myopia, measurable in a clinically feasible setting using OCT and biometry.

5.3 Results

5.3.1 Normative values

Table 7 shows an overview about the averages and distribution of the analyzed parameters in all scan directions (retinal and foveal morphology) and sectors (choroidal thickness). Data are presented as median and interquartile range (IQR). In total, the horizontal retinal radius of curvature is smaller than the vertical, leading to a horizontal-to-vertical ratio of < 1.00 between both meridians. The same proportion can be found for foveal depth and slope, where the vertical values exceed the horizontal values and a subsequent ratio of < 1.00. Foveal width presents an exception, as the horizontal width is larger than the vertical width, resulting in an average directional relation of > 1.00. Choroidal thickness is generally thicker in the central than peripheral retina. Moreover, regional differences can be detected, with thicker choroids in the superior and temporal areas compared to inferior and nasal areas.

	Median $\pm$ IQR (mm / °)		Median $\pm$ IQR (µm)
RRC H	13.20 ± 1.80	**ChT #1**	379 ± 119
RRC V	13.32 ± 2.63	**ChT #2**	381 ± 144
RRC H/V	0.98 ± 0.11	**ChT #3**	367 ± 127
Foveal width H	1.21 ± 0.25	**ChT #4**	382 ± 122
Foveal width V	1.16 ± 0.25	**ChT #5**	349 ± 143
Foveal width H/V	1.08 ± 0.10	**ChT #6**	363 ± 131
Foveal depth H	0.11 ± 0.03	**ChT #7**	351 ± 128
Foveal depth V	0.12 ± 0.03	**ChT #8**	357 ± 104
Foveal depth H/V	0.94 ± 0.11	**ChT #9**	281 ± 126
Foveal slope H	14.00 ± 3.97	**ChT #10**	340 ± 98
Foveal slope V	16.54 ± 3.51	**ChT #11**	290 ± 88
Foveal slope H/V	0.89 ± 0.11	**ChT #12**	313 ± 66
		ChT #13	213 ± 82

Table 7: Median and IQR values for the investigated paramters. Abbreviations: RRC = retinal radius of curvature; H = horizontal scan meridian; V = vertical scan meridian; ChT #n = choroidal thickness in specific ETDRS area.

5.3.2 Correlations to axial length and refractive error

However, the IQR indicates high inter-subject variability in all investigated parameters, which could be based on a dependency of the retinal parameters on axial length or refractive error. Therefore, the retinal and foveal morphology, and choroidal thickness were correlated to axial length and refractive error as a next step, as seen in Table 8 and Figure 13. Choroidal thickness correlated more often and more significantly with refractive error than axial length. Retinal shape showed significant positive correlations in the horizontal direction ($\rho = +0.53$, $p < 0.001$) and in the directional ratio ($\rho = +0.35$, $p < 0.05$) with axial length, but not in the vertical scan meridian. Foveal width, depth and slope could be associated with neither axial length nor refractive error in any scan direction. Moreover, axial length and refractive error were correlated negatively with each other ($\rho = -0.71$, $p < 0.001$).

5.4 Discussion

The current study investigated the influence of myopia - characterized by axial length and spherical refractive error - on retinal shape, foveal pit morphology and choroidal thickness in young adults. In-vivo retinal imaging was performed using wide-field swept-source OCT with distortion-correction of the arrangement of the OCT scan [Steidle and Straub, 2018]. The findings can be summarized and interpreted as follows:
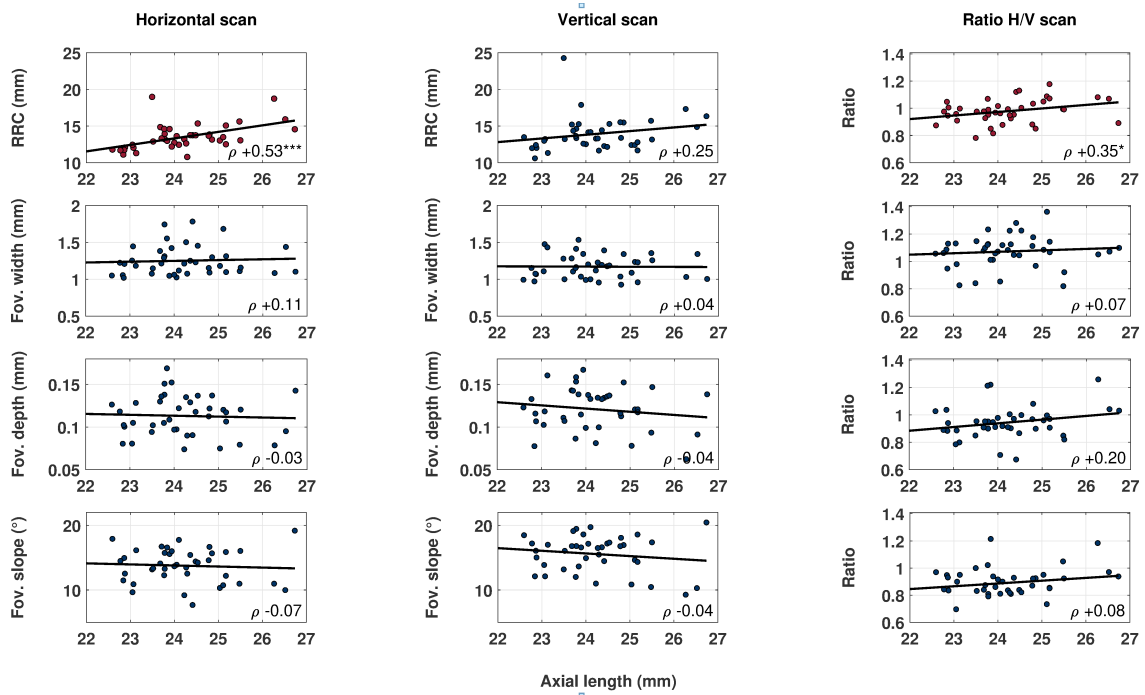
Figure 13: Correlations of axial length with retinal and foveal shape parameters in horizontal and vertical scan meridians, as well as their H/V ratio. For a fast overview, significant correlations with axial length - as in the case with horizontal retinal radius of curvature (RRC), as well as horizontal-to-vertical ratio - are plotted with red markers Asterisks behind the Spearman ρ value denote significant correlations of the retinal parameters with axial length, with *$p < 0.05$, **$p < 0.01$, ***$p < 0.001$.

All retinal radii fall within commonly reported previous results of 8mm-21 mm [Kuo et al., 2013, 2016] and averages between 11 mm and 14 mm [Atchison and Smith, 2000]. The horizontal retinal radius, as well as the horizontal-to-vertical ratio of radii, revealed significant positive correlations with axial length. Myopes tend to have slightly larger radii and directional ratios than emmetropes. These findings go along with a recent OCT study with a similar methodology [Minami et al., 2020]. This means, that the common relationship of larger vertical than horizontal radii is not maintained after myopic eye growth. The same directional disparity was also reported for ocular shape in MRI scans [Atchison et al., 2004; Verkicharla et al., 2012]. Therefore, ocular and retinal shape both change differently in the horizontal and vertical direction. This asymmetrical and changed growth pattern could be also related to a more irregular retinal pigment epithelium (RPE) surface in myopes [Lake et al., 2019] and an altered fundus curvature with myopic complications, such as myopic choroidal neovascularization, chorio-retinal atrophy and staphyloma [Miyake et al., 2014].

	Axial length	Refractive error		Axial length	Refractive error
RRC H	+0.53***	-0.16	ChT #1	-0.27	+0.44**
RRC V	+0.25	-0.01	ChT #2	-0.35*	+0.51***
RRC H/V	+0.35*	-0.27	ChT #3	-0.29	+0.41**
Fov. width H	+0.11	-0.09	ChT #4	-0.29	+0.49**
Fov. width V	+0.04	+0.13	ChT #5	-0.32*	+0.45**
Fov. width H/V	+0.07	-0.14	ChT #6	-0.27	+0.46**
Fov. depth H	-0.03	+0.10	ChT #7	-0.28	+0.43**
Fov. depth V	-0.04	+0.15	ChT #8	-0.37*	+0.52***
Fov. depth H/V	+0.20	-0.19	ChT #9	-0.36*	+0.46**
Fov. slope H	-0.07	+0.15	ChT #10	-0.18	+0.46**
Fov. slope V	-0.04	+0.07	ChT #11	-0.20	+0.42**
Fov. slope H/V	+0.08	+0.05	ChT #12	-0.19	+0.46**
			ChT #13	-0.28	+0.39*

Table 8: Spearman correlation coefficient ρ of horizontal and vertical retinal radius of curvature, foveal pit morphology, choroidal thickness and the ratios of horizontal and vertical parameters, with axial length and refractive error, respectively. Asterisks behind the Spearman ρ value denote significant correlations of the retinal parameters with axial length or refractive error, with *$p < 0.05$, **$p < 0.01$, ***$p < 0.001$. Abbreviations: RRC = retinal radius of curvature; H = horizontal scan meridian; V = vertical scan meridian; ChT #n = choroidal thickness in specific ETDRS area.

Regarding foveal pit morphology, myopes tend to have smaller foveal widths, depths and shallower slopes. However, no statistically significant differences and correlations were shown. This finding is in concordance with an earlier study that indirectly concluded foveal pit shape from uncorrected retinal thickness maps [Dubis et al., 2009].

Choroidal thickness is generally known to thin with increasing retinal eccentricity, axial length and myopic refractive error, which could be replicated in the current study. Spearman analysis revealed correlation coefficients between +0.39 and +0.52 for refractive error, and -0.18 and -0.37 for axial length, which is generally in accordance with past studies [Ikuno et al., 2010; Agawa et al., 2011; Li et al., 2011; Hirata et al., 2011; Sanchez-Cano et al., 2014; Jin et al., 2016]. However, it seems noteworthy that choroidal thickness correlated more with refractive error than axial length, which was an unexpected finding, as it is commonly described vice versa [Ikuno et al., 2010; Li et al., 2011; Sanchez-Cano et al., 2014; Jin et al., 2016]. This difference might be caused by the choice of using the spherical refractive error instead of the spherical equivalent refractive error for the correlations. This way of analysis rules out the influence of astigmatism on correlation results, as astigmatism otherwise would artificially increase the myopic refractive error.

Moreover, the choroidal thinning seems to be more attenuated in the central than in the peripheral retina, as well as superiorly more than nasally, as already described earlier [Read et al., 2013; Hoseini-Yazdi et al., 2019c]. Possible relations of these spatial characteristics with different regional choroidal thickness changes in response to defocus [Breher et al., 2018; Chen et al., 2016; Hoseini-Yazdi et al., 2019a] need further investigation.

The current study also faces some potential limitations. Firstly, the amount of participants was relatively small, as it was carried out as a pilot-study. Secondly, the majority of the dataset consisted of emmetropic and low to moderate myopic participants, lacking high myopes ($< $-6 D). In high myopia, more obvious myopia-related changes might have been detected. This could have also been the case if bigger scan angles were used. Although the scan field can be enlarged via add-on lenses or image stitching, this measurement procedure cannot be translated into a feasible clinical setting with patients so far. Moreover, the optical correction model cannot (yet) account for the unpredictable high optical off-axis measurement phenomena, resulting in eventually large inaccuracies in distortion-correction. The used swept-source OCT device provides a maximum of 16 mm line scans and 12x12 mm^2, which is approximately double the scan size as in commonly used spectral-domain OCTs. Furthermore, swept-source technology enables a faster scanning procedure with more A-scans and B-scans. The relation of scan time and gain of information becomes of importance when examining patients with reduced fixation ability, due to young age or ocular diseases, as it appears with myopia. In addition, the relatively large scan angle, high resolution and scan depth provide easily visible extra-macular imaging in deep retinal structures. This information is not only needed for the evaluation of retinal shape and choroidal thickness, but also clinical exams for peripheral and choroidal complications in myopia [Flitcroft, 2012; Saw et al., 2005].

Regarding retinal shape calculations, spherical fits were chosen over ellipsoid fits [Atchison et al., 2005; Atchison and Charman, 2011; Verkicharla et al., 2016; Kuo et al., 2016] or cubic spline functions [Minami et al., 2020]. This approach was based on two main points: Firstly, a spherical fit does not produce higher fitting errors up to a scan size of 16 mm, as shown with an example OCT scan in Figure 14. Therefore, it is adequate and accurate compared to more complex models. Secondly, the retinal radius of curvature represents a single and conclusive parameter for the numerical description of retinal shape. Providing short and informative values becomes of high importance when translating and applying research methods and findings into clinical settings.
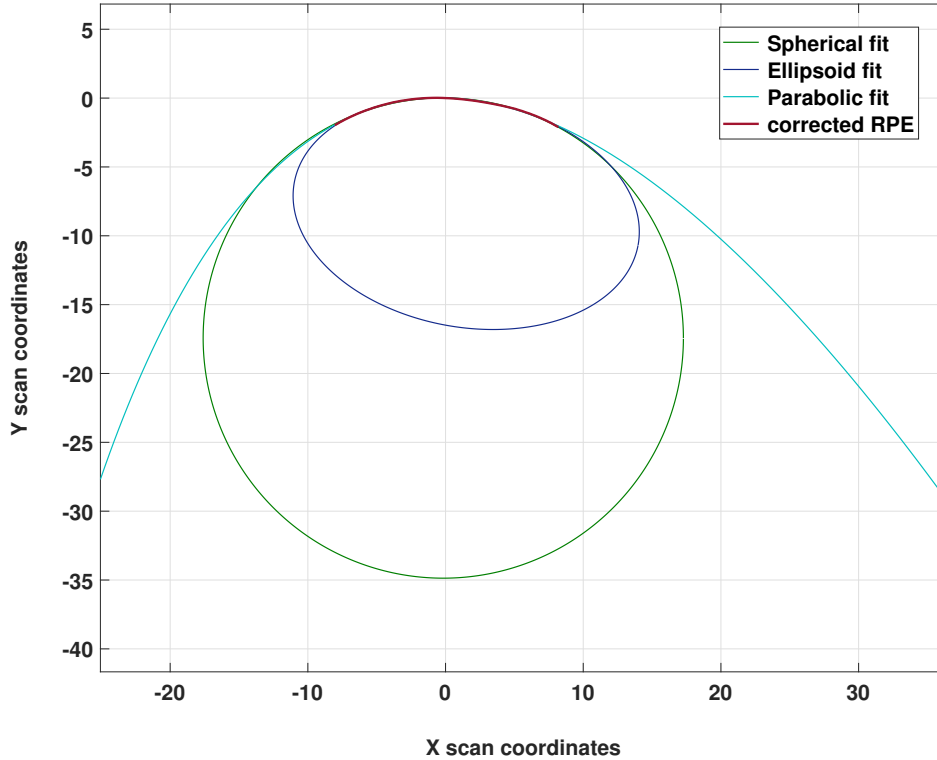
Figure 14: Comparison of different mathematical models to fit the distortion-corrected RPE. Spherical, ellipsoid and parabolic shapes were fitted to the distortion-corrected retina of the 16 mm line scan. Up to the current scan size, none of the models shows a superior fit than the others.

Furthermore, only line scans were corrected for scan image distortions but not volume scans - from which the choroidal thickness maps were extracted. The distortion-correction of whole cube scans is very time- and memory-extensive with current software and hardware. Also, previous studies showed that absolute errors in uncorrected vs. corrected volume scans are in the range of $2.5\,\mu m$ and $6.7\,\mu m$ in the center and in the periphery of the scan field, respectively [Kuo et al., 2013]. Moreover, some peripheral and potentially erroneous choroidal thickness values were not considered in the data analysis, due to the division into Early Treatment of Diabetic Retinopathy Study (ETDRS) [Early Treatment Diabetic Retinopathy Study Research Group, 1985] areas. This additional step of distortion-correction was thus skipped, while still maintaining high accuracy.

To conclude, the study provided evidence that changes in choroidal thickness, horizontal retinal radius of curvature and the horizontal-vertical growth ratio exhibit significant correlations to axial length and/or refractive error. Therefore, retinal shape and choroidal thickness, but not foveal pit morphology, are altered by myopia-induced eye growth.

Subsequently, these parameters are able to indicate retinal changes caused by eye growth, thus, could figure as promising biomarkers for myopia and associated complications. Moreover, the study provides a fast and feasible measurement procedure and thus an easy translation into clinical practice by using commonly available technology. Longitudinal studies are needed to evaluate the ongoing growth process of retinal, foveal and choroidal parameters in children but also in highly myopic participants with and without myopia-related ocular pathologies.

5.5 Methods

5.5.1 Study participants

This prospective study was carried out at the Institute for Ophthalmic Research at the University Tuebingen, followed the Declaration of Helsinki and data protection regulations and was approved by the ethics committee of the Faculty of Medicine of the University Tuebingen. Written informed consent was obtained from every study participant prior to the measurements. Participants with ocular pathologies, surgeries, hyperopia or insufficient OCT signal strength < 6 were excluded. In total, 40 young adults (12 males and 28 females) with a mean age of 24.5 ± 3.5 years were included in the study. Mean refractive error and axial lengths were $-1.33 \pm 1.83 \, \text{D}$ (range $+0.60 \, \text{D}$ to $-5.33 \, \text{D}$) and $24.22 \pm 1.02 \, \text{mm}$ (range $22.59 \, \text{mm}$ to $26.74 \, \text{mm}$), respectively.

5.5.2 Instrumentation and measurement procedure

Each participant underwent objective refraction using wavefront aberrometry (ZEISS i.Profiler plus, Carl Zeiss Vision GmbH, Aalen, Germany), ocular biometry (ZEISS IOLMaster 700, Carl Zeiss Meditec AG, Jena, Germany), as well as retinal imaging using swept-source OCT (ZEISS PlexElite 9000, Carl Zeiss Meditec Inc., Dublin, CA, USA). The swept-source OCT system uses a wavelength between 1040nm and 1060nm and therefore reaches a scan depth of $3 \, \text{mm}$ with an axial resolution of $6.3 \, \mu\text{m}$ in tissue. The OCT scan included different scan patterns: a $12 \text{x} 12 \, \text{mm}^2$ macular volume scan consisting of 1024 B-scans with 1024 A-scans per B-scan, as well as a horizontal $0°$ and nearly vertical $80°$ $16 \, \text{mm}$ line scan centered on the fovea. The scan meridian of $80°$ instead of exactly $90°$ was chosen due to technical limitations in the size of the vertical scan field of the OCT device. The overall OCT field of view is rectangular instead of squared, being larger in the horizontal than vertical dimension. Therefore, a $16 \, \text{mm}$ line scan would exceed the vertical dimensions of the scan field if oriented $90°$, in contrast to an $80°$ directional scan.

5.5.3 Distortion correction and extraction of retinal morphology parameters

OCT distortion correction

Prior to the calculation of the retinal shape and foveal pit morphology, the OCT line scans were corrected for the display distortions as previously validated [Steidle and Straub, 2018]. Briefly, this approach ray-traces the single A-scan pathways of one B-scan through the optics of the OCT device and ocular surfaces (OpticStudio, Zemax, LLC, Kirkland, WA, USA), resulting in a line of constant group delay for all the A-scans of this particular B-scan. Based on the position and displacement of the line of constant group delay, the scan image is accordingly re-arranged and corrected for the dimensional distortions. Individual eye and scan parameters can be modified in the computer model, e.g. the participants' individual axial lengths, as done in the current study. An example OCT scan before and after distortion correction is illustrated in Figure 15.
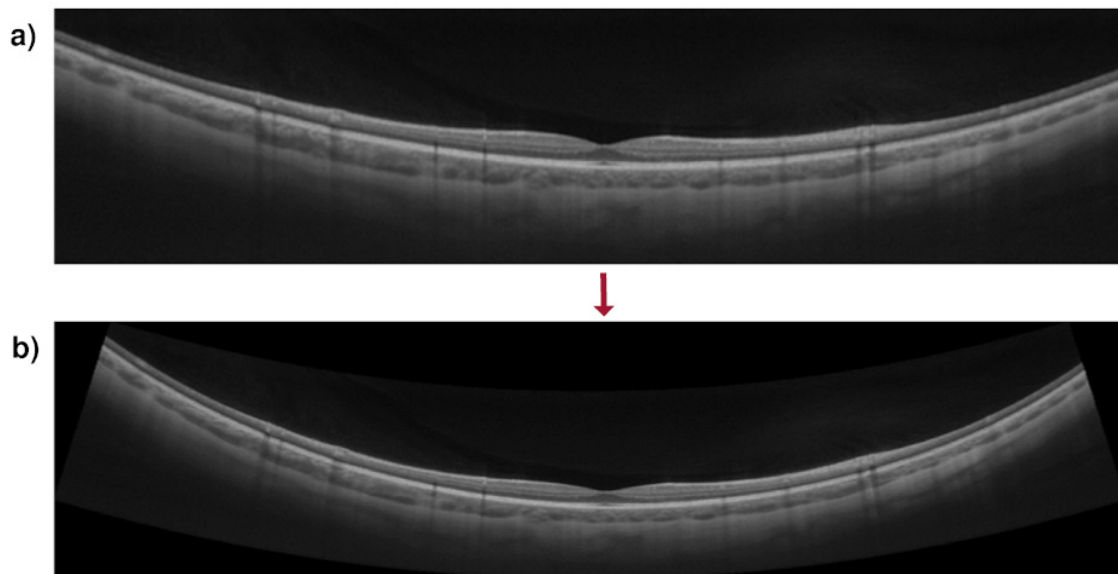

Figure 15: a) Uncorrected, "original" OCT B-Scan of 16 mm length in 80° scan orientation. b) Output B-scan after distortion-correction. Note the increased curvature compared to the artificially flattened, original scan image in a).

Retinal radius of curvature

After distortion correction, the retinal radius of curvature was determined by fitting a sphere to the distortion-corrected RPE of the B-scans [Steidle and Straub, 2018].

Foveal pit morphology

Foveal pit parameters were extracted using a previously validated and semi-automated approach [Breher et al., 2019a]. Foveal width, depth and slope were obtained from defined mathematical landmarks of a Sum of Gaussian fit to the foveal surface of the distortion-corrected scan image.

Choroidal thickness

Choroidal thickness was defined as the distance from the RPE to the chorio-scleral interface. Thickness maps were obtained from automated image segmentation via the Advanced Retinal Imaging Network (ARI Network, Carl Zeiss Meditec Inc., Dublin, CA, USA). The ARI Network represents a research portal provided by Carl Zeiss Meditec Inc., which offers various algorithms for researchers using the PlexElite 9000 OCT device. Thickness data from the optic nerve head was excluded in all maps due to layer segmentation errors. The location of the optic nerve head was automatically detected from the en-face images and directly transferred onto the choroidal thickness map, as seen in Figure 16a. The resulting thickness maps were then converted from pixel to microns by a conversion factor of 1.9531, which is based on the fraction of true scan depth in microns to the image scan depth in pixels. Subsequently, the full scan area was divided into 13 extended wide-field Early Treatment of Diabetic Retinopathy Study (ETDRS) [Early Treatment Diabetic Retinopathy Study Research Group, 1985] sectors with radii of 0.5 mm, 1.5 mm, 3 mm and 6 mm, as depicted in Figure 16b. The median thickness value within a ETDRS region was chosen as the representative thickness value of the particular ETDRS area.

5.5.4 Data analysis

Retinal shape calculation, foveal pit fitting, processing of the retinal and choroidal thickness maps and further statistical data analysis were performed in MATLAB (MATLAB 2019a, The MathWorks, Inc., Natick, MA, USA). Due to the partial non-parametric distribution of the investigated parameters, absolute values are given as median $\pm$ IQR. In case of retinal radius of curvature and foveal pit morphology, the ratios between horizontal and vertical measurement angles were additionally calculated, in order to find potential growth asymmetries between meridians.
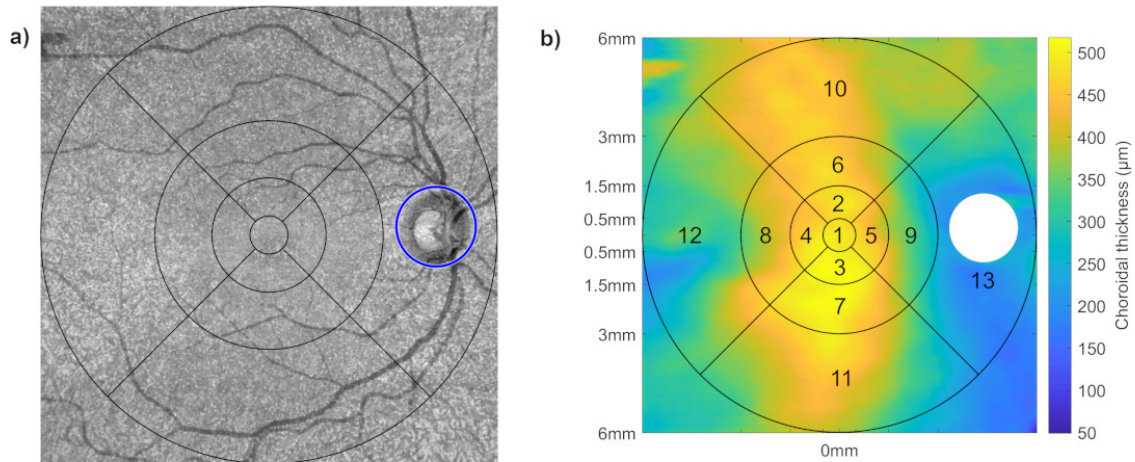
Figure 16: a) Automatic detection of the location of the optic nerve head and visualization of ETDRS sectors on the en-face scan image of an example participant. b) Extracted choroidal thickness map of the same participant together with the 13 wide-field ETDRS areas and the excluded thickness data from the optic nerve head.

Spearman correlation was used to analyze the correlation coefficient ρ between the retinal parameters and axial length and spherical refractive error. P-values $p < 0.05$ were considered as significant.

Data availability

The datasets generated during and/or analyzed during the current study are available from the corresponding author on reasonable request.

Acknowledgements

The authors thank Kerstin Studtrucker for her support during data collection.

Author contributions statement

KB conducted the measurements and analyzed the data. AO and SW conceived the study and provided materials. All authors were involved in the writing process of the manuscript.

Competing interests

Funding

6 Comparison of retinal shape estimation via peripheral refraction vs. OCT

6.1 Abstract

Retinal shape presents a clinical parameter of interest for myopia, and has commonly been inferred indirectly from peripheral refraction (PRX) profiles. Distortion-corrected optical coherence tomography (OCT) scans offer a new and direct possibility for retinal shape estimation. The current study compared retinal curvatures derived from OCT scans vs. PRX measurements in three refractive profiles (0° and 90° meridians, plus spherical equivalent) for 25 participants via Bland-Altman analysis. The radial differences between both procedures were correlated to axial length using Pearson correlation. In general, PRX- and OCT-based retinal radii showed low correlation (all intraclass correlation coefficients < 0.21). PRX found flatter retinal curvatures compared to OCT, with the highest absolute agreement found with the 90° meridian (mean difference $+0.08\,\mathrm{mm}$) and lowest in the 0° meridian (mean difference $+0.89\,\mathrm{mm}$). Moreover, a negative relation between axial length and the agreement of both methods was detected especially in the 90° meridian ($R = -0.38$, $p = 0.06$). PRX measurements tend to underestimate the retinal radius with increasing myopia when compared to OCT measurements. Therefore, future conclusions from PRX on retinal shape should be made cautiously. Rather, faster and more clinically feasible OCT imaging should be performed for this purpose.

6.2 Introduction

Myopia is a spherical refractive error that commonly results from a mismatch between the focal and axial length of the eye. As the eye undergoes excessive growth, the risks for sight-threatening ocular pathologies, such as myopic macular degeneration and retinal detachment, are strikingly enhanced in myopes [Saw et al., 2005]. Due to various factors (see the review in [Read et al., 2019b]), its prevalence is estimated to increase, affecting up to half of the global population by the year 2050 [Holden et al., 2016] and leading to a public-health and socioeconomic burden [Chiang et al., 2014].

Peripheral refraction (PRX) was reported to play a substantial role in myopia development [Neil Charman and Radhakrishnan, 2010]. In monkeys, for example, the induction of peripheral hyperopic defocus - even in combination with foveal ablation - resulted in central axial elongation [Smith III et al., 2009]. Additionally, it was found in humans that uncorrected myopes show more relative peripheral hyperopia than emmetropes and hyperopes [Rempt et al., 1971; Millodot, 1981; Seidemann et al., 2002; Chen et al., 2010; Sng et al., 2011]. However, from longitudinal studies, it has been suggested that relative peripheral hyperopia is a consequence rather than the cause of myopia [Atchison, 2012; Atchison et al., 2015; Mutti et al., 2011]. Moreover, the basis of retinal shape is interwoven with PRX and has commonly been concluded from PRX profiles [Verkicharla et al., 2012]. The more relative the peripheral hyperopia exhibited is, the steeper and the more prolate the retina is suggested to be, as in the case of myopia [Schmid, 2003; Mutti et al., 2000; Logan et al., 2004; Verkicharla et al., 2016]. However, it has already been stated that conclusions from PRX about retinal shape should be made cautiously, especially with respect to the high variability of off-axis ocular optics [Verkicharla et al., 2012]. Nowadays, retinal shape can also be estimated using optical coherence tomography (OCT) in a clinically feasible manner. Here, the myopic retina was found to grow in a balloon-like fashion across the horizontal scan field [Breher et al., 2020a], which partly stands in conflict with the previously predicted steepening of the retina as indirectly derived from PRX.

To the best of the authors' knowledge, there have not yet been any studies conducted in order to analyze the agreement between the direct OCT-based retinal shape versus the indirect PRX-based retinal shape. Therefore, the present study will investigate the agreement of OCT- and PRX-based retinal curvature. It will evaluate whether a direct transfer from PRX to retinal shape can be recommended or if these two parameters should be considered separately. These findings are of interest for clinical environments when choosing the preferred procedure for retinal shape estimation for individual myopia progression follow ups, but also for individualized myopia control choices and efficacy evaluations.

6.3 Materials and Methods

6.3.1 Study participants

This prospective, monocentric, and cross-sectional study was carried out at the Institute for Ophthalmic Research in Tübingen, Germany. It followed the Declaration of Helsinki and data protection regulations, and was approved by the ethics committee of the Medical Faculty of the University of Tübingen. Informed consent was obtained from every participant prior to the study measurements.

Participants with ocular pathologies, previous ocular surgery, and insufficient OCT signal strength < 6 - and, thus, reduced image quality of the OCT scans - were excluded. A total of n $= 25$ participants with a mean age of 24.6 ± 4.0 years (range 19 to 35 years) were included in the study. Measurements were performed on undilated right eyes. The mean axial length (ZEISS IOLMaster 700, Carl Zeiss Meditec AG, Jena, Germany) was 23.89 ± 0.75 mm (range 22.59 to 25.17 mm). The mean central refractive error (i.Profiler plus, ZEISS Vision, Aalen, Germany) was -1.07 ± 1.60 D (range -5.14 to +0.57 D). The group consisted of 14 emmetropes and 11 myopes.

6.3.2 OCT-based retinal shape estimation

Swept-source OCT imaging (ZEISS PlexElite 9000, Carl Zeiss Meditec Inc., Dublin, USA) was performed for retinal imaging with subsequent retinal shape calculation. The OCT scan pattern consisted of a horizontal 16 mm (approximately 52°) line scan, which was centered on the fovea. In order to estimate the retinal shape, the OCT scan first had to be corrected for the scan geometry distortions. These geometrical distortions arise from the artificial flattening of the OCT image due to display reasons. A newly developed and validated optical model by Steidle and Straub [Steidle and Straub, 2018] was used to perform the geometrical distortion correction. This was achieved via ray-tracing of the OCT A-scans through the optical components of the OCT device and the Arizona eye model [Schwiegerling, 2004] with the individually adjusted axial length of the participant using MATLAB (MATLAB 2018b, The MathWorks, Inc., Natick, MA, USA) and OpticStudio (OpticStudio, Zemax, LLC, Kirkland, WA, USA). After re-construction of the geometrically correct scan, the retinal radius of curvature was extracted from a circle that was fitted to the retinal pigment epithelium (RPE) of the OCT image (see Figure 17). This will be stated as the "OCT-based retinal curvature" hereinafter.

6.3.3 PRX-based retinal shape estimation

PRX measurements were performed using eccentric photorefraction as described elsewhere [Tabernero and Schaeffel, 2009a], but with the horizontal meridian being measured additionally in the same manner. The photorefractor consisted of a moving mirror to scan from the temporal to the nasal retina across a $\pm 50°$ scan field (measurement angle α). The sampling rate was $0.71°$. The fixation target was mounted in front of the right eye, such that profiles were measured in the primary gaze direction of the participants and were centered on the fovea. The photorefractor measures the vertical and horizontal profiles of refraction after each other—the 0° and 90° refractive meridians.
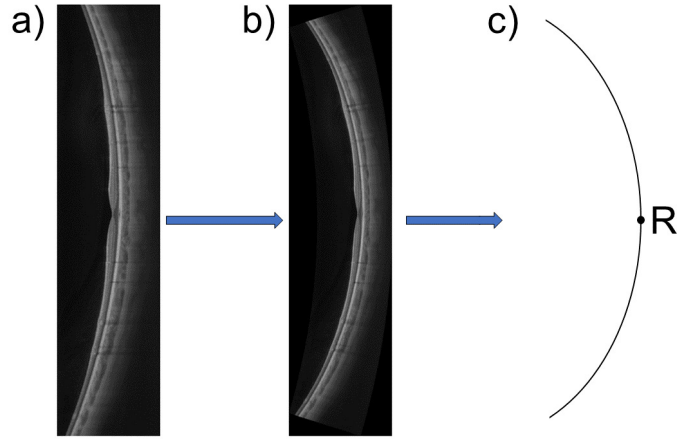
Figure 17: Process of retinal shape calculation from optical coherence tomography (OCT) imaging: (**a**) the original OCT scan; (**b**) the distortion-corrected OCT scan; (**c**) a circle is fitted to the retinal pigment epithelium (RPE) of the corrected scan image, and its radius is extracted for retinal shape estimation. The point "R" on this circle scheme is displayed for better reference to Figure 18.

The spherical equivalent profile was calculated as the average of the 0° and 90° meridian values. One measurement cycle was repeated from 7 to 14 times for each participant, depending on the compliance. With this repetitive procedure, assessment of the cylindrical refractive error was shown to lie within an intra-subject range of 0.15 D [Gekeler et al., 1997].

Subsequently, the 0° and 90° meridian profiles were normalized to zero in order to obtain the relative PRX. Afterwards, they were size-adapted according to the participant's axial length to match the angular size of the OCT line scan. The measured defocus in diopters for each eccentricity was then converted into millimeters by a factor of 0.32 mm per diopter, as derived from the optical properties of the Arizona eye model [Schwiegerling, 2004]. Subsequently, the reverse defocus shift Δz in millimeters was applied to the retina of the eye model with a baseline radius of 13.4 mm, as drawn schematically in Figure 18. The resulting shift of the baseline retina simulates the assumed retinal shape.

It is noteworthy that the eccentricity angles for the PRX measurements are relative to the axial-length-adjusted position of the nodal point N in the eye. However, this point does not coincidence with the circle center C of the baseline radius for the retina on the y-axis (see Figure 18). Therefore, the general circle equations needed to be adjusted in order to calculate the $x_{Z_{(\alpha)}}$ and $y_{Z_{(\alpha)}}$ positions of the points $Z_{(\alpha)}$ resulting from the PRX-defocus shift $\Delta z_{(\alpha)}$. This calculation was performed for each measurement angle α separately via Equation (10).
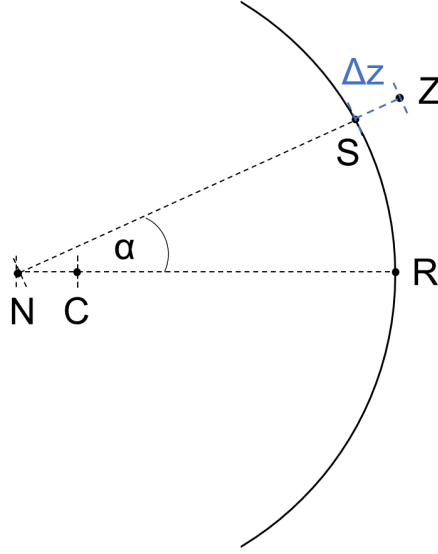
Figure 18: Process of retinal shape calculation from PRX measurements: scheme of an eye with the retinal curvature of the Arizona eye model [Schwiegerling, 2004], its circle center C, and ocular nodal point N (adjustable for the axial length). For each scan angle α, the peripheral refraction (PRX) shift Δz was added or subtracted for myopic or hyperopic defocus to the length $\overline{NS}$, respectively. A circle was then fitted to all resulting points Z. The image displays the case of myopic defocus and a subsequent elongation of $\overline{NS}$ by Δz.

$$\begin{pmatrix} x_{Z_{(\alpha)}} \\ y_{Z_{(\alpha)}} \end{pmatrix} = \begin{pmatrix} 0 \\ -\overline{CN} \end{pmatrix} + (\overline{NS}_{(\alpha)} - \Delta z_{(\alpha)}) \cdot \begin{pmatrix} \sin\alpha \\ \cos\alpha \end{pmatrix} \tag{10}$$

Here, $\overline{NS}_{(\alpha)}$ represents the distance between the nodal point and the original eye model circle under a given angle α and is derived from Equation (11).

$$\overline{NS}_{(\alpha)} = \overline{CN} \cdot \cos\alpha + \sqrt{\overline{CN}^2 \cdot \cos^2\alpha - \overline{CN}^2 + \overline{CR}^2} \tag{11}$$

As a last and equal step to the previously explained fitting procedure from OCT, a circle was fitted to the re-arranged points $Z_{(\alpha)}$. This radius was considered as the retinal radius of curvature, hereinafter called the "PRX-based retinal curvature".

6.3.4   Statistical data analysis

Data analysis was carried out with the help of MATLAB (MATLAB 2020a, The Math-Works, Inc., Natick, MA, USA). Normal distribution was ensured with the Lilliefors test [Lilliefors, 1967].

A t-test was performed in addition to Bland-Altman analysis [Bland and Altman, 1999] and the calculation of the intraclass correlation coefficient (ICC(2,1)) [Shrout and Fleiss, 1979] in order to investigate the statistical differences and agreement between the OCT- and PRX-based retinal curvatures. Bivariate correlation analysis was performed with Pearson correlation [Edwards, 1984]. Statistical results were interpreted as significant in the case that $p < 0.05$.

6.4 Results

The mean retinal radii from the OCT measurements and from the PRX meridians were as follows: $12.73 \pm 1.05\,\mathrm{mm}$ (OCT), $13.63 \pm 1.14\,\mathrm{mm}$ (PRX, 0° meridian), $12.82 \pm 0.51\,\mathrm{mm}$ (PRX, 90° meridian), and $13.18 \pm 0.52\,\mathrm{mm}$ (PRX, spherical equivalent).

OCT- and PRX-based retinal curvatures were compared for both meridians and the spherical equivalent values. The t-test, ICC, and Bland-Altman results are shown in Table 9. All investigated refraction profiles showed poor reliability for both measurement methods, with ICCs < 0.5. The t-tests exposed a significant difference between the OCT-based retinal curvature and PRX-based retinal curvature in the 0° meridian ($p = 0.01$). However, the differences of the spherical equivalent profile and the 90° meridian were only borderline significant and non-significant, respectively ($p = 0.07$ and $p = 0.71$). These findings fit to the Bland-Altman results.

Table 9: T-test, ICC and Bland-Altman analysis of the PRX-based retinal curvature for three refractive profiles versus the OCT-based retinal curvature ($n = 25$).

	0° meridian	90° meridian	Spherical equivalent
ICC analysis			
ICC	0.18	0.20	0.03
p-value	0.65	0.29	0.47
Bland-Altman analysis (mm)			
Mean difference	+0.89	+0.08	+0.45
Upper limit of agreement	+4.04	+2.36	+2.72
[95% confidence interval]	[+2.89 to +5.19]	[+1.45 to 3.02]	[+1.89 to +3.55]
Lower limit of agreement	-2.26	-2.07	-1.83
[95% confidence interval]	[-1.11 to -3.41]	[-1.28 to -2.85]	[-1.00 to -2.66]
T-test			
H_0 / H_1	H_1	H_0	H_0
p-value	0.01	0.07	0.71

The Bland-Altman agreement revealed a positive mean difference in all meridians, meaning that the PRX-based retinal curvature was estimated to be larger than the OCT-based retinal curvature on average. The largest discrepancy was present for the 0° meridian (mean difference = +0.89 mm (-2.26 to +4.04 mm)), whereas the 90° meridian showed the best agreement (+0.08 mm (-2.07 to +2.36 mm)). As expected, the agreement for the spherical equivalent meridian was located in between (+0.45 mm (-1.83 to 2.72 mm)). The width of the limits of agreement was also largest for the 0° meridian, followed by the spherical equivalent and the 90° meridian with 6.30 mm, 4.55 mm, and 4.43 mm, respectively. Figure 19 visualizes the Bland-Altman analysis from Table 9. There was a notable trend for the 90° meridian and the spherical equivalent in Figure 19b,c. Here, the generally positive mean difference turned into a generally negative difference with increasing retinal radius of curvature.
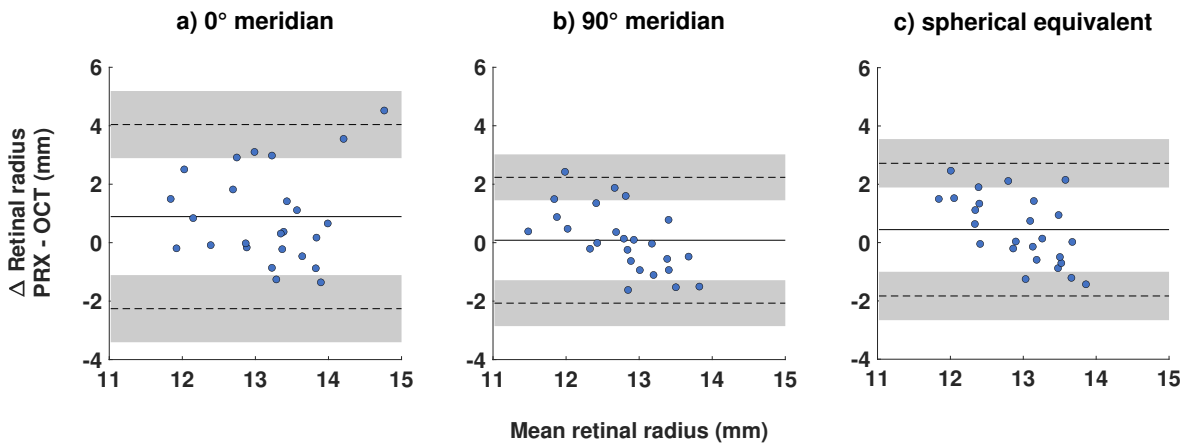
Figure 19: Bland-Altman plots for the comparison between PRX- and OCT-based retinal radii of curvature (n = 25) for the (**a**) 0° refractive meridian, (**b**) 90° refractive meridian, and (**c**) spherical equivalent refraction.

As the OCT-based retinal radius increases with myopia [Breher et al., 2020a], a correlation analysis between the radial difference and axial length was performed. The expected negative correlation between PRX- and OCT-based retinal curvature and axial length could be shown for all refractive meridians (see Figure 20). However, only the regression for the 90° meridian was borderline significant (R = −0.38; p = 0.06).

6.5 Discussion

The study compared PRX- and OCT-based retinal shapes with each other and in relation to axial length. It provided evidence that OCT-based and PRX-based retinal shapes differ from each other, revealing low ICCs. The PRX-based retinal radius was estimated to be larger compared to the OCT-based radius for all three investigated refractive profiles (0° and 90° meridians and spherical equivalent).

a) 0° meridian

y = -0.29x + 7.70
R = -0.13 (p = 0.53)

b) 90° meridian

y = -0.56x + 13.41
R = -0.38 (p = 0.06)

c) spherical equivalent

y = -0.42x + 10.47
R = -0.27 (p = 0.19)

Δ Retinal radius PRX - OCT (mm)

Axial length (mm)

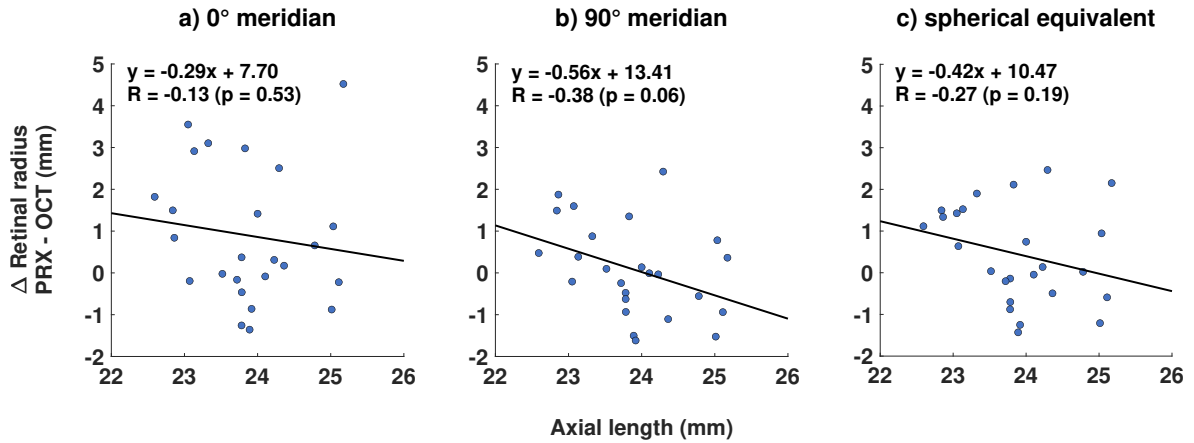Figure 20: Linear regression equations and coefficients for the relation between axial length and the discrepancy of PRX- and OCT-based retinal radii of curvature (n = 25) for the (**a**) 0° refractive meridian, (**b**) 90° refractive meridian, and (**c**) spherical equivalent refraction.

The highest absolute deviations were revealed in the 0° meridian, and the lowest in the 90° meridian. This difference in retinal shape of 0.81 mm between meridians might arise from the increase of astigmatism in the peripheral retina, corresponding to approximately 2.5 D, as reported in [Gustafsson et al., 2001; Lotmar and Lotmar, 1974; Calver et al., 2007]. Furthermore, this fact supports the hypothesis that direct methods of retinal shape estimation, such as OCT or magnetic resonance imaging (MRI), might lead to more reliable and stable results, as these are independent from eccentricity-related refractive fluctuations. In fact, absolute differences are low (on average, less than 1 mm), but more importantly, the discrepancy in the agreement is inconsistent across the range of evaluated retinal curvatures and axial lengths. With increasing axial length, the Δ(PRX-OCT) difference of radii decreased, and eventually even became negative. This tendency could be interpreted as an overestimation of PRX-based retinal steepness with increasing axial length and, therefore, myopia. Vice versa, it could be described as an overestimation of PRX-based retinal flatness with decreasing axial length and, therefore, emmetropia or hyperopia. This effect could be explained by the influence of higher-order aberrations occurring with off-axis refraction. Higher-order aberrations alone sum up to 0.9 D in the periphery (assuming a 4 mm pupil) [Lundström and Rosén, 2017] and, therefore, can change measurements from refraction when only lower-order aberrations are considered. As recently found, PRX profiles in emmetropic children show much flatter courses with less relative peripheral myopia and inter-subject variability when measured with an open-field wavefront aberrometer over ±30° of visual field [Lan et al., 2019]. Using the same wavefront aberrometer technique, myopes also show flatter profiles with less relative peripheral hyperopia than usually reported [Wang et al., 2020].

These findings would, in turn, lead to larger PRX-based retinal curvatures in myopia and smaller retinal curvatures in emmetropia, and are thus a better match with the OCT-based retinal shapes.

When comparing these results to previous literature, there are inconsistent findings due to methodological differences. The most important study to recognize in this context is by Verkicharla et al. [Verkicharla et al., 2015]. They compared optical biometry and Dunne's method [Dunne et al., 1987; Dunne, 1995] (Gullstrand eye model based on PRX modeling) for retinal shape estimations, and compared them to the ground truth of magnetic resonance imaging (MRI). Dunne's method was less appropriate than optical biometry and showed flatter retinal shapes of 1.7 mm compared to MRI contours. In this sense, the aforementioned study agrees that PRX is not ideally suited for estimating retinal contour. The smaller mean difference in the current study most likely arises from the usage of the same eye model for OCT- and PRX-based retinal shape estimations. It is further noteworthy that the present study considered the OCT-based retinal shape as the ground truth instead of MRI. Nevertheless, a good agreement between the retinal shapes measured via MRI and distortion-corrected OCT scans was found previously [Kuo et al., 2016]. OCT also provides a faster, more clinically feasible, and less expensive method for retinal imaging than MRI. With a somewhat different methodology, but with a similar purpose to that of the present study, Schmid [Schmid, 2003] found that relative peripheral hyperopia predicts more retinal steepness in children, but that there is considerably high inter-subject variability in both parameters. Similar results were found later in adults [Verkicharla et al., 2016]. However, both studies used an open-field autorefraction and optical biometry with off-axis fixation via eye turns, as opposed to the eccentric photorefraction and OCT measurements with constant primary gaze position in the current study.

The strengths of this current study are laid down in the methodology. A fast eccentric photorefractor [Tabernero and Schaeffel, 2009a] was used, which abolishes the need for eye movements for peripheral fixation targets. The same advantage accounts for the OCT measurements vs. optical biometry. Moreover, the sampling rate was higher for both parameters of interest. For PRX, measurements were performed in steps of 0.71° instead of 5° to 10° steps, as with common open-field autorefractors. With regards to OCT, each 11th A-scan out of a total of 1024 A-scans was used for the retinal shape estimation, which corresponds to a sampling rate of approximately 0.6°. However, there are also certain limitations present with the current study. Despite consisting of myopes and emmetropes, the sample lacked highly myopic participants with an axial length of >26 mm, which could have led to more pronounced and significant differences and correlation results.

Moreover, the prevalence of staphyloma [Zheng et al., 2020] increases with higher degrees of myopia, leading to more irregular retinal shapes and PRX profiles, as well as an unknown relationship between them. The eye model was adjusted for the individual axial length, but not for other optical components, such as corneal curvature. However, tolerance analysis showed that axial length appears to be the largest error source for retinal shape calculation (up to ± 4 mm misestimation), while corneal curvature or lens refractive index account for only up to ± 0.2 and ± 0.1 mm of misjudgment [Steidle and Straub, 2018]. The Arizona eye model [Schwiegerling, 2004] figured as the baseline for the conversion from diopters to millimeters for the PRX-assumed retinal shape. However, this conversion factor was not adjusted for the individual participants with their refractive ocular properties, but was rather inferred from the eye model. This could lead to inaccuracies, which are pronounced in the peripheral measurement angles. Moreover, only the horizontal visual field was investigated in the current study due to the technical set-up of the photorefractor, which did not allow conclusions for the vertical visual field. The first rough suggestions match in the sense that PRX profiles [Atchison et al., 2006], as well as retinal curvature [Breher et al., 2020a], have been shown in separate studies to be less affected by myopia in the vertical visual field than horizontal visual field.

The current study showed that retinal shape should be preferably inferred from direct imaging methods, such as OCT instead of an indirect estimation from PRX profiles. However, the measurements of PRX should not be neglected at all, since it is of very high importance especially in the field of myopia control. In contrast to retinal shape (which figures more as a biomarker still), PRX can be altered in a clinically feasible way using optical treatment strategies, such as orthokeratology [Queirós et al., 2018, 2010], progressive addition spectacle lenses [Berntsen et al., 2013], multifocal contact lenses [Kang et al., 2013] or refractive surgery [Queirós et al., 2012]. The overall aim of these options is to shift PRX into a myopic direction, where orthokeratology lenses show a particular strong effect mainly outside of 15° eccentricity in four investigated directions [Queirós et al., 2018]. Therefore, it is recommended that future studies and clinical applications should strive for an evaluation of PRX and retinal shape as separately measured parameters, albeit brought into a meaningful combination.

From the study results, it can be concluded that retinal shape measurements from PRX measurements lead to overall larger retinal radii compared to radii derived from distortion-corrected OCT imaging. However, this relationship is reversed with increasing axial length, where PRX tends to underestimate the radius of the retina when compared to OCT. Therefore, future studies should rely more on direct retinal shape estimations from OCT rather than indirectly inferring it from PRX measurements, especially in the context of myopia.

7 Summary

The primary purpose of the work was to assess and enhance OCT-based retinal bio-markers used in human myopia research in the context of advancing OCT technologies. The individual studies provided insights into the repeatability of automated choroidal thickness measurements with spectral-domain and swept-source OCT. Moreover, the work assessed wide-field topographical choroidal vascularity, retinal and foveal shape in relation to myopia. Finally, novel procedures of retinal shape measurements were compared to peripheral refraction as previously used method for this purpose. The results of the presented work lead to the following conclusions:

(1) The repeatability and agreement of two spectral-domain OCT devices combined with automated choroidal thickness measurements vary across the macular area. It was shown that repeatability and agreement were improved in nasal sectors and with increasing eccentricity. Moreover, the found repeatability exceeds previously stated effect sizes of choroidal thickness changes in human myopia research. These findings were mainly caused by the limited scan depth of spectral-domain OCT devices. They will have implications on the measurement locations and interpretation of choroidal thickness changes in future studies.

(2) Swept-source OCT provides better repeatability values from the automated choroidal thickness and choroidal vascularity measurements, more similar to found effect sizes in previous human studies. Moreover, the results confirmed typical choroidal thickness distribution across the retina and varying choroidal thinning with myopia. In contrast, choroidal vascularity did not exhibit a clear topographical pattern: it tended to increase within the macula but decreased outside of the macula in myopes. This experiment was the first to develop and apply a wide-field, volumetric analysis of choroidal thickness and vascularity as choroidal biomarkers.

(3) Wide-field retinal shape growth in myopia is affected differently in vertical and horizontal meridians: The retinal radius of curvature in the horizontal meridian increases with axial length, whereas the vertical retinal radius of curvature remains relatively stable. Moreover, it was found that foveal pit shape is not affected by myopia and that choroidal thickness seems to be more associated with refractive error than axial length. These results provided insight into the retina's myopia-related growth patterns with the retinal radius of curvature as a potential biomarker, assessed via a newly implemented, clinically feasible and wide-field OCT procedure.

(4) There is only low agreement between the OCT-based and peripheral refraction-based method to derive retinal shape. Moreover, this agreement is dependent on axial length, where retinal radii were overestimated with relatively shorter axial length but underestimated with longer axial length. Therefore, the study provided evidence that the inference from peripheral refraction to retinal shape should be only made with caution. Rather, they should be considered in a complementary fashion with each other.

Despite the range of findings in the current work, this field requires further research to apply and enhance the established methodology and to bring it into context with other aspects of myopia research. Future developments in OCT technology, such as a wider field of view or improved scan resolution are of high interest. A higher axial resolution could further improve reliability in studies involving ocular structures in the range of microns, such as the choroid. Moreover, image processing algorithms for the analysis of OCT images undergo constant progress especially in combination with artificial intelligence and big data. Data collection could be enhanced through further milestones in the technical direction of OCT development, such as remote care using low-cost and/or miniaturized OCT devices.

Other improvements are based on the modulation of OCT scan images: one could further individualize the optical model behind the distortion-correction to abolish remaining inaccuracies in the correction of OCT scan images. Besides, the description of retinal shape in a three-dimensional manner will enable further steps to merge the dynamics of environmental and ocular properties in a static and eventually dynamic manner. Along this line, the distortion-correction of OCT scans offers great potential not only for retinal shape analysis but also to derive corrected layer proportions and thicknesses. Here, the correction of choroidal thickness maps will become more crucial with wider scan angles and higher refractive errors.

Furthermore, the developed methodology should be applied in clinical studies. Here, longitudinal studies in children can give insight into structural processes before and during myopia onset and progression, as well as with myopia control strategies. In addition, the interpretation and transfer of choroidal thickness, choroidal vascularity and retinal shape as promising OCT-based biomarkers should be further researched with respect to long-term axial length changes. These findings will present a great step forward potential acceleration in the field of OCT-based human research.

8   Zusammenfassung

Das primäre Ziel der Arbeit war die Bewertung und Verbesserung OCT-basierter retinaler Biomarker im Kontext fortschreitender OCT-Technologie, die in der Myopieforschung beim Menschen eingesetzt werden. Die einzelnen Studien lieferten Einblicke in die Wiederholbarkeit von automatisierten Aderhautdickenmessungen mittels spectral-domain und swept-source OCT. Darüber hinaus wurde die topographische Aderhautvaskularität im Weitwinkelbereich sowie die Form der Netzhaut und der Fovea in Abhängigkeit von der Kurzsichtigkeit bewertet. Schließlich wurden neuartige Verfahren zur Messung der Netzhautform mit der peripheren Refraktion verglichen. Die Ergebnisse der vorgestellten Arbeit führen zu folgenden Schlussfolgerungen:

(1) Die Wiederholbarkeit und Übereinstimmung von zwei spectral-domain OCT-Geräten in Kombination mit automatisierten Aderhautdickenmessungen variieren über den Makulabereich. Es konnte gezeigt werden, dass die Wiederholbarkeit und Übereinstimmung in nasalen Sektoren und mit zunehmender Exzentrizität verbessert wurden. Darüber hinaus übersteigt die Wiederholbarkeit bisher angegebene Effektgrößen von Aderhautdickenänderungen in der menschlichen Myopieforschung. Diese Befunde wurden hauptsächlich durch die begrenzte Scantiefe der spectral-domain OCT-Geräte verursacht. Diese Ergebnisse haben Auswirkungen auf die Messorte und die Interpretation von Aderhautdickenänderungen in zukünftigen Studien haben.

(2) Das swept-source OCT liefert bessere Wiederholbarkeitswerte der automatisierten Messungen von Aderhautdicke und der choroidalen Vaskularität, die den gefundenen Effektgrößen in früheren Studien näher kommen. Darüber hinaus bestätigten die Ergebnisse die typische Verteilung der Aderhautdicke über die Netzhaut und die unterschiedliche Verdünnung der Aderhaut bei Myopie. Im Gegensatz dazu zeigte die Aderhautvaskularität kein klares topographisches Verteilungsmuster: sie nahm bei Myopen tendenziell innerhalb der Makula zu, aber außerhalb der Makula ab. Dieses Experiment war das erste, in dem eine volumetrische Weitfeldanalyse der Aderhautdicke und der Aderhautvaskularität als choroidale Biomarker entwickelt und angewendet wurde.

(3) Die Weitfeld Netzhautform wird bei Kurzsichtigkeit in vertikalen und horizontalen Meridianen unterschiedlich beeinflusst: Der retinale Krümmungsradius im horizontalen Meridian nimmt mit der Augenlänge zu, während der vertikale retinale Krümmungsradius relativ stabil bleibt. Darüber hinaus wurde festgestellt, dass die Form der Fovea nicht von der Myopie beeinflusst wird und dass die Dicke der Aderhaut eher mit dem Refraktionsfehler als mit der Achsenlänge assoziiert zu sein scheint. Diese Ergebnisse lieferten einen Einblick in die myopiebedingten Wachstumsmuster der Netzhaut mit dem retinalen Krümmungsradius als potenziellem Biomarker, der mittels eines neu implementierten, klinisch durchführbaren OCT-Verfahrens ermittelt wird.

(4) Es besteht nur eine geringe Übereinstimmung zwischen der OCT-basierten und der auf peripherer Refraktion basierenden Methode zur Ableitung der Netzhautform. Außerdem ist diese Übereinstimmung abhängig von der axialen Länge, wobei die Netzhautradien bei relativ kurzer axialer Länge überschätzt, bei längerer axialer Länge jedoch unterschätzt wurden. Daher liefert die Studie Hinweise darauf, dass der Rückschluss von der peripheren Refraktion auf die Netzhautform nur mit Vorsicht erfolgen sollte. Vielmehr sollten sie ergänzend zueinander betrachtet werden.

Trotz der Bandbreite der Ergebnisse in der aktuellen Arbeit sind auf diesem Gebiet weitere Forschungen erforderlich, um die etablierte Methodik anzuwenden und zu verbessern und sie in einen Kontext mit anderen Aspekten der Myopieforschung zu bringen. Zukünftige Entwicklungen in der OCT-Technologie, wie z.B. ein größeres Sichtfeld oder eine verbesserte Scan-Auflösung, sind von hohem Interesse. Eine höhere axiale Auflösung könnte die Zuverlässigkeit bei Studien, die okulare Strukturen im Mikrometerbereich, beispielsweise die Aderhaut, betreffen, weiter verbessern. Darüber hinaus werden die Bildverarbeitungsalgorithmen für die Analyse von OCT-Bildern ständig weiterentwickelt, insbesondere in Kombination mit künstlicher Intelligenz und Big Data. Die Datenerfassung könnte durch weitere Meilensteine in der technischen Richtung der OCT-Entwicklung verbessert werden, wie z.B. die Fernbetreuung mit kostengünstigen Geräten und/oder miniaturisierten OCT-Geräten.

Andere Verbesserungen basieren auf der Modulation von OCT Scan-Bildern: Man könnte das optische Modell hinter der Verzerrungs-Korrektur weiter individualisieren, um verbleibende mögliche Ungenauigkeiten bei der Korrektur von OCT-Scanbildern zu beseitigen. Außerdem wird die dreidimensionale Beschreibung der Netzhautform weitere Schritte ermöglichen, um die Dynamik der Umgebungs- und Augeneigenschaften auf statische und schließlich dynamische Art zu verschmelzen. In diesem Sinne bietet die Verzerrungskorrektur von OCT-Scans ein großes Potential nicht nur für die Analyse der Netzhautform, sondern auch für die Ableitung korrigierter Schichtproportionen und -dicken. Dabei wird die Korrektur von Aderhautdickenkarten mit größeren Scanwinkeln und höheren Brechungsfehlern noch entscheidender werden.

Weiterhin sollte die entwickelte Methodik in klinischen Studien angewendet werden. Hier können longitudinale Studien bei Kindern Einblicke in strukturelle Prozesse vor und während des Auftretens und Progression der Myopie sowie bei Myopiekontrollstrategien geben. Darüber hinaus sollten Aderhautdicke, -vaskularität und Netzhautform als vielversprechende OCT-basierte Biomarker hinsichtlich ihrer Übertragung auf langfristige Achsenlängenänderungen validiert werden. Diese Ergebnisse stellen einen großen Schritt vorwärts dar und könnten die OCT-basierte Forschung am Menschen beschleunigen.

9 References

Agawa, T., Miura, M., Ikuno, Y., Makita, S., Fabritius, T., Iwasaki, T., Goto, H., Nishida, K., and Yasuno, Y. (2011). Choroidal thickness measurement in healthy japanese subjects by three-dimensional high-penetration optical coherence tomography. *Graefe's Archive for Clinical and Experimental Ophthalmology*, 249(10):1485.

Agrawal, R., Chhablani, J., Tan, K.-A., Shah, S., Sarvaiya, C., and Banker, A. (2016a). Choroidal vascularity index in central serous chorioretinopathy. *Retina*, 36(9):1646–1651.

Agrawal, R., Ding, J., Sen, P., Rousselot, A., Chan, A., Nivison-Smith, L., Wei, X., Mahajan, S., Kim, R., Mishra, C., et al. (2020). Exploring choroidal angioarchitecture in health and disease using choroidal vascularity index. *Progress in Retinal and Eye Research*, page 100829.

Agrawal, R., Gupta, P., Tan, K.-A., Cheung, C. M. G., Wong, T.-Y., and Cheng, C.-Y. (2016b). Choroidal vascularity index as a measure of vascular status of the choroid: measurements in healthy eyes from a population-based study. *Scientific reports*, 6:21090.

Agrawal, R., Salman, M., Tan, K.-A., Karampelas, M., Sim, D. A., Keane, P. A., and Pavesio, C. (2016c). Choroidal vascularity index (cvi)-a novel optical coherence tomography parameter for monitoring patients with panuveitis? *PLoS One*, 11(1).

Agrawal, R., Seen, S., Vaishnavi, S., Vupparaboina, K. K., Goud, A., Rasheed, M. A., and Chhablani, J. (2019). Choroidal vascularity index using swept-source and spectral-domain optical coherence tomography: a comparative study. *Ophthalmic Surgery, Lasers and Imaging Retina*, 50(2):e26–e32.

Agrawal, R., Wei, X., Goud, A., Vupparaboina, K. K., Jana, S., and Chhablani, J. (2017). Influence of scanning area on choroidal vascularity index measurement using optical coherence tomography. *Acta ophthalmologica*, 95(8):e770–e775.

Akyol, N., Kükner, A., Ozdemir, T., and Esmerligil, S. (1996). Choroidal and retinal blood flow changes in degenerative myopia. *Canadian journal of ophthalmology. Journal canadien d'ophtalmologie*, 31(3):113–119.

Alonso-Caneiro, D., Read, S. A., and Collins, M. J. (2011). Speckle reduction in optical coherence tomography imaging by affine-motion image registration. *Journal of Biomedical Optics*, 16(11):116027.

Alonso-Caneiro, D., Read, S. A., and Collins, M. J. (2013). Automatic segmentation of choroidal thickness in optical coherence tomography. *Biomedical Optics Express*, 4(12):2795–2812.

Alshareef, R. A., Khuthaila, M. K., Goud, A., Vupparaboina, K. K., Jana, S., and Chhablani, J. (2017a). Subfoveal choroidal vascularity in myopia: evidence from spectral-domain optical coherence tomography. *Ophthalmic Surgery, Lasers and Imaging Retina*, 48(3):202–207.

Alshareef, R. A., Khuthaila, M. K., Januwada, M., Goud, A., Ferrara, D., and Chhablani, J. (2017b). Choroidal vascular analysis in myopic eyes: evidence of foveal medium vessel layer thinning. *International journal of retina and vitreous*, 3(1):28.

Artal, P. (2017). *Handbook of Visual Optics, Two-Volume Set*. CRC Press.

Atchison, D. and Smith, G. (2000). *Optics of the human eye*. Butterworth Heinemann.

Atchison, D. A. (2012). The glenn a. fry award lecture 2011: peripheral optics of the human eye. *Optometry and Vision Science*, 89(7):E954–E966.

Atchison, D. A. and Charman, W. N. (2011). Can partial coherence interferometry be used to determine retinal shape? *Optometry and Vision Science*, 88(5):E601–E607.

Atchison, D. A., Jones, C. E., Schmid, K. L., Pritchard, N., Pope, J. M., Strugnell, W. E., and Riley, R. A. (2004). Eye shape in emmetropia and myopia. *Investigative Ophthalmology & Visual Science*, 45(10):3380–3386.

Atchison, D. A., Li, S.-M., Li, H., Li, S.-Y., Liu, L.-R., Kang, M.-T., Meng, B., Sun, Y.-Y., Zhan, S.-Y., Mitchell, P., et al. (2015). Relative peripheral hyperopia does not predict development and progression of myopia in children. *Investigative ophthalmology & visual science*, 56(10):6162–6170.

Atchison, D. A., Pritchard, N., and Schmid, K. L. (2006). Peripheral refraction along the horizontal and vertical visual fields in myopia. *Vision research*, 46(8-9):1450–1458.

Atchison, D. A., Pritchard, N., Schmid, K. L., Scott, D. H., Jones, C. E., and Pope, J. M. (2005). Shape of the retinal surface in emmetropia and myopia. *Investigative Ophthalmology & Visual Science*, 46(8):2698–2707.

Bagherinia, H., Gregori, G., Rosenfeld, P. J., Lyu, C., Noorikolouri, J., Shi, Y., Zheng, F., De Sisternes, L., and Durbin, M. K. (2019). A method for automated choroidal-scleral interface segmentation in optical coherence tomography. *Investigative Ophthalmology & Visual Science*, 60(9):143–143.

Bennett, A. G., Rudnicka, A. R., and Edgar, D. F. (1994). Improvements on littmann's method of determining the size of retinal features by fundus photography. *Graefe's archive for clinical and experimental ophthalmology*, 232(6):361–367.

Berntsen, D. A., Barr, C. D., Mutti, D. O., and Zadnik, K. (2013). Peripheral defocus and myopia progression in myopic children randomly assigned to wear single vision and progressive addition lenses. *Investigative ophthalmology & visual science*, 54(8):5761–5770.

Berntsen, D. A., Sinnott, L. T., Mutti, D. O., Zadnik, K., Group, C. S., et al. (2011). Accommodative lag and juvenile-onset myopia progression in children wearing refractive correction. *Vision research*, 51(9):1039–1046.

Bille, J. F. (2019). High resolution imaging in microscopy and ophthalmology: new frontiers in biomedical optics.

Bland, J. M. and Altman, D. G. (1999). Measuring agreement in method comparison studies. *Statistical Methods in Medical Research*, 8(2):135–160.

Branchini, L., Regatieri, C. V., Flores-Moreno, I., Baumann, B., Fujimoto, J. G., and Duker, J. S. (2012). Reproducibility of choroidal thickness measurements across three spectral domain optical coherence tomography systems. *Ophthalmology*, 119(1):119–123.

Breher, K., Agarwala, R., Leube, A., and Wahl, S. (2019a). Direct modeling of foveal pit morphology from distortion-corrected oct images. *Biomedical Optics Express*, 10(9):4815–4824.

Breher, K., Garcia, M. G., Ohlendorf, A., and Wahl, S. (2018). The effect of the optical design of multifocal contact lenses on choroidal thickness. *PloS One*, 13(11):e0207637.

Breher, K., Ohlendorf, A., and Wahl, S. (2019b). A metrological approach to the analysis of choroidal thickness by optical coherence tomography 3d scans in myopia research. *Scientific Reports*, 9(1):1–9.

Breher, K., Ohlendorf, A., and Wahl, S. (2020a). Myopia induces meridional growth asymmetry of the retina: a pilot study using wide-field swept-source oct. *Scientific RepoRtS*, 10(1):1–8.

Breher, K., Terry, L., Bower, T., and Wahl, S. (2020b). Choroidal biomarkers: A repeatability and topographical comparison of choroidal thickness and choroidal vascularity index in healthy eyes. *Translational Vision Science & Technology*, 9(11):8–8.

Brown, J. S., Flitcroft, D. I., Ying, G.-s., Francis, E. L., Schmid, G. F., Quinn, G. E., and Stone, R. A. (2009). In vivo human choroidal thickness measurements: evidence for diurnal fluctuations. *Investigative ophthalmology & visual science*, 50(1):5–12.

Calver, R., Radhakrishnan, H., Osuobeni, E., and O'Leary, D. (2007). Peripheral refraction for distance and near vision in emmetropes and myopes. *Ophthalmic and Physiological Optics*, 27(6):584–593.

Chakraborty, R., Ostrin, L. A., Nickla, D. L., Iuvone, P. M., Pardue, M. T., and Stone, R. A. (2018). Circadian rhythms, refractive development, and myopia. *Ophthalmic and Physiological Optics*, 38(3):217–245.

Chakraborty, R., Read, S. A., and Collins, M. J. (2011). Diurnal variations in axial length, choroidal thickness, intraocular pressure, and ocular biometrics. *Investigative ophthalmology & visual science*, 52(8):5121–5129.

Chakraborty, R., Read, S. A., and Collins, M. J. (2012). Monocular myopic defocus and daily changes in axial length and choroidal thickness of human eyes. *Experimental eye research*, 103:47–54.

Chakraborty, R., Read, S. A., and Collins, M. J. (2013). Hyperopic defocus and diurnal changes in human choroid and axial length. *Optometry and Vision Science*, 90(11):1187–1198.

Chen, F. K., Yeoh, J., Rahman, W., Patel, P. J., Tufail, A., and Da Cruz, L. (2012). Topographic variation and interocular symmetry of macular choroidal thickness using enhanced depth imaging optical coherence tomography. *Investigative Ophthalmology & Visual Science*, 53(2):975–985.

Chen, M.-J., Liu, Y.-T., Tsai, C.-C., Chen, Y.-C., Chou, C.-K., and Lee, S.-M. (2009). Relationship between central corneal thickness, refractive error, corneal curvature, anterior chamber depth and axial length. *Journal of the Chinese Medical Association*, 72(3):133–137.

Chen, Q., Fan, W., Niu, S., Shi, J., Shen, H., and Yuan, S. (2015). Automated choroid segmentation based on gradual intensity distance in hd-oct images. *Optics express*, 23(7):8974–8994.

Chen, X., Sankaridurg, P., Donovan, L., Lin, Z., Li, L., Martinez, A., Holden, B., and Ge, J. (2010). Characteristics of peripheral refractive errors of myopic and non-myopic chinese eyes. *Vision research*, 50(1):31–35.

Chen, X., Shi, F., and Chen, H. (2019). *Retinal Optical Coherence Tomography Image Analysis*. Springer.

Chen, Z., Xue, F., Zhou, J., Qu, X., and Zhou, X. (2016). Effects of orthokeratology on choroidal thickness and axial length. *Optometry and Vision Science*, 93(9):1064–1071.

Chiang, P. P.-C., Fenwick, E., Cheung, C. M. G., and Lamoureux, E. L. (2014). Public health impact of pathologic myopia. In *Pathologic Myopia*, pages 75–81. Springer.

Chiang, S. T.-H., Chen, T.-L., and Phillips, J. R. (2018). Effect of optical defocus on choroidal thickness in healthy adults with presbyopia. *Investigative Ophthalmology & Visual Science*, 59(12):5188–5193.

Chiang, S. T.-H., Phillips, J. R., and Backhouse, S. (2015). Effect of retinal image defocus on the thickness of the human choroid. *Ophthalmic and Physiological Optics*, 35(4):405–413.

Cho, A., Choi, Y., and Kim, Y. (2014). Influence of choroidal thickness on subfoveal choroidal thickness measurement repeatability using enhanced depth imaging optical coherence tomography. *Eye*, 28(10):1151–1160.

Chua, S. Y., Sabanayagam, C., Cheung, Y.-B., Chia, A., Valenzuela, R. K., Tan, D., Wong, T.-Y., Cheng, C.-Y., and Saw, S.-M. (2016). Age of onset of myopia predicts risk of high myopia in later childhood in myopic singapore children. *Ophthalmic and Physiological Optics*, 36(4):388–394.

Chung, S. E., Kang, S. W., Lee, J. H., and Kim, Y. T. (2011). Choroidal thickness in polypoidal choroidal vasculopathy and exudative age-related macular degeneration. *Ophthalmology*, 118(5):840–845.

Copete, S., Flores-Moreno, I., Montero, J. A., Duker, J. S., and Ruiz-Moreno, J. M. (2014). Direct comparison of spectral-domain and swept-source oct in the measurement of choroidal thickness in normal eyes. *British Journal of Ophthalmology*, 98(3):334–338.

Deng, J., Li, X., Jin, J., Zhang, B., Zhu, J., Zou, H., Xu, X., Xie, J., Wang, L., Zhu, S., et al. (2018). Distribution pattern of choroidal thickness at the posterior

pole in chinese children with myopia. *Investigative ophthalmology & visual science*, 59(3):1577–1586.

Dervişoğulları, M. S., Totan, Y., Yüce, A., and Kulak, A. E. (2016). Acute effects of caffeine on choroidal thickness and ocular pulse amplitude. *Cutaneous and ocular toxicology*, 35(4):281–286.

Diether, S. and Schaeffel, F. (1997). Local changes in eye growth induced by imposed local refractive error despite active accommodation. *Vision research*, 37(6):659–668.

Diez, P. S., Wahl, S., and Ohlendorf, A. (2019a). The standardized definition of high myopia. *Graefe's Archive for Clinical and Experimental Ophthalmology*, 257(8):1807–1808.

Diez, P. S., Yang, L.-H., Lu, M.-X., Wahl, S., and Ohlendorf, A. (2019b). Growth curves of myopia-related parameters to clinically monitor the refractive development in chinese schoolchildren. *Graefe's Archive for Clinical and Experimental Ophthalmology*, 257(5):1045–1053.

Ding, Y., Spund, B., Glazman, S., Shrier, E. M., Miri, S., Selesnick, I., and Bodis-Wollner, I. (2014). Application of an oct data-based mathematical model of the foveal pit in parkinson disease. *Journal of Neural Transmission*, 121(11):1367–1376.

Drexler, W. and Fujimoto, J. G. (2008). *Optical coherence tomography: technology and applications.* Springer Science & Business Media.

Dubis, A. M., McAllister, J. T., and Carroll, J. (2009). Reconstructing foveal pit morphology from optical coherence tomography imaging. *British Journal of Ophthalmology*, 93(9):1223–1227.

Dunne, M., Barnes, D., and Clement, R. (1987). A model for retinal shape changes in ametropia. *Ophthalmic and Physiological Optics*, 7(2):159–160.

Dunne, M. C. (1995). A computing scheme for determination of retinal contour from peripheral refraction, keratometry and a-scan ultrasonography. *Ophthalmic and Physiological Optics*, 15(2):133–143.

Early Treatment Diabetic Retinopathy Study Research Group (1985). Photocoagulation for diabetic macular edema. *Arch Ophthalmol*, 103:1796–1806.

Edwards, A. L. (1984). An introduction to linear regression and correlation. Technical report.

Fedtke, C., Ehrmann, K., and Holden, B. A. (2009). A review of peripheral refraction techniques. *Optometry and vision science*, 86(5):429–446.

Ferree, C. E., Rand, G., and Hardy, C. (1931). Refraction for the peripheral field of vision. *Archives of Ophthalmology*, 5(5):717–731.

Fitzgerald, M. E., Wildsoet, C. F., and Reiner, A. (2002). Temporal relationship of choroidal blood flow and thickness changes during recovery from form deprivation myopia in chicks. *Experimental eye research*, 74(5):561–570.

Flitcroft, D. (2012). The complex interactions of retinal, optical and environmental factors in myopia aetiology. *Progress in Retinal and Eye Research*, 31(6):622–660.

Flitcroft, D. I., Harb, E. N., and Wildsoet, C. F. (2020). The spatial frequency content of urban and indoor environments as a potential risk factor for myopia development. *Investigative Ophthalmology & Visual Science*, 61(11):42–42.

Fontaine, M., Gaucher, D., Sauer, A., and Speeg-Schatz, C. (2017). Choroidal thickness and ametropia in children: a longitudinal study. *European journal of ophthalmology*, 27(6):730–734.

Fujimoto, J. and Swanson, E. (2016). The development, commercialization, and impact of optical coherence tomography. *Investigative ophthalmology & visual science*, 57(9):OCT1–OCT13.

García, M. G., Wahl, S., Pusti, D., Artal, P., and Ohlendorf, A. (2019). 2-d peripheral image quality metrics with different types of multifocal contact lenses. *Scientific reports*, 9(1):1–10.

García García, M., Pusti, D., Wahl, S., and Ohlendorf, A. (2019). A global approach to describe retinal defocus patterns. *Plos one*, 14(4):e0213574.

Gekeler, F., Schaeffel, F., Howland, H. C., and Wattam-Bell, J. (1997). Measurement of astigmatism by automated infrared photoretinoscopy. *Optometry and vision science*, 74(7):472–482.

Goud, A., Singh, S. R., Sahoo, N. K., Rasheed, M. A., Vupparaboina, K. K., Ankireddy, S., Lupidi, M., and Chhablani, J. (2019). New insights on choroidal vascularity: A comprehensive topographic approach. *Investigative ophthalmology & visual science*, 60(10):3563–3569.

Grossniklaus, H. E. and Green, W. R. (1992). Pathologic findings in pathologic myopia. *Retina (Philadelphia, Pa.)*, 12(2):127–133.

Group, E. T. D. R. S. R. et al. (1985). Photocoagulation for diabetic macular edema. *Arch Ophthalmol*, 103:1796–1806.

Gupta, P., Jing, T., Marziliano, P., Cheung, C. Y., Baskaran, M., Lamoureux, E. L., Wong, T. Y., Cheung, C. M. G., and Cheng, C.-Y. (2015). Distribution and determinants of choroidal thickness and volume using automated segmentation software in a population-based study. *American Journal of Ophthalmology*, 159(2):293–301.

Gupta, P., Thakku, S. G., Saw, S.-M., Tan, M., Lim, E., Tan, M., Cheung, C. M. G., Wong, T.-Y., and Cheng, C.-Y. (2017). Characterization of choroidal morphologic and vascular features in young men with high myopia using spectral-domain optical coherence tomography. *American journal of ophthalmology*, 177:27–33.

Gustafsson, J., Terenius, E., Buchheister, J., and Unsbo, P. (2001). Peripheral astigmatism in emmetropic eyes. *Ophthalmic and Physiological Optics*, 21(5):393–400.

Hirata, M., Tsujikawa, A., Matsumoto, A., Hangai, M., Ooto, S., Yamashiro, K., Akiba, M., and Yoshimura, N. (2011). Macular choroidal thickness and volume in normal subjects measured by swept-source optical coherence tomography. *Investigative Ophthalmology & Visual Science*, 52(8):4971–4978.

Hogan, M. J. (1971). Histology of the human eye. *an Atlas and Textbook*.

Holden, B. A., Fricke, T. R., Wilson, D. A., Jong, M., Naidoo, K. S., Sankaridurg, P., Wong, T. Y., Naduvilath, T. J., and Resnikoff, S. (2016). Global prevalence of myopia and high myopia and temporal trends from 2000 through 2050. *Ophthalmology*, 123(5):1036–1042.

Hoseini-Yazdi, H., Vincent, S. J., Collins, M. J., and Read, S. A. (2019a). Regional alterations in human choroidal thickness in response to short-term monocular hemifield myopic defocus. *Ophthalmic and Physiological Optics*, 39(3):172–182.

Hoseini-Yazdi, H., Vincent, S. J., Collins, M. J., Read, S. A., and Alonso-Caneiro, D. (2019b). Repeatability of wide-field choroidal thickness measurements using enhanced-depth imaging optical coherence tomography. *Clinical and Experimental Optometry*, 102(3):327–334.

Hoseini-Yazdi, H., Vincent, S. J., Collins, M. J., Read, S. A., and Alonso-Caneiro, D. (2019c). Wide-field choroidal thickness in myopes and emmetropes. *Scientific reports*, 9(1):3474–3484.

Hoseini-Yazdi, H., Vincent, S. J., Read, S. A., and Collins, M. J. (2020). Astigmatic defocus leads to short-term changes in human choroidal thickness. *Investigative Ophthalmology & Visual Science*, 61(8):48–48.

86

Howlett, M. H. and McFadden, S. A. (2009). Spectacle lens compensation in the pigmented guinea pig. *Vision research*, 49(2):219–227.

Huang, D., Swanson, E. A., Lin, C. P., Schuman, J. S., Stinson, W. G., Chang, W., Hee, M. R., Flotte, T., Gregory, K., Puliafito, C. A., et al. (1991). Optical coherence tomography. *science*, 254(5035):1178–1181.

Huang, H.-M., Chang, D. S.-T., and Wu, P.-C. (2015). The association between near work activities and myopia in children—a systematic review and meta-analysis. *PloS one*, 10(10):e0140419.

Huang, J., Wen, D., Wang, Q., McAlinden, C., Flitcroft, I., Chen, H., Saw, S. M., Chen, H., Bao, F., Zhao, Y., et al. (2016). Efficacy comparison of 16 interventions for myopia control in children: a network meta-analysis. *Ophthalmology*, 123(4):697–708.

Hung, L.-F., Wallman, J., and Smith, E. L. (2000). Vision-dependent changes in the choroidal thickness of macaque monkeys. *Investigative Ophthalmology & Visual Science*, 41(6):1259–1269.

Ikuno, Y., Kawaguchi, K., Nouchi, T., and Yasuno, Y. (2010). Choroidal thickness in healthy japanese subjects. *Investigative Ophthalmology & Visual Science*, 51(4):2173–2176.

Iovino, C., Pellegrini, M., Bernabei, F., Borrelli, E., Sacconi, R., Govetto, A., Vagge, A., Di Zazzo, A., Forlini, M., Finocchio, L., et al. (2020). Choroidal vascularity index: An in-depth analysis of this novel optical coherence tomography parameter. *Journal of Clinical Medicine*, 9(2):595.

ISO / IEC Guide 100:2008 (2008). Evaluation of measurement data – Guide to the expression of uncertainty in measurement. Standard, International Organization for Standardization, Geneva, Switzerland.

Jin, P., Zou, H., Xu, X., Chang, T. C., Zhu, J., Deng, J., Lv, M., Jin, J., Sun, S., Wang, L., et al. (2019). Longitudinal changes in choroidal and retinal thicknesses in children with myopic shift. *Retina*, 39(6):1091–1099.

Jin, P., Zou, H., Zhu, J., Xu, X., Jin, J., Chang, T. C., Lu, L., Yuan, H., Sun, S., Yan, B., et al. (2016). Choroidal and retinal thickness in children with different refractive status measured by swept-source optical coherence tomography. *American journal of ophthalmology*, 168:164–176.

Kajikawa, J. (1923). Beiträge zur anatomie und physiologie des vogelauges. *Albrecht von Graefes Archiv für Ophthalmologie*, 112(2):260–346.

Kang, P., Fan, Y., Oh, K., Trac, K., Zhang, F., and Swarbrick, H. A. (2013). The effect of multifocal soft contact lenses on peripheral refraction. *Optometry and Vision Science*, 90(7):658–666.

Koeppen, B. M. and Stanton, B. A. (2009). *Berne & Levy Physiology, Updated Edition E-Book*. Elsevier Health Sciences.

Kolb, H. (2012). Simple anatomy of the retina. *Webvision: The Organization of the Retina and Visual System [Internet]*.

Kong, M., Choi, D. Y., Han, G., Song, Y.-M., Park, S. Y., Sung, J., Hwang, S., and Ham, D.-I. (2018). Measurable range of subfoveal choroidal thickness with conventional spectral domain optical coherence tomography. *Translational Vision Science & Technology*, 7(5):16–16.

Kong, M., Eo, D. R., Han, G., Park, S. Y., and Ham, D.-I. (2016). Error rate of automated choroidal segmentation using swept-source optical coherence tomography. *Acta Ophthalmologica*, 94(6):e427–e431.

Koumbo, I. O., Conrad, F., Sankaridurg, P., and Ehrmann, K. (2019). Peripheral eye length measurement techniques: a review. *Clinical & Experimental Optometry*.

Kugelman, J., Alonso-Caneiro, D., Read, S. A., Hamwood, J., Vincent, S. J., Chen, F. K., and Collins, M. J. (2019). Automatic choroidal segmentation in oct images using supervised deep learning methods. *Scientific reports*, 9(1):1–13.

Kuo, A. N., McNabb, R. P., Chiu, S. J., El-Dairi, M. A., Farsiu, S., Toth, C. A., and Izatt, J. A. (2013). Correction of ocular shape in retinal optical coherence tomography and effect on current clinical measures. *American Journal of Ophthalmology*, 156(2):304–311.

Kuo, A. N., Verkicharla, P. K., McNabb, R. P., Cheung, C. Y., Hilal, S., Farsiu, S., Chen, C., Wong, T. Y., Ikram, M. K., Cheng, C. Y., et al. (2016). Posterior eye shape measurement with retinal oct compared to mri. *Investigative Ophthalmology & Visual Science*, 57(9):196–203.

Lake, S., Bottema, M., Williams, K., and Reynolds, K. (2019). The correlation between optical coherence tomography retinal shape irregularity and axial length. *PloS One*, 14(12).

Lan, W., Lin, Z., Yang, Z., and Artal, P. (2019). Two-dimensional peripheral refraction and retinal image quality in emmetropic children. *Scientific reports*, 9(1):1–9.

Lee, K., Lee, J., Lee, C. S., Park, S. Y., Lee, S. C., and Lee, T. (2015). Topographical variation of macular choroidal thickness with myopia. *Acta ophthalmologica*, 93(6):e469–e474.

Lee, S. W., Yu, S.-Y., Seo, K. H., Kim, E. S., and Kwak, H. W. (2014). Diurnal variation in choroidal thickness in relation to sex, axial length, and baseline choroidal thickness in healthy korean subjects. *Retina*, 34(2):385–393.

Lens, A., Nemeth, S. C., and Ledford, J. K. (2008). *Ocular anatomy and physiology*. Slack Incorporated.

Li, T., Zhou, X., Wang, Z., Zhu, J., Shen, W., and Jiang, B. (2016). Assessment of retinal and choroidal measurements in chinese school-age children with cirrus-hd optical coherence tomography. *PloS One*, 11(7):e0158948.

Li, X. Q., Larsen, M., and Munch, I. C. (2011). Subfoveal choroidal thickness in relation to sex and axial length in 93 danish university students. *Investigative Ophthalmology & Visual Science*, 52(11):8438–8441.

Li, Z., Cui, D., Hu, Y., Ao, S., Zeng, J., and Yang, X. (2017). Choroidal thickness and axial length changes in myopic children treated with orthokeratology. *Contact Lens and Anterior Eye*, 40(6):417–423.

Li, Z., Hu, Y., Cui, D., Long, W., He, M., and Yang, X. (2019). Change in subfoveal choroidal thickness secondary to orthokeratology and its cessation: a predictor for the change in axial length. *Acta ophthalmologica*, 97(3):e454–e459.

Li, Z., Long, W., Hu, Y., Zhao, W., Zhang, W., and Yang, X. (2020). Features of the choroidal structures in myopic children based on image binarization of optical coherence tomography. *Investigative Ophthalmology & Visual Science*, 61(4):18–18.

Lilliefors, H. W. (1967). On the kolmogorov-smirnov test for normality with mean and variance unknown. *Journal of the American statistical Association*, 62(318):399–402.

Lin, Z., Vasudevan, B., Jhanji, V., Mao, G. Y., Gao, T. Y., Wang, F. H., Rong, S. S., Ciuffreda, K. J., and Liang, Y. B. (2014). Near work, outdoor activity, and their association with refractive error. *Optometry and Vision Science*, 91(4):376–382.

Lingham, G., Mackey, D. A., Lucas, R., and Yazar, S. (2020). How does spending time outdoors protect against myopia? a review. *British Journal of Ophthalmology*, 104(5):593–599.

Liu, L., Marsh-Tootle, W., Harb, E. N., Hou, W., Zhang, Q., Anderson, H. A., Norton, T. T., Weise, K. K., Gwiazda, J. E., Hyman, L., et al. (2016). A sloped piecemeal gaussian model for characterising foveal pit shape. *Ophthalmic and Physiological Optics*, 36(6):615–631.

Liu, Y., Wang, L., Xu, Y., Pang, Z., and Mu, G. (2021). The influence of the choroid on the onset and development of myopia: from perspectives of choroidal thickness and blood flow. *Acta ophthalmologica*.

Logan, N. S., Gilmartin, B., Wildsoet, C. F., and Dunne, M. C. (2004). Posterior retinal contour in adult human anisomyopia. *Investigative ophthalmology & visual science*, 45(7):2152–2162.

Lotmar, W. and Lotmar, T. (1974). Peripheral astigmatism in the human eye: experimental data and theoretical model predictions. *JOSA*, 64(4):510–513.

Lundström, L. and Rosén, R. (2017). Peripheral aberrations. In Artal, P., editor, *Handbook of Visual Optics*. CRC Press, London.

Mansouri, K., Medeiros, F. A., Tatham, A. J., Marchase, N., and Weinreb, R. N. (2014). Evaluation of retinal and choroidal thickness by swept-source optical coherence tomography: repeatability and assessment of artifacts. *American Journal of Ophthalmology*, 157(5):1022–1032.

Martinez-Conde, S., Macknik, S. L., Troncoso, X. G., and Hubel, D. H. (2009). Microsaccades: a neurophysiological analysis. *Trends in Neurosciences*, 32(9):463–475.

Maruko, I., Iida, T., Sugano, Y., Ojima, A., Ogasawara, M., and Spaide, R. F. (2010). Subfoveal choroidal thickness after treatment of central serous chorioretinopathy. *Ophthalmology*, 117(9):1792–1799.

Maruko, I., Iida, T., Sugano, Y., Oyamada, H., Sekiryu, T., Fujiwara, T., and Spaide, R. F. (2011). Subfoveal choroidal thickness after treatment of vogt–koyanagi–harada disease. *Retina*, 31(3):510–517.

Mazzaferri, J., Beaton, L., Hounye, G., Sayah, D. N., and Costantino, S. (2017). Opensource algorithm for automatic choroid segmentation of oct volume reconstructions. *Scientific Reports*, 7:42112.

McAlinden, C., Khadka, J., and Pesudovs, K. (2011). Statistical methods for conducting agreement (comparison of clinical tests) and precision (repeatability or reproducibility) studies in optometry and ophthalmology. *Ophthalmic and Physiological Optics*, 31(4):330–338.

Meng, W., Butterworth, J., Malecaze, F., and Calvas, P. (2011). Axial length of myopia: a review of current research. *Ophthalmologica*, 225(3):127–134.

Metlapally, R. and Wildsoet, C. F. (2015). Scleral mechanisms underlying ocular growth and myopia. *Progress in molecular biology and translational science*, 134:241–248.

Millodot, M. (1981). Effect of ametropia on peripheral refraction. *American journal of optometry and physiological optics*, 58(9):691–695.

Minami, S., Ito, Y., Ueno, S., Kataoka, K., Takeuchi, J., Ito, H., Nakano, Y., Kitagawa, M., Leahy, C., Straub, J., et al. (2020). Analysis of macular curvature in normal eyes using swept-source optical coherence tomography. *Japanese Journal of Ophthalmology*, 64(2):180–186.

Miyake, M., Yamashiro, K., Akagi-Kurashige, Y., Oishi, A., Tsujikawa, A., Hangai, M., and Yoshimura, N. (2014). Analysis of fundus shape in highly myopic eyes by using curvature maps constructed from optical coherence tomography. *PloS One*, 9(9).

Mohler, K. J., Draxinger, W., Klein, T., Kolb, J. P., Wieser, W., Haritoglou, C., Kampik, A., Fujimoto, J. G., Neubauer, A. S., Huber, R., et al. (2015). Combined 60 wide-field choroidal thickness maps and high-definition en face vasculature visualization using swept-source megahertz oct at 1050 nm. *Investigative ophthalmology & visual science*, 56(11):6284–6293.

Morgan, I. G., Ashby, R. S., and Nickla, D. L. (2013). Form deprivation and lens-induced myopia: are they different? *Ophthalmic and Physiological Optics*, 33(3):355–361.

Moriyama, M., Ohno-Matsui, K., Futagami, S., Yoshida, T., Hayashi, K., Shimada, N., Kojima, A., Tokoro, T., and Mochizuki, M. (2007). Morphology and long-term changes of choroidal vascular structure in highly myopic eyes with and without posterior staphyloma. *Ophthalmology*, 114(9):1755–1762.

Mutti, D. O., Mitchell, G. L., Moeschberger, M. L., Jones, L. A., and Zadnik, K. (2002). Parental myopia, near work, school achievement, and children's refractive error. *Investigative ophthalmology & visual science*, 43(12):3633–3640.

Mutti, D. O., Sholtz, R. I., Friedman, N. E., and Zadnik, K. (2000). Peripheral refraction and ocular shape in children. *Investigative ophthalmology & visual science*, 41(5):1022–1030.

Mutti, D. O., Sinnott, L. T., Mitchell, G. L., Jones-Jordan, L. A., Moeschberger, M. L., Cotter, S. A., Kleinstein, R. N., Manny, R. E., Twelker, J. D., and Zadnik, K. (2011). Relative peripheral refractive error and the risk of onset and progression of myopia in children. *Investigative ophthalmology & visual science*, 52(1):199–205.

Myers, L. and Sirois, M. J. (2004). Differences between spearman correlation coefficients. *Encyclopedia of statistical sciences*, 12.

Neil Charman, W. and Radhakrishnan, H. (2010). Peripheral refraction and the development of refractive error: a review. *Ophthalmic and Physiological Optics*, 30(4):321–338.

Niblack, W. (2003). An introduction to digital image processing. 1986. In *G. Leedham, C. Yan, K. Takru, J. Tan and L. Mian. Comparison of Some Thresholding Algorithms for Text/Background Segmentation in Difficult Document Images. In Proceedings of the Seventh International Conference on Document Analysis and Recognition*, pages 859–864.

Nickla, D. L. and Totonelly, K. (2015). Choroidal thickness predicts ocular growth in normal chicks but not in eyes with experimentally altered growth. *Clinical and Experimental Optometry*, 98(6):564–570.

Nickla, D. L. and Wallman, J. (2010). The multifunctional choroid. *Progress in retinal and eye research*, 29(2):144–168.

Nolan, J. M., Stringham, J. M., Beatty, S., and Snodderly, D. M. (2008). Spatial profile of macular pigment and its relationship to foveal architecture. *Investigative Ophthalmology & Visual Science*, 49(5):2134–2142.

North, R. and Kelly, M. (1987). A review of the uses and adverse effects of topical administration of atropine. *Ophthalmic and Physiological Optics*, 7(2):109–114.

Norton, T. T., Casagrande, V. A., and Sherman, S. M. (1977). Loss of y-cells in the lateral geniculate nucleus of monocularly deprived tree shrews. *Science*, 197(4305):784–786.

Ogawa, A. and Tanaka, M. (1988). The relationship between refractive errors and retinal detachment–analysis of 1,166 retinal detachment cases. *Japanese Journal of Ophthalmology*, 32(3):310–315.

Ohlendorf, A. and Schaeffel, F. (2009). Contrast adaptation induced by defocus–a possible error signal for emmetropization? *Vision Research*, 49(2):249–256.

Pacella, R., McLellan, J., Grice, K., Del Bono, E. A., Wiggs, J. L., and Gwiazda, J. E. (1999). Role of genetic factors in the etiology of juvenile-onset myopia based on a longitudinal study of refractive error. *Optometry and vision science: official publication of the American Academy of Optometry*, 76(6):381–386.

Pan, C.-W., Ramamurthy, D., and Saw, S.-M. (2012). Worldwide prevalence and risk factors for myopia. *Ophthalmic and Physiological Optics*, 32(1):3–16.

Pärssinen, O. and Lyyra, A.-L. (1993). Myopia and myopic progression among school-children: a three-year follow-up study. *Investigative ophthalmology & visual science*, 34(9):2794–2802.

Philip, K., Sankaridurg, P., Holden, B., Ho, A., and Mitchell, P. (2014). Influence of higher order aberrations and retinal image quality in myopisation of emmetropic eyes. *Vision research*, 105:233–243.

Queirós, A., Amorim-de Sousa, A., Lopes-Ferreira, D., Villa-Collar, C., Gutiérrez, Á. R., and González-Méijome, J. M. (2018). Relative peripheral refraction across 4 meridians after orthokeratology and lasik surgery. *Eye and Vision*, 5(1):1–8.

Queirós, A., González-Méijome, J. M., Jorge, J., Villa-Collar, C., and Gutiérrez, A. R. (2010). Peripheral refraction in myopic patients after orthokeratology. *Optometry and Vision Science*, 87(5):323–329.

Queirós, A., Villa-Collar, C., Jorge, J., Gutiérrez, Á. R., and González-Méijome, J. M. (2012). Peripheral refraction in myopic eyes after lasik surgery. *Optometry and Vision Science*, 89(7):977–983.

Radhakrishnan, H., Pardhan, S., Calver, R. I., and O'Leary, D. J. (2004). Effect of positive and negative defocus on contrast sensitivity in myopes and non-myopes. *Vision Research*, 44(16):1869–1878.

Rahman, W., Chen, F. K., Yeoh, J., Patel, P., Tufail, A., and Da Cruz, L. (2011). Repeatability of manual subfoveal choroidal thickness measurements in healthy subjects using the technique of enhanced depth imaging optical coherence tomography. *Investigative Ophthalmology & Visual Science*, 52(5):2267–2271.

Rasheed, M. A., Singh, S. R., Invernizzi, A., Cagini, C., Goud, A., Sahoo, N. K., Cozzi, M., Lupidi, M., and Chhablani, J. (2018). Wide-field choroidal thickness profile in healthy eyes. *Scientific reports*, 8(1):1–7.

Raviola, E. and Wiesel, T. N. (1985). An animal model of myopia. *New England Journal of Medicine*, 312(25):1609–1615.

Read, S. A., Alonso-Caneiro, D., Vincent, S. J., and Collins, M. J. (2015). Longitudinal changes in choroidal thickness and eye growth in childhood. *Investigative ophthalmology & visual science*, 56(5):3103–3112.

Read, S. A., Collins, M. J., and Sander, B. P. (2010). Human optical axial length and defocus. *Investigative Ophthalmology & Visual Science*, 51(12):6262–6269.

Read, S. A., Collins, M. J., Vincent, S. J., and Alonso-Caneiro, D. (2013). Choroidal thickness in myopic and nonmyopic children assessed with enhanced depth imaging optical coherence tomography. *Investigative Ophthalmology & Visual Science*, 54(12):7578–7586.

Read, S. A., Fuss, J. A., Vincent, S. J., Collins, M. J., and Alonso-Caneiro, D. (2019a). Choroidal changes in human myopia: insights from optical coherence tomography imaging. *Clinical and Experimental Optometry*, 102(3):270–285.

Read, S. A., Fuss, J. A., Vincent, S. J., Collins, M. J., and Alonso-Caneiro, D. (2019b). Choroidal changes in human myopia: insights from optical coherence tomography imaging. *Clinical and Experimental Optometry*, 102(3):270–285.

Read, S. A., Pieterse, E. C., Alonso-Caneiro, D., Bormann, R., Hong, S., Lo, C.-H., Richer, R., Syed, A., and Tran, L. (2018). Daily morning light therapy is associated with an increase in choroidal thickness in healthy young adults. *Scientific reports*, 8(1):1–10.

Remington, L. A. and Goodwin, D. (2011). *Clinical anatomy of the visual system E-Book*. Elsevier Health Sciences.

Rempt, F., Hoogerheide, J., and Hoogenboom, W. (1971). Peripheral retinoscopy and the skiagram. *Ophthalmologica*, 162(1):1–10.

Rucker, F. J. (2013). The role of luminance and chromatic cues in emmetropisation. *Ophthalmic and Physiological Optics*, 33(3):196–214.

Rucker, F. J. and Wallman, J. (2012). Chicks use changes in luminance and chromatic contrast as indicators of the sign of defocus. *Journal of vision*, 12(6):23–23.

Sanchez-Cano, A., Orduna, E., Segura, F., Lopez, C., Cuenca, N., Abecia, E., and Pinilla, I. (2014). Choroidal thickness and volume in healthy young white adults and the relationships between them and axial length, ammetropy and sex. *American Journal of Ophthalmology*, 158(3):574–583.

Saw, S.-M., Gazzard, G., Shih-Yen, E. C., and Chua, W.-H. (2005). Myopia and associated pathological complications. *Ophthalmic and Physiological Optics*, 25(5):381–391.

Saw, S.-M., Nieto, F. J., Katz, J., Schein, O. D., Levy, B., and Chew, S.-J. (2000). Factors related to the progression of myopia in singaporean children. *Optometry and vision science*, 77(10):549–554.

Schaeffel, F., Glasser, A., and Howland, H. C. (1988). Accommodation, refractive error and eye growth in chickens. *Vision research*, 28(5):639–657.

Scheibe, P., Zocher, M. T., Francke, M., and Rauscher, F. G. (2016). Analysis of foveal characteristics and their asymmetries in the normal population. *Experimental Eye Research*, 148:1–11.

Schmid, G. F. (2003). Variability of retinal steepness at the posterior pole in children 7–15 years of age. *Current Eye Research*, 27(1):61–68.

Schmid, G. F. (2011). Association between retinal steepness and central myopic shift in children. *Optometry and Vision Science*, 88(6):684–690.

Schmid, K. L. and Wildsoe, C. F. (1997). Contrast and spatial-frequency requirements for emmetropization in chicks. *Vision research*, 37(15):2011–2021.

Schwiegerling, J. (2004). Arizona eye model. In *Field Guide to Visual and Ophthalmic Optics*. Spie Bellingham WA.

Seidel, G., Hausberger, S., Herzog, S. A., Palkovits, S., Pöschl, E. M., Wackernagel, W., and Weger, M. (2015). Circadian macular volume changes in the healthy human choroid. *American journal of ophthalmology*, 159(2):365–371.

Seidemann, A. and Schaeffel, F. (2002). Effects of longitudinal chromatic aberration on accommodation and emmetropization. *Vision research*, 42(21):2409–2417.

Seidemann, A., Schaeffel, F., Guirao, A., Lopez-Gil, N., and Artal, P. (2002). Peripheral refractive errors in myopic, emmetropic, and hyperopic young subjects. *JOSA A*, 19(12):2363–2373.

Shao, L., Xu, L., Chen, C. X., Yang, L. H., Du, K. F., Wang, S., Zhou, J. Q., Wang, Y. X., You, Q. S., Jonas, J. B., et al. (2013). Reproducibility of subfoveal choroidal thickness measurements with enhanced depth imaging by spectral-domain optical coherence tomography. *Investigative Ophthalmology & Visual Science*, 54(1):230–233.

Shih, Y.-F. (1998). Relationship between choroidal blood flow and myopia. In *Myopia Updates*, pages 297–303. Springer.

Shrout, P. E. and Fleiss, J. L. (1979). Intraclass correlations: uses in assessing rater reliability. *Psychological Bulletin*, 86(2):420–428.

Siegwart Jr, J. T. and Norton, T. T. (1998). The susceptible period for deprivation-induced myopia in tree shrew. *Vision research*, 38(22):3505–3515.

Siegwart Jr, J. T. and Norton, T. T. (2010). Binocular lens treatment in tree shrews: Effect of age and comparison of plus lens wear with recovery from minus lens-induced myopia. *Experimental eye research*, 91(5):660–669.

Singh, S. R., Invernizzi, A., Rasheed, M. A., Cagini, C., Goud, A., Vupparaboina, K. K., Cozzi, M., Lupidi, M., and Chhablani, J. (2018). Wide-field choroidal vascularity in healthy eyes. *American journal of ophthalmology*, 193:100–105.

Smith, E. L., Ramamirtham, R., Qiao-Grider, Y., Hung, L.-F., Huang, J., Kee, C.-s., Coats, D., and Paysse, E. (2007). Effects of foveal ablation on emmetropization and form-deprivation myopia. *Investigative ophthalmology & visual science*, 48(9):3914–3922.

Smith III, E. L., Hung, L.-F., and Huang, J. (2009). Relative peripheral hyperopic defocus alters central refractive development in infant monkeys. *Vision research*, 49(19):2386–2392.

Sng, C. C., Lin, X.-Y., Gazzard, G., Chang, B., Dirani, M., Chia, A., Selvaraj, P., Ian, K., Drobe, B., Wong, T.-Y., et al. (2011). Peripheral refraction and refractive error in singapore chinese children. *Investigative ophthalmology & visual science*, 52(2):1181–1190.

Sonoda, S., Sakamoto, T., Yamashita, T., Shirasawa, M., Uchino, E., Terasaki, H., and Tomita, M. (2014). Choroidal structure in normal eyes and after photodynamic therapy determined by binarization of optical coherence tomographic images. *Investigative ophthalmology & visual science*, 55(6):3893–3899.

Sonoda, S., Sakamoto, T., Yamashita, T., Uchino, E., Kawano, H., Yoshihara, N., Terasaki, H., Shirasawa, M., Tomita, M., and Ishibashi, T. (2015). Luminal and stromal areas of choroid determined by binarization method of optical coherence tomographic images. *American journal of ophthalmology*, 159(6):1123–1131.

Spaide, R. F., Ohno-Matsui, K., Yannuzzi, L. A., et al. (2014). Pathologic myopia.

Steidle, M. A. and Straub, J. (2018). Estimating the shape of the human eye using widefield optical coherence tomography (oct). In *Biophotonics: Photonic Solutions for Better Health Care VI*, volume 10685, page 106851V. International Society for Optics and Photonics.

Swiatczak, B. and Schaeffel, F. (2021). Emmetropic, but not myopic human eyes distinguish positive defocus from calculated blur. *Investigative Ophthalmology & Visual Science*, 62(3):14–14.

Tabernero, J., Ohlendorf, A., Fischer, M. D., Bruckmann, A. R., Schiefer, U., and Schaeffel, F. (2011). Peripheral refraction profiles in subjects with low foveal refractive errors. *Optometry and Vision Science*, 88(3):E388–E394.

Tabernero, J. and Schaeffel, F. (2009a). Fast scanning photoretinoscope for measuring peripheral refraction as a function of accommodation. *JOSA A*, 26(10):2206–2210.

Tabernero, J. and Schaeffel, F. (2009b). More irregular eye shape in low myopia than in emmetropia. *Investigative Ophthalmology & Visual Science*, 50(9):4516–4522.

Tan, C. S. and Cheong, K. X. (2014). Macular choroidal thicknesses in healthy adults—relationship with ocular and demographic factors. *Investigative ophthalmology & visual science*, 55(10):6452–6458.

Tan, C. S., Ouyang, Y., Ruiz, H., and Sadda, S. R. (2012). Diurnal variation of choroidal thickness in normal, healthy subjects measured by spectral domain optical coherence tomography. *Investigative ophthalmology & visual science*, 53(1):261–266.

Tan, K.-A., Laude, A., Yip, V., Loo, E., Wong, E. P., and Agrawal, R. (2016). Choroidal vascularity index–a novel optical coherence tomography parameter for disease monitoring in diabetes mellitus? *Acta ophthalmologica*, 94(7):e612–e616.

Tan, R., Agrawal, R., Taduru, S., Gupta, A., Vupparaboina, K., and Chhablani, J. (2018). Choroidal vascularity index in retinitis pigmentosa: an oct study. *Ophthalmic Surgery, Lasers and Imaging Retina*, 49(3):191–197.

Terry, L., Cassels, N., Lu, K., Acton, J. H., Margrain, T. H., North, R. V., Fergusson, J., White, N., and Wood, A. (2016). Automated retinal layer segmentation using spectral domain optical coherence tomography: evaluation of inter-session repeatability and agreement between devices. *PloS one*, 11(9).

Tick, S., Rossant, F., Ghorbel, I., Gaudric, A., Sahel, J.-A., Chaumet-Riffaud, P., and Paques, M. (2011). Foveal shape and structure in a normal population. *Investigative Ophthalmology & Visual Science*, 52(8):5105–5110.

Tran, N., Chiu, S., Tian, Y., and Wildsoet, C. F. (2008). The significance of retinal image contrast and spatial frequency composition for eye growth modulation in young chicks. *Vision research*, 48(15):1655–1662.

Troilo, D., Smith, E. L., Nickla, D. L., Ashby, R., Tkatchenko, A. V., Ostrin, L. A., Gawne, T. J., Pardue, M. T., Summers, J. A., Kee, C.-s., et al. (2019). Imi–report on experimental models of emmetropization and myopia. *Investigative ophthalmology & visual science*, 60(3):M31–M88.

Twa, M. D., Schulle, K. L., Chiu, S. J., Farsiu, S., and Berntsen, D. A. (2016). Validation of macular choroidal thickness measurements from automated sd-oct image segmentation. *Optometry and Vision Science*, 93(11):1387–1398.

Usui, S., Ikuno, Y., Akiba, M., Maruko, I., Sekiryu, T., Nishida, K., and Iida, T. (2012). Circadian changes in subfoveal choroidal thickness and the relationship with circulatory factors in healthy subjects. *Investigative ophthalmology & visual science*, 53(4):2300–2307.

Verkicharla, P. K., Kammari, P., and Das, A. V. (2020). Myopia progression varies with age and severity of myopia. *Plos one*, 15(11):e0241759.

Verkicharla, P. K., Mathur, A., Mallen, E. A., Pope, J. M., and Atchison, D. A. (2012). Eye shape and retinal shape, and their relation to peripheral refraction. *Ophthalmic and Physiological Optics*, 32(3):184–199.

Verkicharla, P. K., Suheimat, M., Pope, J. M., Sepehrband, F., Mathur, A., Schmid, K. L., and Atchison, D. A. (2015). Validation of a partial coherence interferometry method for estimating retinal shape. *Biomedical Optics Express*, 6(9):3235–3247.

Verkicharla, P. K., Suheimat, M., Schmid, K. L., and Atchison, D. A. (2016). Peripheral refraction, peripheral eye length, and retinal shape in myopia. *Optometry and Vision Science*, 93(9):1072–1078.

Vongphanit, J., Mitchell, P., and Wang, J. J. (2002). Prevalence and progression of myopic retinopathy in an older population. *Ophthalmology*, 109(4):704–711.

Vuong, V. S., Moisseiev, E., Cunefare, D., Farsiu, S., Moshiri, A., and Yiu, G. (2016). Repeatability of choroidal thickness measurements on enhanced depth imaging optical coherence tomography using different posterior boundaries. *American Journal of Ophthalmology*, 169:104–112.

Wagner-Schuman, M., Dubis, A. M., Nordgren, R. N., Lei, Y., Odell, D., Chiao, H., Weh, E., Fischer, W., Sulai, Y., Dubra, A., et al. (2011). Race-and sex-related differences in retinal thickness and foveal pit morphology. *Investigative Ophthalmology & Visual Science*, 52(1):625–634.

Wakabayashi, T. and Ikuno, Y. (2010). Choroidal filling delay in choroidal neovascularisation due to pathological myopia. *British Journal of Ophthalmology*, 94(5):611–615.

Wallman, J., Gottlieb, M. D., Rajaram, V., and Fugate-Wentzek, L. A. (1987). Local retinal regions control local eye growth and myopia. *Science*, 237(4810):73–77.

Wallman, J., Turkel, J., and Trachtman, J. (1978). Extreme myopia produced by modest change in early visual experience. *Science*, 201(4362):1249–1251.

Wallman, J., Wildsoet, C., Xu, A., Gottlieb, M. D., Nickla, D. L., Marran, L., Krebs, W., and Christensen, A. M. (1995). Moving the retina: choroidal modulation of refractive state. *Vision Research*, 35(1):37–50.

Wallman, J. and Winawer, J. (2004). Homeostasis of eye growth and the question of myopia. *Neuron*, 43(4):447–468.

Walls, G. L. (1944). The vertebrate eye and its adaptive radiation.

Wang, D., Chun, R. K. M., Liu, M., Lee, R. P. K., Sun, Y., Zhang, T., Lam, C., Liu, Q., and To, C. H. (2016). Optical defocus rapidly changes choroidal thickness in schoolchildren. *PloS One*, 11(8):e0161535.

Wang, S., Lin, Z., Xi, X., Lu, Y., Pan, L., Li, X., Artal, P., Lan, W., and Yang, Z. (2020). Two-dimensional, high-resolution peripheral refraction in adults with isomyopia and anisomyopia. *Investigative Ophthalmology & Visual Science*, 61(6):16–16.

Wei, W. B., Xu, L., Jonas, J. B., Shao, L., Du, K. F., Wang, S., Chen, C. X., Xu, J., Wang, Y. X., Zhou, J. Q., et al. (2013). Subfoveal choroidal thickness: the beijing eye study. *Ophthalmology*, 120(1):175–180.

Wei, X., Ting, D. S. W., Ng, W. Y., Khandelwal, N., Agrawal, R., and Cheung, C. M. G. (2017). Choroidal vascularity index: a novel optical coherence tomography based parameter in patients with exudative age-related macular degeneration. *Retina*, 37(6):1120–1125.

Wildsoet, C. and Wallman, J. (1995). Choroidal and scleral mechanisms of compensation for spectacle lenses in chicks. *Vision research*, 35(9):1175–1194.

Wildsoet, C. F., Chia, A., Cho, P., Guggenheim, J. A., Polling, J. R., Read, S., Sankaridurg, P., Saw, S.-M., Trier, K., Walline, J. J., et al. (2019). Imi–interventions for controlling myopia onset and progression report. *Investigative ophthalmology & visual science*, 60(3):M106–M131.

Wildsoet, C. F., Howland, H. C., Falconer, S., and Dick, K. (1993). Chromatic aberration and accommodation: their role in emmetropization in the chick. *Vision research*, 33(12):1593–1603.

Wolffsohn, J. S., Kollbaum, P. S., Berntsen, D. A., Atchison, D. A., Benavente, A., Bradley, A., Buckhurst, H., Collins, M., Fujikado, T., Hiraoka, T., et al. (2019). Imi–clinical myopia control trials and instrumentation report. *Investigative ophthalmology & visual science*, 60(3):M132–M160.

Woodman, E. C., Read, S. A., and Collins, M. J. (2012). Axial length and choroidal thickness changes accompanying prolonged accommodation in myopes and emmetropes. *Vision research*, 72:34–41.

Woodman-Pieterse, E. C., Read, S. A., Collins, M. J., and Alonso-Caneiro, D. (2015). Regional changes in choroidal thickness associated with accommodation. *Investigative ophthalmology & visual science*, 56(11):6414–6422.

Woods, R. L., Bradley, A., and Atchison, D. A. (1996). Monocular diplopia caused by ocular aberrations and hyperopic defocus. *Vision Research*, 36(22):3597–3606.

Wu, H., Chen, W., Zhao, F., Zhou, Q., Reinach, P. S., Deng, L., Ma, L., Luo, S., Srinivasalu, N., Pan, M., et al. (2018). Scleral hypoxia is a target for myopia control. *Proceedings of the National Academy of Sciences*, 115(30):E7091–E7100.

Xiong, S., Sankaridurg, P., Naduvilath, T., Zang, J., Zou, H., Zhu, J., Lv, M., He, X., and Xu, X. (2017). Time spent in outdoor activities in relation to myopia prevention and control: a meta-analysis and systematic review. *Acta ophthalmologica*, 95(6):551–566.

Yamashita, T., Yamashita, T., Shirasawa, M., Arimura, N., Terasaki, H., and Sakamoto, T. (2012). Repeatability and reproducibility of subfoveal choroidal thickness in normal eyes of japanese using different sd-oct devices. *Investigative Ophthalmology & Visual Science*, 53(3):1102–1107.

Yang, Y. S. and Koh, J. W. (2015). Choroidal blood flow change in eyes with high myopia. *Korean journal of ophthalmology: KJO*, 29(5):309.

Ye, L., Shi, Y., Yin, Y., Li, S., He, J., Zhu, J., and Xu, X. (2020). Effects of atropine treatment on choroidal thickness in myopic children. *Investigative ophthalmology & visual science*, 61(14):15–15.

Zengin, M. O., Cinar, E., Karahan, E., Tuncer, I., and Kucukerdonmez, C. (2015). The effect of caffeine on choroidal thickness in young healthy subjects. *Cutaneous and ocular toxicology*, 34(2):112–116.

Zengin, M. O., Cinar, E., and Kucukerdonmez, C. (2014). The effect of nicotine on choroidal thickness. *British Journal of Ophthalmology*, 98(2):233–237.

Zhang, S., Zhang, G., Zhou, X., Xu, R., Wang, S., Guan, Z., Lu, J., Srinivasalu, N., Shen, M., Jin, Z., et al. (2019). Changes in choroidal thickness and choroidal blood perfusion in guinea pig myopia. *Investigative ophthalmology & visual science*, 60(8):3074–3083.

Zhang, Y. and Wildsoet, C. F. (2015). Rpe and choroid mechanisms underlying ocular growth and myopia. *Progress in molecular biology and translational science*, 134:221–240.

Zhang, Z., Zhou, Y., Xie, Z., Chen, T., Gu, Y., Lu, S., and Wu, Z. (2016). The effect of topical atropine on the choroidal thickness of healthy children. *Scientific reports*, 6(1):1–8.

Zhao, W., Li, Z., Hu, Y., Jiang, J., Long, W., Cui, D., Chen, W., and Yang, X. (2020). Short-term effects of atropine combined with orthokeratology (aco) on choroidal thickness. *Contact Lens and Anterior Eye.*

Zheng, F., Gregori, G., Schaal, K. B., Legarreta, A. D., Miller, A. R., Roisman, L., Feuer, W. J., and Rosenfeld, P. J. (2016). Choroidal thickness and choroidal vessel density in nonexudative age-related macular degeneration using swept-source optical coherence tomography imaging. *Investigative Ophthalmology & Visual Science*, 57(14):6256–6264.

Zheng, F., Wong, C.-W., Sabanayagam, C., Cheung, Y.-B., Matsumura, S., Chua, J., Man, R. E. K., Ohno-Matsui, K., Wong, T.-Y., Cheng, C.-Y., et al. (2020). Prevalence, risk factors and impact of posterior staphyloma diagnosed from wide-field optical coherence tomography in singapore adults with high myopia. *Acta ophthalmologica.*

Zhu, X. (2013). Temporal integration of visual signals in lens compensation (a review). *Experimental eye research*, 114:69–76.

Zhu, X., Park, T. W., Winawer, J., and Wallman, J. (2005). In a matter of minutes, the eye can know which way to grow. *Investigative Ophthalmology & Visual Science*, 46(7):2238–2241.

Zwillinger, D. and Kokoska, S. (1999). *CRC standard probability and statistics tables and formulae*, chapter Numerical summary measures, page 17. Crc Press.

10 Publications, conference contributions and talks related to this work

10.1 Peer reviewed publications

Breher K., García García M., Ohlendorf A., & Wahl S. (2018). The effect of the optical design of multifocal contact lenses on choroidal thickness. PLoS One, 13(11):-e0207637.

Breher K., Agarwala R., Leube A., & Wahl S. (2019). Direct modeling of foveal pit morphology from distortion-corrected OCT images. Biomedical Optics Express, 10(9):4815-4824.

García García M., **Breher K.**, Ohlendorf A., & Wahl S. (2020). To correct or not correct? Actual evidence, controversy and the questions that remain open. Journal of Clinical Medicine, 9(6):1975.

Neumann, A., **Breher, K.**, & Wahl, S. (2021). Effects of screen-based retinal light stimulation measured with a novel contrast sensitivity test. Plos one, 16(7), e0254877.

10.2 Peer reviewed conference contributions

Breher K., Ohlendorf A., & Wahl S. (2019). A metrological approach to the analysis of choroidal thickness by OCT in the context of myopia research. Investigative Ophthalmology & Visual Science, 60(9), 4334-4334. ARVO, Vancouver (Canada).

Breher K., Ohlendorf A., & Wahl S. (2019). A metrological approach to the analysis of choroidal thickness by OCT in the context of myopia research. Young Researcher Vision Camp, Leibertingen (Germany).

Breher K., Ohlendorf A., & Wahl S. (2019). Inter-session and intra-session repeatability for different modalities of choroidal thickness imaging and segmentation. International Myopia Conference, Tokyo (Japan).

Ohlendorf A., **Breher K.**, Studtrucker K., & Wahl S. (2020). Retinal and foveal shape integrity is preserved in myopia. Investigative Ophthalmology & Visual Science, 61(7), 2687-2687. ARVO, Baltimore (USA).

Breher K., Bumstead J., Straub J., Kubach S., Leahy C., Arianta K., Nafar Z., & Wahl S. (2021). Metrological and refractive aspects of retinal shape estimation from 90° field of view optical coherence tomography. Investigative Ophthalmology & Visual Science, 62(8):1799. ARVO, Virtual meeting.

Neumann A., Breher K., & Wahl S. (2021). Effect of short-wavelength light emitting screen technologies on human contrast sensitivity. Investigative Ophthalmology & Visual Science, 62(8):1375. ARVO, Virtual meeting.

10.3   Non peer reviewed talks

Breher K., (2018). The effect of the optical design of multifocal contact lenses on choroidal thickness. Progress in Ophthalmic Research. Institute for Ophthalmic Research, Eberhard-Karls University Tübingen (Germany).

Breher K., (2019). The role of the choroid in myopia management. Laser World of Photonics, Munich (Germany).

Breher K. (2019). Eye shape and peripheral refraction. Alumni Meeting of the M.Sc. Vision Science & Business (Optometry) program, Benediktbeuern (Germany).

Breher K., (2019). Image-based modeling of foveal pit morphology from distortion-corrected OCT scans. Progress in Ophthalmic Research. Institute for Ophthalmic Research, Eberhard-Karls University Tübingen (Germany).

Breher K. (2019). Wie hängen Netzhautform und Myopie zusammen? Arbeitskreis Ophthalmische Optik, Herrsching (Germany).

Breher K. (2021). Human retinal shape - insights from OCT. Golden Gate Presentations, Online.

Breher K. (2021). The use of OCT in myopia research. Alumni Meeting of the M.Sc. Vision Science & Business (Optometry) program, Benediktbeuern (Germany).

Breher K. (2021). Der Zusammenhang zwischen Netzhautform und peripherer Refraktion. Arbeitskreis Ophthalmische Optik, Aalen (Germany).

11 Statement of own contribution

11.1 Publication 1 - A metrological approach to the analysis of choroidal thickness by optical coherence tomography 3D scans in myopia research

Breher K., Ohlendorf A., & Wahl S. (2019). A metrological approach to the analysis of choroidal thickness by optical coherence tomography 3D scans in myopia research. Scientific Reports, 9(1):20322.

Contribution of the first author:
I helped to develop the initial idea for the experiments and defined the methodology. I performed the measurements on study participants and analyzed the data. I wrote the initial version of the manuscript and improved it based on my ideas and input from the other authors.

Contribution of the other authors:
Dr. Arne Ohlendorf as second author of the paper, conceived the study idea, supported the work with his experience in planning and performing experiments and was involved in the editing of the manuscript. The last author, Prof. Dr. Siegfried Wahl, provided materials, supervised the study and helped to improve the manuscript.

11.2 Publication 2 - Choroidal biomarkers: A repeatability and topographical comparison of choroidal thickness and choroidal vascularity index in healthy eyes

Breher K., Terry L., Bower T., & Wahl S. (2020). Choroidal biomarkers: A repeatability and topographical comparison of choroidal thickness and choroidal vascularity index in healthy eyes. Translational Vision Science & Technology, 9(11), 8-8.

Contribution of the first author:
I helped to develop the initial idea for the experiments and defined the methodology. I performed the measurements on study participants and analyzed the ChT data and performed the statistical analysis of all collected data. I wrote a majority of the initial version of the manuscript and improved it based on my ideas and input from the other authors.

Contribution of the other authors:

The second author of the paper, Dr. Louise Terry helped to develop the initial idea for the experiment and ran the CVI analysis. Dr. Thomas Bower as third author of the paper programmed the software for the CVI analysis. Both authors wrote the methodological CVI part of the manuscript and helped to improve it later on. The fourth author of the paper, Prof. Dr. Siegfried Wahl provided materials, supervised the study and helped to improve the manuscript.

11.3 Publication 3 - Myopia induces meridional growth asymmetry of the retina: a pilot study using wide-field swept-source OCT

Breher K., Ohlendorf A., & Wahl S. (2020). Myopia induces meridional growth asymmetry of the retina: a pilot study using wide-field swept-source OCT. Scientific Reports, 10(1):10886.

Contribution of the first author:

I developed the initial idea for the experiments and defined the methodology. I performed the measurements on study participants and analyzed the data. I wrote the initial version of the manuscript and improved it based on my ideas and input from the other authors.

Contribution of the other authors:

Dr. Arne Ohlendorf as second author of the paper, supported the work with his experience in planning and performing experiments and was involved in the editing of the manuscript. The last author, Prof. Dr. Siegfried Wahl, provided materials, supervised the study and helped to improve the manuscript.

11.4 Publication 4 - Comparison of methods for estimating retinal shape: peripheral refraction vs. optical coherence tomography

Breher K., Calabuig A., Kühlewein L., Ziemssen F., Ohlendorf A., & Wahl S. (2021). Comparison of methods for estimating retinal shape: peripheral refraction vs. optical coherence tomography. Journal of Clinical Medicine, 10(2):174.

Contribution of the first author:

I developed the initial idea for the experiments and defined the methodology. I performed the measurements on study participants and analyzed the data. I wrote the initial version of the manuscript and improved it based on my ideas and input from the other authors.

Contribution of the other authors:

Dr. Alejandro Calabuig and Dr. Arne Ohlendorf supported the work with their experience in data analysis. Dr. Laura Kühlewein and Dr. Focke Ziemssen provided the materials. The last author, Prof. Dr. Siegfried Wahl provided materials and supervised the study. All co-authors helped to improve the manuscript.

12 Acknowledgements

This doctoral thesis was created with the kind support of many individuals.

First of all, I would like to express my sincere gratitude to my advisors Prof. Dr. Siegfried Wahl and Prof. Dr. Frank Schaeffel for their continuous guidance of my doctoral studies and related research, but also for their feedback, motivation and extensive knowledge. Thank you for the opportunities I was given during the last years.

Dr. Arne Ohlendorf for his guidance as mentor, for the constructive meetings and remarks, as well as for sharing his broad experience and always having an open door for questions and discussions. Thank you for this.

I would also like to thank all my former and current colleagues in the Zeiss Vision Science Lab. Thank you for your numerous explanations in your field of expertise and the discussions that opened up new perspectives and solutions. You created a great atmosphere to work in. I further thank all the volunteers for participating in the experiments.

Moreover, I would like to thank the Zeiss Meditec team in Dublin for their support regarding technical, optical and analytical aspects while working with the OCT devices.

Finally and most importantly, I would like to express my deepest gratitude to my family, my partner and my friends for their constant support, love and encouragement throughout the last years.